Transdimensional surface wave inversion

1D, 2D and 3D applications

Rahimi Dalkhani, A.

DOI
10.4233/uuid:a4ff648f-7de1-43b1-a418-844344942c89

Publication date
2024

Document Version
Final published version

Citation (APA)
Rahimi Dalkhani, A. (2024). *Transdimensional surface wave inversion: 1D, 2D and 3D applications*. [Dissertation (TU Delft), Delft University of Technology]. https://doi.org/10.4233/uuid:a4ff648f-7de1-43b1-a418-844344942c89

Transdimensional surface wave inversion

1D, 2D and 3D applications

Dissertation

for the purpose of obtaining the degree of doctor
at Delft University of Technology
by the authority of the Rector Magnificus, prof. dr. ir. T.H.J.J. van der Hagen,
chair of the Board for Doctorates
to be defended publicly on
Thursday 5 September 2024 at 10:00 o'clock

by

Amin RAHIMI DALKHANI

Master of Science in Petroleum Geosciences Engineering, Amirkabir University of Technology, Iran
born in Shiraz, Iran

This dissertation has been approved by the promotor and the copromotor.

Composition of the doctoral committee:

Rector Magnificus,	chairperson
Prof. dr. ir. C.P.A. Wapenaar,	Delft University of Technology, *promotor*
Dr. C. Weemstra,	Delft University of Technology, *copromotor*
Independent members:	
Prof. dr. ir. E.C. Slob,	Delft University of Technology
Prof. dr. P.J. Vardon,	Delft University of Technology
Prof. dr. N. Rawlinson,	University of Cambridge, England
Prof. dr. L.V. Socco,	Politecnico di Torino, Italy
Dr. D.A. Kraaijpoel	TNO

This research has received funding from the Iran Ministry of Science, Research and Technology, and the European Research Council (ERC) under the European Union's Horizon 2020 research and innovation program (grant no. 742703).

ISBN 978-94-6384-623-3

An electronic copy of this dissertation is available at
https://repository.tudelft.nl/.

To my family and friends.

Contents

Summary

Surface wave inversion is a powerful tool for subsurface imaging at various scales, spanning from near-surface characterization to crustal imaging. This study focuses on the transdimensional Markov chain Monte Carlo (McMC) algorithm and its effectiveness for surface wave inversion. We explore its application at different dimensions (1D, 2D, 3D) and scales, encompassing both near-surface and crustal subsurface characterization.

We first demonstrate the fundamentals of surface wave inversion using a least-squares algorithm, a conventional McMC method, and the transdimensional McMC algorithm applied to the (non-linear) 1D inversion problem. We compare these algorithms by applying them to both synthetic and field data. In contrast to the least-squares method, the transdimensional algorithm successfully recovers rapid variations in velocity, particularly at a depth of around 3 km. This observation emphasizes the automatic and localized smoothing applied in the transdimensional McMC algorithm. Furthermore, the transdimensional McMC algorithm yields, inherently, the posterior probability density of the shear wave velocity as a function of depth, offering valuable insights.

In Chapter 3, we extend the study to two dimensions using surface waves retrieved by means of Distributed Acoustic Sensing (DAS), validating the transdimensional algorithm's potential for near-surface applications. We first determine the dispersive behavior of the Rayleigh wave considering lateral variation in the subsurface. This leads to a local dispersion curve at the location of each receiver. To recover a 2D shear wave velocity section of the subsurface, we develop a 2D transdimensional approach to invert all the dispersion curves simultaneously. This approach retains lateral correlations of the recovered shear wave velocities. This two-dimensional application demonstrates the ability of the transdimensional McMC algorithm to reconstruct the two-dimensional shear wave velocity structure of the near-surface.

Finally, we extend the study to three dimensions by recovering the crustal shear wave velocity structure of the Reykjanes Peninsula. As input, we use travel times extracted from Rayleigh waves that were retrieved through the application of seismic interferometry to recordings of ambient seismic noise. We then modify and use the one-step 3D transdimensional surface wave tomography algorithm. This implies that we depart from conventional two-step approaches. Synthetic tests showcase adaptability to ray density, yielding higher resolution in densely sampled areas. Reduced computational costs by modifying the algorithm enhance the applicability for 3D crustal imaging. Our application of the one-step 3D transdimensional algorithm to ambient-noise data provides the first comprehensive shear wave velocity model of the Reykjanes Peninsula. The detailed

shear wave velocity model offers valuable geological and geothermal insights into the subsurface structure, confirming the algorithm's potential as a routine tool for surface wave tomography.

Collectively, these findings advocate the use of one-step transdimensional inversion algorithms for seismic tomography. Their adaptability, efficiency gains, and interpretability contribute to advancing our understanding of subsurface velocity structures. As seismic data volumes grow, embracing innovative inversion approaches becomes imperative, and the transdimensional algorithms showcased in this thesis emerge as a promising tool for pushing the boundaries of seismic tomography.

Samenvatting

Oppervlaktegolfinversie is een krachtig hulpmiddel voor verschillende schalen, variërend van karakterisering van de ondiepe ondergrond tot beeldvorming van de aardkorst. De focus van deze studie is de transdimensionale Markov-keten Monte Carlo (McMC) en de effectiviteit hiervan voor oppervlaktegolfinversie. We onderzoeken de toepassing ervan in verschillende dimensies (1D, 2D, 3D) en schalen, en doen zowel karakterisatie van de ondiepe ondergrond alsmede van de aardkorst.

We demonstreren eerst de basisprincipes van oppervlaktegolfinversie met behulp van een kleinste kwadratenalgoritme, een conventionele McMC-methode, en het transdimensionale McMC-algoritme aan de hand van een één-dimensionaal probleem. We vergelijken deze algoritmen door ze toe te passen op de synthetische en velddata. In tegenstelling tot de kleinste-kwadratenmethode heeft het transdimensionale algoritme met succes scherpe variaties in snelheid kunnen achterhalen, vooral op een diepte van ongeveer 3 km. Deze bevinding onderstreept de automatische en gelokaliseerde afvlakking die wordt toegepast in het transdimensionale McMC-algoritme. Bovendien levert het transdimensionale McMC-algoritme een posterieure waarschijnlijkheidsdichtheid, wat waardevolle inzichten oplevert.

Vervolgens breiden we het onderzoek uit naar 2D-oppervlaktegolfinversie met behulp van Distributed Acoustic Sensing (DAS), waarmee we het potentieel van het transdimensionale algoritme voor toepassingen dicht bij het oppervlak valideren. We bepalen eerst het dispersiegedrag van de Rayleigh-golf, rekening houdend met de laterale variatie in de ondergrond. Dit leidt tot een lokale spreidingscurve op de locatie van elke ontvanger. Om een 2D-schuifgolfsnelheidssectie van de ondergrond te verkrijgen, ontwikkelen we een 2D-transdimensionale benadering om alle dispersiecurven tegelijkertijd te inverteren. Dit behoudt de laterale correlatie van de schuifgolf snelheden. Deze 2D toepassing van het transdimensionale algoritme onderstreept het vermogen van dit algoritme om laterale correlaties zo goed mogelijk te behouden en zodoende de schuifgolfsnelheden in de ondiepe ondergrond te reconstrueren.

Ten slotte breiden we de studie uit met een 3D-studie om de aardkorststructuur van het Reykjanes-schiereiland te achterhalen. We gebruiken hiervoor aankomsttijden van oppervlakte golven die zijn verkregen door middel van crosscorrelaties van seismische ruis. We modificeren hiervoor een éénstaps 3D transdimensionaal oppervlaktegolftomografie algoritme, waarbij we dus afwijken van conventionele tweestapsbenaderingen. Synthetische tests tonen het aanpassingsvermogen aan de straaldichtheid aan, wat een hogere resolutie oplevert in dicht bemonsterde gebieden. Door het algoritme

aan te passen, vergroten we de computationele efficiëntie voor 3D-beeldvorming van de korst. De toepassing van het éénstaps 3D-transdimensionaal algoritme op van ruis afgeleide oppervlakte golven levert het eerste uitgebreide schuifgolf snelheids model van het Reykjanes-schiereiland op. Dit gedetailleerde model biedt waardevolle inzichten in de ondergrondse structuur en bevestigt het potentieel van het algoritme als routinematig hulpmiddel voor oppervlaktegolftomografie.

Gezamenlijk pleiten onze bevindingen voor het routinematig gebruik van transdimensionale inversie-algoritmen in seismische tomografie. Hun aanpassingsvermogen, efficiëntiewinst en interpreteerbaarheid dragen bij aan het bevorderen van ons begrip van ondergrondse structuren. Naarmate de mogelijkheden van seismische inversie groter worden, wordt het omarmen van innovatieve benaderingen absoluut noodzakelijk. De transdimensionale algoritmen die in dit onderzoek worden gepresenteerd, komen naar voren als een veelbelovend hulpmiddel om de grenzen van seismische tomografie te verleggen.

1

Introduction

Seismic tomography, a powerful tool for imaging subsurface structures, has seen remarkable advancements in recent years. With the revolutionary advancements in computational resources, innovative methods employing global search algorithms have captured substantial attention. This thesis explores an innovative Bayesian seismic inversion approach, which exploits a reversible jump Markov chain Monte Carlo algorithm (Green, 1995) to unravel the complexities of subsurface geological structures.

Traditional seismic inversion methods often grapple with user-defined parameters and computational inefficiencies. They often require careful parametrization of the model and proper regularization of the solution to prevent over/under-fitting or to impose some form of structure or constraint on the solution. And those approaches may then still be susceptible to getting stuck in local minima. Global search methods like a standard McMC usually solve the problem of local minima. However, they are computationally inefficient while exploring large model spaces (Sambridge & Mosegaard, 2002; Tarantola, 2005). The partition modeling McMC algorithm presented by Bodin et al. (2009) significantly improved the efficiency and adaptability of the McMC algorithm in a seismic tomography scenario. By self-parametrizing the model space, it eliminates the need for explicit regularization, offering a more dynamic and adaptable approach. Expanding this scheme in a transdimensional framework (Bodin & Sambridge, 2009; Bodin et al., 2012) introduces novel elements such as an unknown number of partitioning cells and dynamically estimated data uncertainty. This not only enhances computational efficiency but also yields a more accurate representation of the subsurface.

In this thesis, we explore the transdimensional method using different applications of seismic inversion. The structure of the thesis is organized as follows:

Chapter 2 provides an in-depth exploration of the partition modeling algorithm and its transdimensional extension compared with a regularized least-squares approach. We investigate these approaches using a 1D surface wave dispersion curve inversion problem. It lays the foundation for understanding the self-parametrizing

and adaptive nature of the transdimensional algorithm, emphasizing its significance in seismic tomography.

Chapter 3 delves into the application of the transdimensional algorithm in the case of a 2D data setup. We employ distributed acoustic sensing (DAS) for surface wave analysis, specifically focusing on active-source surveys. Multi-offset phase analysis (MOPA) is introduced as a tool for extracting laterally varying dispersion curves. The transdimensional inversion algorithm is then employed to produce a 2D shear wave velocity image, with validation against borehole data. In this chapter, we discuss the transdimensional approach in more detail and propose a few modifications to enhance the algorithm's efficiency.

Chapter 4 shifts the focus to a real-world geothermal setting, specifically the Reykjanes Peninsula in southwest Iceland. It explores the feasibility of a recently developed transdimensional algorithm for performing 3D surface wave inversion in one step (Zhang et al., 2018, 2020). We study the potential of the algorithm to interferometric surface waves retrieved from ambient noise recorded on and around the Reykjanes Peninsula. To that end, we perform several synthetic tests with the station configuration of the Reykjanes seismic network. We also propose some modifications to the original algorithm to increase the algorithm's efficiency.

Chapter 5 extends the application of the aforementioned 3D transdimensional inversion method to address the challenges and opportunities in imaging the subsurface of the Reykjanes Peninsula. It emphasizes the significance of probabilistic tomography and explores the potential of shear wave velocity models derived from ambient noise seismic data. We first retrieve surface wave dispersion curves from the recorded noise by the Reykjanes seismic network. Subsequently, we employ the modified one-step transdimensional approach to reconstruct a 3D shear wave velocity model of the study area. Finally, we provide a comprehensive interpretation of the recovered velocity model, concluding with a comparative analysis against images obtained by means of other geophysical methods employed in the study area.

Chapter 6 presents the main conclusions drawn from this thesis.

2

1D surface wave dispersion curve inversion

Abstract: Transdimensional inversion, a Bayesian algorithm employing reversible jump Markov chain Monte Carlo (McMC), estimates posterior distributions. In this chapter, we explore the transdimensional algorithm's efficacy in a 1D surface wave dispersion curve inversion, including a comparison with a nonlinear least-squares algorithm and a conventional McMC method with fixed parametrization. The nonlinear least-squares method has its limitations in scenarios with numerous parameters and potential local minima. Conventional McMC with fixed parametrization is identified as inefficient, especially in exploring large model spaces. Partition modeling McMC offers self-parametrization but faces challenges in choosing the optimal number of cells. Transdimensional McMC, introducing adaptability by treating the number of cells as an unknown, yields promising results. A field data application from the Reykjanes Peninsula highlights its superiority in recovering reliable and interpretable subsurface velocity profiles. The interpretability is attributed to the uncertainty that the algorithm inherently provides.

2.1 Introduction

In tomographic imaging, a set of surface measurements is used to infer some internal physical properties (e.g. velocity, density, composition, temperature). The conventional algorithms (either least-squares or McMC with fixed parametrization) for seismic inversion require proper parametrization, regularization, and a good estimate of data uncertainty (Tarantola, 2005; Aster et al., 2018), which must be defined a priori by the user. Moreover, in a conventional McMC algorithm with fixed parametrization, if too many parameters (are needed to) define a model, the number

ChatGPT is employed to enhance the quality of specific sentences and paragraphs while drafting the initial version of this chapter, acknowledging its valuable assistance in refining the content: OpenAI. (2023). ChatGPT [Large language model]. https://chat.openai.com

of samples needed to explore the whole model space may become prohibitively large (Tarantola, 2005).

The partition modeling applied to McMC, which is introduced to seismic tomography by Bodin et al. (2009), is a self-parametrizing algorithm with naturally smooth results that do not need any regularization. The model space is partitioned by a given number of non-overlapping regions. In this method, the position of each cell defining the geometry of the velocity field and the velocity field itself are unknown in the inversion process. The inversion is carried out with a fully nonlinear parameter search method formulated in a Bayesian framework. However, the number of cells is yet a parameter to be chosen properly. In the transdimensional scheme (Bodin & Sambridge, 2009), in addition to the velocity field and cell positions, the number of partitioning cells is itself one of the unknowns to be determined. The data uncertainty can also be treated as an unknown and can be estimated and inferred during the inversion process (Bodin et al., 2012).

2.2 The inverse problem

In a seismic inverse problem, the aim is to recover the seismic velocity structure of the Earth's subsurface using the observed data. Based on the physical theory of wave propagation, we can relate an observed seismic dataset, $\mathbf{d}_{obs}$, to a subsurface model $\mathbf{m}$ using the expression:

$$\mathbf{d}_{obs} = g(\mathbf{m}), \tag{2.1}$$

where g is a forward function that relates $\mathbf{m}$ to $\mathbf{d}_{obs}$. It should be noted that often even g is an approximation itself (the forward function does not necessarily capture all the physics). In a surface wave inversion problem, the seismic dataset ($\mathbf{d}_{obs}$) consists of the retrieved surface wave dispersion curves (DCs[1]). The forward function g here is a function that computes the theoretical dispersion curves for a subsurface model $\mathbf{m}$. In this chapter, we use the MATLAB package developed by Wu et al. (2019) using the method proposed in Buchen & Ben-Hador (1996) to compute the theoretical dispersion curve (i.e., phase velocity versus frequency) in a 1D earth model. Figure 2.1 shows a 1D shear wave velocity model ($\mathbf{m}$) and its corresponding theoretical DC. It must be noted that the Rayleigh wave phase velocity is a function of the thickness, the shear wave velocity (v_s), the compressional wave velocity (v_p), and the density (ρ) of each layer. Furthermore, in this chapter the compressional wave velocity is assumed to be a linear function of v_s according to $v_p = 1.78 v_s$ (Allen et al., 2002) and that the mass density ρ is assumed to be related to the latter according to $\rho = 2.35 + 0.036(v_p - 3)^2$, where v_p and v_s are in km/s and ρ in g/cm^3 (Kurita, 1973; Zhang et al., 2020).

Solving the inverse problem entails searching for a certain velocity model $\mathbf{m}$ such that the predicted data $g(\mathbf{m})$ fits the observed DC ($\mathbf{d}_{obs}$) as closely as possible. The agreement between observed and predicted data may be quantified by a misfit function such as a weighted least-squares misfit:

[1] For a detailed explanation of retrieving surface wave DCs, see section 3.2.2 for active seismic data and appendix A.2 for passive seismic data.

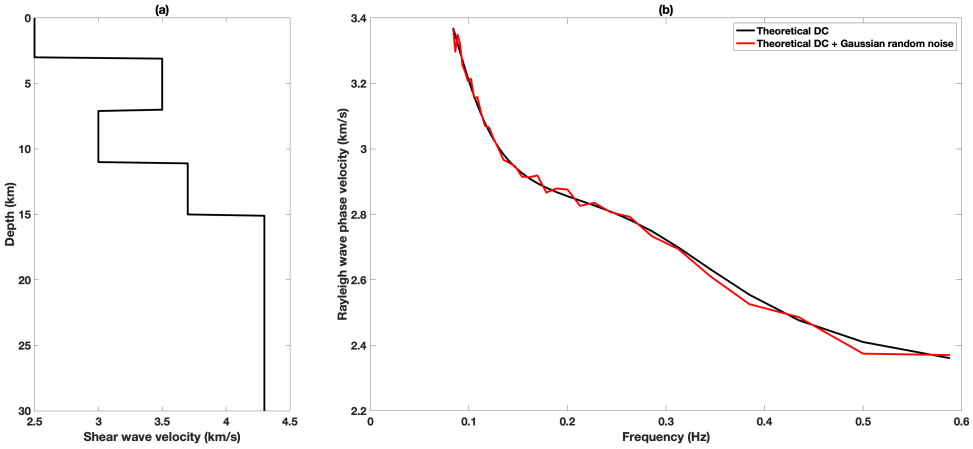

Figure 2.1. *(a) A 1D synthetic velocity model. (b) The theoretical fundamental mode dispersion curve (black). Higher modes are ignored in this experiment. The red curve is the theoretical fundamental mode dispersion curve with additive Gaussian noise with a standard deviation of 20 m/s to be used in the inversion algorithms.*

$$\phi(\mathbf{m}) = \left\| \frac{g(\mathbf{m}) - \mathbf{d}_{obs}}{\sigma_{\mathbf{d}}} \right\|^2 = \left(g(\mathbf{m}) - \mathbf{d}_{obs}\right)^{\mathsf{T}} \mathbf{C}_d^{-1} \left(g(\mathbf{m}) - \mathbf{d}_{obs}\right), \tag{2.2}$$

where $\sigma_{\mathbf{d}}$ is the uncertainty vector or noise associated with the observed data, $^{\mathsf{T}}$ denotes transposition, and $\mathbf{C}_d$ is the covariance matrix of data noise, representing the uncertainty in the data and the correlation between data errors. In an inverse problem, uncertainty controls the level of fit. It determines the extent to which the modeled or predicted data should be close to the observed data. High uncertainty means that the noise level in the data is high and the inversion algorithm is not required to be sensitive to high-frequency changes in the data and velocity model. Hence, an increase in data uncertainty will lead to smoother models.

2.3 Nonlinear least-squares inversion

A least-squares inversion algorithm minimizes the misfit function (Equation 2.2). The minimum of the objective function $\phi(\mathbf{m})$ may be found by equating the first derivative of the objective function to zero $\left(\frac{\partial \phi(\mathbf{m})}{\partial \mathbf{m}} = 0\right)$. This results in:

$$\frac{\partial \phi(\mathbf{m})}{\partial \mathbf{m}} = 2\mathbf{J}^{\mathsf{T}} \mathbf{C}_d^{-1} \left(g(\mathbf{m}) - \mathbf{d}_{obs}\right) = 0, \tag{2.3}$$

where $\mathbf{J} = \frac{\partial g(\mathbf{m})}{\partial \mathbf{m}}$ is the Jacobian matrix. Since $g(\mathbf{m})$ is a nonlinear function, Equation 2.3 becomes a non-linear equation to be solved. To solve this equation, let us assume that the nonlinear function $g(\mathbf{m})$ can be linearized around the initial guess

$\mathbf{m}_i$ as (Tarantola, 2005, p. 68):

$$g(\mathbf{m}) \approx g(\mathbf{m}_i) + \mathbf{J}(\mathbf{m} - \mathbf{m}_i). \tag{2.4}$$

Substituting relation 2.4 in Equation 2.3 and solving for $\mathbf{m}$ yields:

$$\mathbf{m} = \mathbf{m}_i - \left(\mathbf{J}^\intercal \mathbf{C}_d^{-1} \mathbf{J}\right)^{-1} \mathbf{J}^\intercal \mathbf{C}_d^{-1} \left(g(\mathbf{m}_i) - \mathbf{d}_{obs}\right). \tag{2.5}$$

By iteratively solving this equation and setting $\mathbf{m}_i = \mathbf{m}$ at each iteration, one can find the optimal solution when the model norm $||\mathbf{m} - \mathbf{m}_i||$ becomes sufficiently small. This algorithm is called Gauss–Newton (GN) method (see Aster et al., 2018, chapter 9, p. 240). However, Equation 2.5 often becomes unstable due to the solution's nonuniqueness. Therefore, it is necessary to use proper regularization to choose a solution out of all possible solutions (Bodin & Sambridge, 2009). The objective function used in the inversion scheme is then a linear combination of the misfit function, the distance to a reference model, or the norm of the first or second spatial derivative of the model (Bodin & Sambridge, 2009). This objective function reads:

$$\phi(\mathbf{m}) = \left(g(\mathbf{m}) - \mathbf{d}_{obs}\right)^\intercal \mathbf{C}_d^{-1} \left(g(\mathbf{m}) - \mathbf{d}_{obs}\right) + \lambda(\mathbf{m} - \mathbf{m}_i)^\intercal (\mathbf{m} - \mathbf{m}_i) + \eta(\mathbf{D}\mathbf{m})^\intercal (\mathbf{D}\mathbf{m}), \tag{2.6}$$

where $\mathbf{D}$ is a finite difference spatial derivative operator, and λ is usually referred to as the damping parameter that prevents the solution from staying too far from the reference model $\mathbf{m}_i$, which ensures the stability of the inversion at each iteration (Xia et al., 1999; Bodin & Sambridge, 2009). It is important to note that the incorporation of this damping term does not imply that the ultimate solution must closely resemble the initial guess, since the reference model $\mathbf{m}_i$ undergoes updates at each iteration. Finally, η is called the smoothing parameter, which ensures the smoothness of the solution model (Bodin & Sambridge, 2009).

The optimal model can be obtained by setting the first derivative of the regularized objective function (Equation 2.6) to zero, expressed as:

$$\frac{\partial \phi(\mathbf{m})}{\partial \mathbf{m}} = 2\mathbf{J}^\intercal \mathbf{C}_d^{-1} \left(g(\mathbf{m}) - \mathbf{d}_{obs}\right) + 2\lambda(\mathbf{m} - \mathbf{m}_i) + 2\eta \mathbf{D}^\intercal \mathbf{D}\mathbf{m} = 0. \tag{2.7}$$

Similar to Equations 2.5 one can first substitute relation 2.4 into Equation 2.7 and derive the iterative formula for the regularized GN algorithm as:

$$\mathbf{m} = \mathbf{m}_i - \left(\mathbf{J}^\intercal \mathbf{C}_d^{-1} \mathbf{J} + \lambda \mathbf{I} + \eta \mathbf{D}^\intercal \mathbf{D}\right)^{-1} \left(\mathbf{J}^\intercal \mathbf{C}_d^{-1} \left(g(\mathbf{m}_i) - \mathbf{d}_{obs}\right) + \eta \mathbf{D}^\intercal \mathbf{D}\mathbf{m}_i\right). \tag{2.8}$$

Assuming $\eta = 0$, Equation 2.8 underlies the well-known Levenberg–Marquardt method (Levenberg, 1944; Marquardt, 1963). The stability of this Equation relies on tuning the damping parameter λ. In practice, determining a suitable damping factor involves testing multiple values of λ. Small values of λ (i.e., close to zero) may result in an unstable inversion (i.e., the algorithm diverges). Conversely, higher values of λ force the inversion to set $\mathbf{m}$ too close to the reference model $\mathbf{m}_i$, causing a slower convergence of the algorithm. Consequently, the lowest λ that ensures stability in solving Equation 2.8 is desirable. After finding a proper damping parameter λ, one can find the optimum smoothing parameter η using different methods such as

L-curve, cross-validation, or the application of the discrepancy principle (see Aster et al., 2018, chapter 10).

We apply this method to invert the synthetic dispersion curves illustrated in Figure 2.1b. We presente the results in Figures 2.2-2.3 for both noise-free and noisy dispersion curves, respectively. We first defined the initial model ($\mathbf{m}_i$) with 51 points and assigned to each point a velocity of 4.3 km/s, which is the true velocity of the lower half-space in the synthetic model. This selection is motivated by the half-space being least sensitive to shear wave velocity perturbations in the lower half-space, making it particularly influenced by the initial model during the inversion. Subsequently, assuming $\eta = 0$, we identified the minimum damping factor λ for which Equation 2.8 remained stable and converged to a velocity model. In both cases, this optimal λ value was found to be $\lambda = 5$.

The optimal smoothing parameter η was then determined using an L-curve analysis, as depicted in Figure 2.2a and Figure 2.3a. Notably, the optimal η in Figure 2.3a was higher than that in the noise-free experiment, reflecting the impact of additive noise. In the noise-free scenario, the final estimated model demonstrated a smoothly regularized approximation of the true model. In contrast, in the experiment with additive noise, the final velocity model deviated from the true velocity model.

Finding the optimum regularization parameter is a challenge. The number of grid points for the model parametrization should also be defined by the user, which affects the resolution of the final inverted model (Bodin & Sambridge, 2009). Moreover, the smoothing technique utilizes a uniform smoothing parameter for the entire model, overlooking potential variations in smoothing needs at the local level. Additionally, any approaches like the GN method explained here may suffer from local minima (Aster et al., 2018). They are sensitive to the initial guess and can get trapped in local minima, thus missing the global minimum. These methods are commonly employed in seismic inversion when the objective function is relatively smooth and the solution space can be well approximated by local information (Aster et al., 2018). Global optimization techniques like Monte Carlo methods can be used for seismic inversion to explore the wide range of possible subsurface models. They are particularly useful when dealing with complex, multimodal objective functions (Sambridge & Mosegaard, 2002). However, such methods can be computationally very expensive and may not converge to a solution as quickly as the local search methods. In the following sections, we explain three different algorithms of the Markov chain Monte Carlo approaches, which are in a Bayesian framework.

2.4 Bayesian inference

2.4.1 Bayesian framework

A Bayesian inversion approach aims to recover the probability density of the model parameters given the observed data, $p(\mathbf{m}|\mathbf{d}_{obs})$. The posterior probability density function is derived by applying Bayes' rule (Bayes, 1958), which combines prior information on the model parameters with observed data as:

$$p(\mathbf{m}|\mathbf{d}_{obs}) = \frac{p(\mathbf{d}_{obs}|\mathbf{m})\,p(\mathbf{m})}{p(\mathbf{d}_{obs})}, \tag{2.9}$$

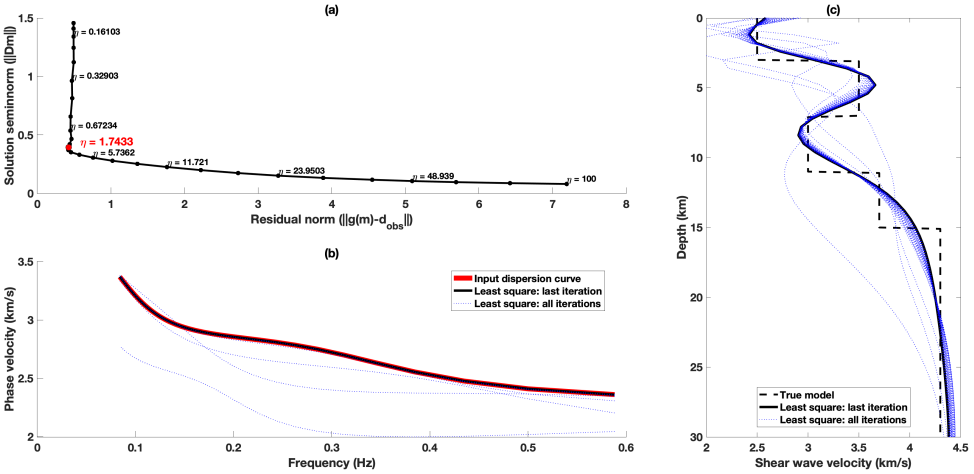

Figure 2.2. *The regularized GN method for the inversion of the noise-free synthetic dispersion curve. (a) The L-curve to find the optimum smoothing parameter η. (b) The input DC (red) and the modeled DCs (dotted blue) at different iterations of the inversion algorithm. (c) The true shear wave velocity model (dashed black) and the inverted shear wave velocity model (dotted blue) at different iterations of the inversion and the final inverted model (black solid).*

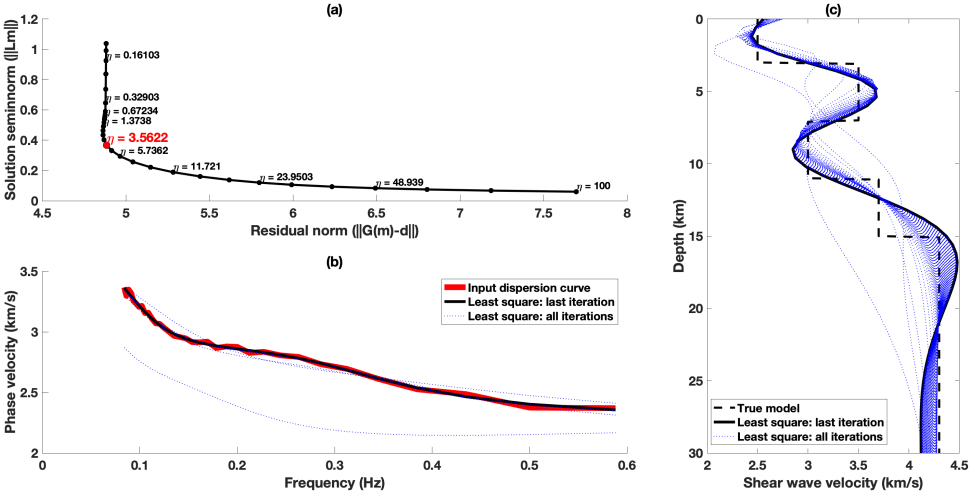

Figure 2.3. *As Figure 2.2, but for a noisy synthetic dispersion curve.*

where $\mathbf{d}_{obs}$ is a vector defined by the set of observed data and $\mathbf{m}$ is the vector of the model parameters. $p(\mathbf{d}_{obs}|\mathbf{m})$ is the likelihood, $p(\mathbf{m})$ is the prior probability density and $p(\mathbf{d}_{obs})$ is often referred to as the evidence. The evidence, $p(\mathbf{d}_{obs})$, can be considered as constant because it is not a function of any particular model $\mathbf{m}$ (e.g.,

Sambridge et al., 2006). Hence:

$$p(\mathbf{m}|\mathbf{d}_{obs}) \propto p(\mathbf{d}_{obs}|\mathbf{m})p(\mathbf{m}). \tag{2.10}$$

The likelihood function $p(\mathbf{d}_{obs}|\mathbf{m})$ quantifies the misfit between observed and predicted data. For a simple least-squares misfit (Equation 2.2), the likelihood function is Gaussian:

$$p(\mathbf{d}_{obs}|\mathbf{m}) \propto \exp\left(-\frac{\phi(\mathbf{m})}{2}\right). \tag{2.11}$$

Given that all inferences drawn from the posterior are inherently tied to the prior distribution, the significance of priors in Bayesian inversion schemes cannot be overstated. The selection of an inappropriate prior adversely affects the result. To avoid the potential introduction of biases stemming from the prior, we opted for uniform prior distributions with wide ranges for all model parameters. The model is initially parameterized with n non-overlapping one-dimensional Voronoi cells, each defined by a cell nucleus (c_i) and an assigned velocity (v_i). Since the model parameters (i.e., number of cells, location of nuclei of each cell, and the velocity assigned to each cell) are independent, the prior can be written as:

$$p(\mathbf{m}) = p(n)p(\mathbf{c}|n)p(\mathbf{v}|n), \tag{2.12}$$

where n is the number of model parameters or cells, $p(n)$ is the prior on the number of cells, $p(\mathbf{c}|n)$ is the prior on cell nuclei location given the number of cells, and $p(\mathbf{v}|n)$ is the prior on cell velocity given the number of cells (see Bodin & Sambridge, 2009; Bodin et al., 2012, for more details).

2.4.2 Markov chain Monte Carlo method

The Markov chain Monte Carlo (McMC) method is an iterative stochastic technique designed to generate samples from the posterior probability density. The initial model is chosen randomly, and the determination of the subsequent model in the 'chain' relies on a proposal probability distribution (q), solely contingent on the present state of the model. In essence, the proposal involves selecting the new model, $\mathbf{m}'$, as a random deviate from the conditional probability distribution $q(\mathbf{m}'|\mathbf{m})$, with dependence solely on the current model $\mathbf{m}$. The acceptance or rejection of the proposed samples is determined by:

$$\begin{aligned}\alpha(\mathbf{m}'|\mathbf{m}) &= \min\left[1, \text{prior-ratio} \times \text{likelihood-ratio} \times \text{proposal-ratio} \times |\mathbf{J}|\right], \\ &= \min\left[1, \frac{p(\mathbf{m}')}{p(\mathbf{m})}\frac{p(\mathbf{d}_{obs}|\mathbf{m}')}{p(\mathbf{d}_{obs}|\mathbf{m})}\frac{q(\mathbf{m}'|\mathbf{m})}{q(\mathbf{m}|\mathbf{m}')} \times |\mathbf{J}|\right],\end{aligned} \tag{2.13}$$

where the matrix $\mathbf{J}$ is the Jacobian of the transformation from $\mathbf{m}$ to $\mathbf{m}'$ and is crucial for accounting for the scale changes inherent in transformations involving jumps between dimensions (Green, 1995). The proposal probability distribution, denoted as q, serves as the basis for suggesting a new model and can take the form of any desired function, such as a Gaussian distribution. After drawing a model ($\mathbf{m}'$) from the proposal distribution $q(\mathbf{m}'|\mathbf{m})$, it undergoes a selection process based on

2

the acceptance probability $\alpha(\mathbf{m}'|\mathbf{m})$. This involves generating a uniform random number, r, between 0 and 1. If $r \leq \alpha$, the proposed model is accepted, replacing the current model $\mathbf{m}$ with the proposed model $\mathbf{m}'$, and the chain advances to the next step. However, if $r > \alpha$, the proposed model is rejected, and the current model ($\mathbf{m}$) is preserved for the subsequent chain step, repeating the process. The acceptance probability, $\alpha(\mathbf{m}'|\mathbf{m})$, plays a critical role in ensuring that the samples conform to the target density $p(\mathbf{m}|\mathbf{d}_{obs})$ (Bodin & Sambridge, 2009).

2.4.3 Conventional McMC with fixed parametrization

The conventional McMC algorithm for inverse problems considers the velocity field as the only unknown parameter (Menke, 2018). To use McMC sampling, we need to compute the acceptance ratio of Equation 2.13. In this case number of cells, position of cells, and uncertainty parameters ($\sigma_{\mathbf{d}}$) are fixed. Hence, the prior (Equation 2.12) becomes:

$$p(\mathbf{m}) = p(\mathbf{v}|n). \tag{2.14}$$

By assuming a minimal prior knowledge of velocity, using a uniform prior distribution, and assuming that the velocity is independent in each cell, the prior can be calculated by (Bodin et al., 2009):

$$p(\mathbf{m}) = \left(\frac{1}{\Delta v}\right)^n, \tag{2.15}$$

where n represents the number of cells, Δv is the difference between the maximum (v_{max}) and minimum (v_{min}) priors on shear wave velocity. Because of a fixed number of cells, n, the prior probability remains constant in each iteration. Hence the prior ratio in Equation 2.13 will be constant and equal to 1. The likelihood ratio in Equation 2.13 can be computed by using Equation 2.11 for each iteration of the chain. By considering the proposal distribution to be Gaussian, it will be symmetric (i.e. $q(\mathbf{m}'|\mathbf{m}) = q(\mathbf{m}|\mathbf{m}')$). The proposal ratio will therefore be constant and equal to 1. Finally, due to the fixed number of cells, there is no change in model parameter dimensions, so $|\mathbf{J}| = 1$. The acceptance ratio, therefore, becomes:

$$\begin{aligned}
\alpha(\mathbf{m}'|\mathbf{m}) &= min\left[1, \frac{p(\mathbf{d}_{obs}|\mathbf{m}')}{p(\mathbf{d}_{obs}|\mathbf{m})}\right] \\
&= min\left[1, \frac{\exp(-\frac{\phi(\mathbf{m}')}{2})}{\exp(-\frac{\phi(\mathbf{m})}{2})}\right] \\
&= min\left[1, \exp(\frac{\phi(\mathbf{m}) - \phi(\mathbf{m}')}{2})\right].
\end{aligned} \tag{2.16}$$

The flowchart for this McMC algorithm is depicted in Figure 2.4. The chain starts with an initial (random) velocity model, in which the number of cells and their positions are fixed. The next step is to perturb the velocity model by randomly selecting a cell and proposing a new velocity for that cell using a Gaussian probability distribution centered at the current velocity model. The proposed model

(sample) is then accepted or rejected based on the acceptance probability ratio of Equation 2.16. When sufficient samples are drawn from the posterior distribution, it becomes feasible to calculate key statistical measures such as the mean and standard deviation. It is common practice to discard samples from the initial phase of the chain, known as the burn-in period. This phase allows the algorithm to mitigate the influence of the initial model and attain a satisfactory mixing of posterior samples (Bodin & Sambridge, 2009).

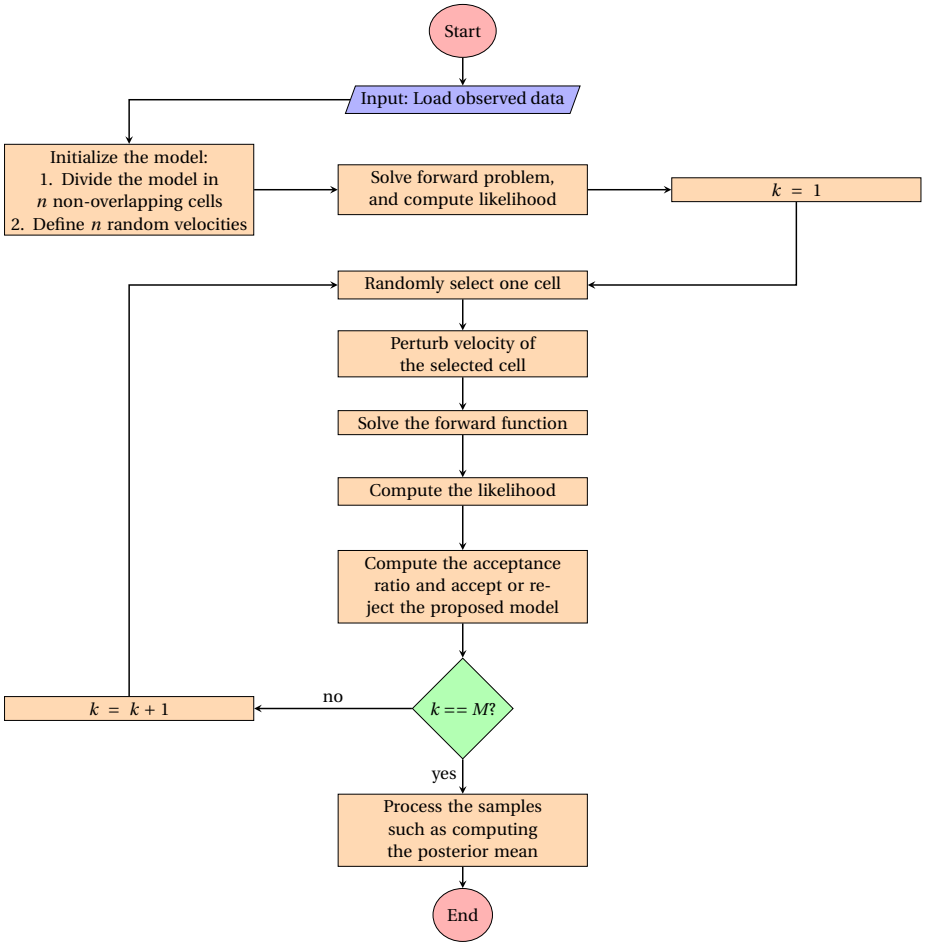

Figure 2.4. *Flowchart to draw M samples using a conventional McMC algorithm, wherein the number of cells and the position of cells are known and fixed.*

Figure 2.5 shows the results of the conventional McMC inversion for the noisy synthetic data of Figure 2.1, assuming that number of cells (or layers) and position of cells (or thickness of layers) are known. We examined a scenario involving five

cells (layers) with known positions, mirroring the true configuration. The velocity of each cell (layer) is unknown and is to be estimated using the Markov chain Monte Carlo (McMC) algorithm. To adequately sample the posterior distribution, we employed 20 independent McMC chains, each generating 5000 samples, in which the first 2000 samples were discarded as the burn-in steps. Figure 2.5a illustrates the samples generated by a specific chain, offering insight into the velocity variations during the McMC sampling process. In Figure 2.5b, the true model, post-burn-in posterior mean, least-squares estimation, and the posterior probability density of the velocity model are presented. Notably, the posterior mean aligns reasonably well with the true model. The posterior probability density, representing the histogram of post-burn-in samples, accurately captures the true model structure and highlights the sensitivity of observed data to shear wave velocity. The width of the posterior probability density increases with depth.

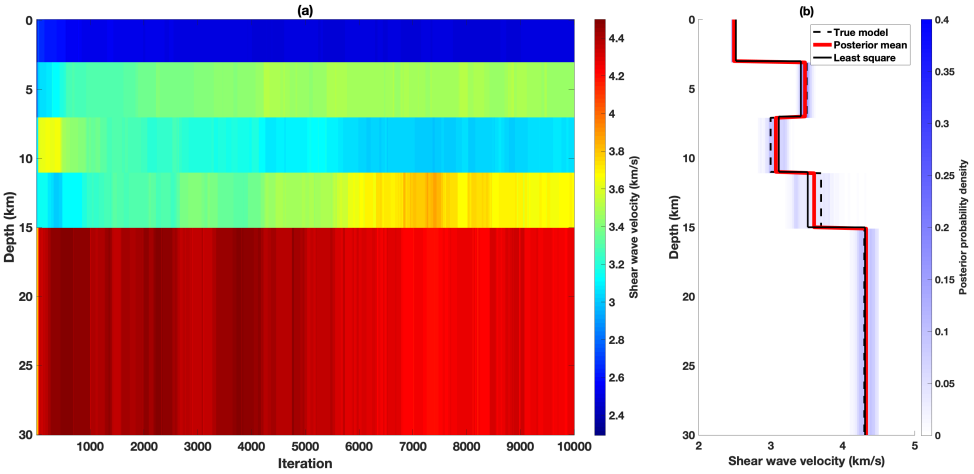

Figure 2.5. *The results of McMC sampling assuming five cells (layers) with known true cell positions. (a) Sampled models of a particular chain. (b) True model (dashed black line), posterior mean (red), least-squares solution (black) as in Figure 2.3c, and the posterior probability density (white-blue colored histogram). The least-squares solution is obtained under the assumption that the number of layers and layer interfaces are known.*

The scenario discussed above, with the number of cells and position of cells as in the true model, represents a simplified case. In reality, both the number of cells (or layers) and their positions are typically unknown. In practice, a refined grid of cells is employed, featuring equispaced distances like the one used in the least-squares algorithm in Figures 2.2-2.3. We exemplified such a case in Figure 2.6 using 30 cells with equispaced cell positions. Not surprisingly, we needed to generate more samples to represent the posterior due to the increased number of unknown model parameters. As you can see, the recovered posterior density resembles the true model fairly well despite the limited resolution. For a higher resolution, it is

necessary to consider more cells. However, the resolution is also limited by the sensitivity of the input data to the velocity model. Therefore, it is difficult for a user to choose a proper number of cells. Additionally, an increasing number of cells requires more samples to be collected and hence demands a high computational cost even for this simple 1D problem. In the next section, we explain a more efficient McMC algorithm in which the number of cells is fixed but the position of cells and the velocity assigned to each cell are variable. This algorithm is called partition modeling McMC (see Bodin et al., 2009).

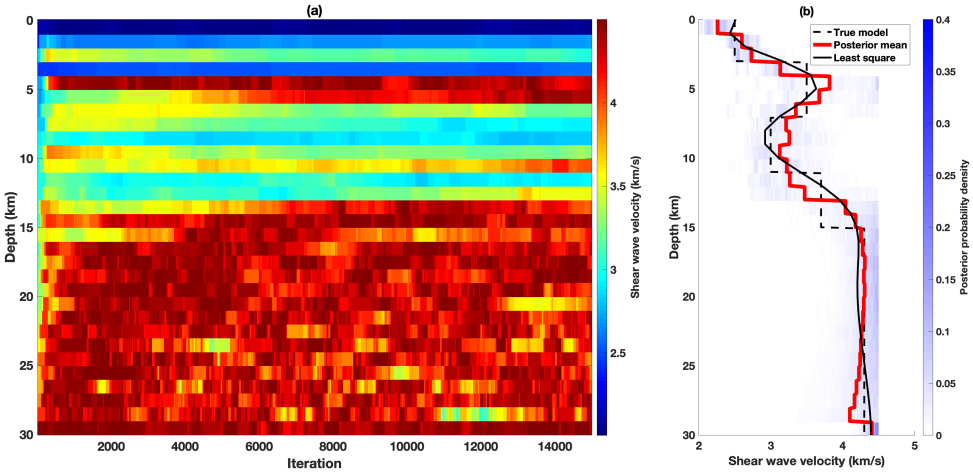

Figure 2.6. *As Figure 2.5, but with 30 refined cells (layers) with known equispaced cell positions. The least-squares solution is also obtained under the assumption of 30 layers with equal thicknesses.*

2.4.4 Partition modeling McMC

Partition modeling is a method of statistical analysis that is used for non-linear regression and classification, and it is particularly useful for dealing with parameters that vary spatially. Bodin et al. (2009) extended the partition modeling method to the seismic tomography problem. The procedure involves a dynamic parametrization for the model which can adapt to an uneven spatial distribution of the information on the model parameters contained in the observed data. In this method, instead of a dense regular grid of cells, as in Figure 2.6, a small number of irregular cells is considered. The velocity and position of cells are considered as unknowns. However, the number of cells is fixed. Hence, the prior (Equation 2.12) becomes:

$$p(\mathbf{m}) = p(\mathbf{c}|n)\,p(\mathbf{v}|n). \tag{2.17}$$

Because of the fixed number of cells, n, this prior probability remains constant during the McMC sampling. The acceptance ratio, therefore, is similar to the

conventional McMC and can be simply computed by Equation 2.16 (see Bodin et al., 2009, for details).

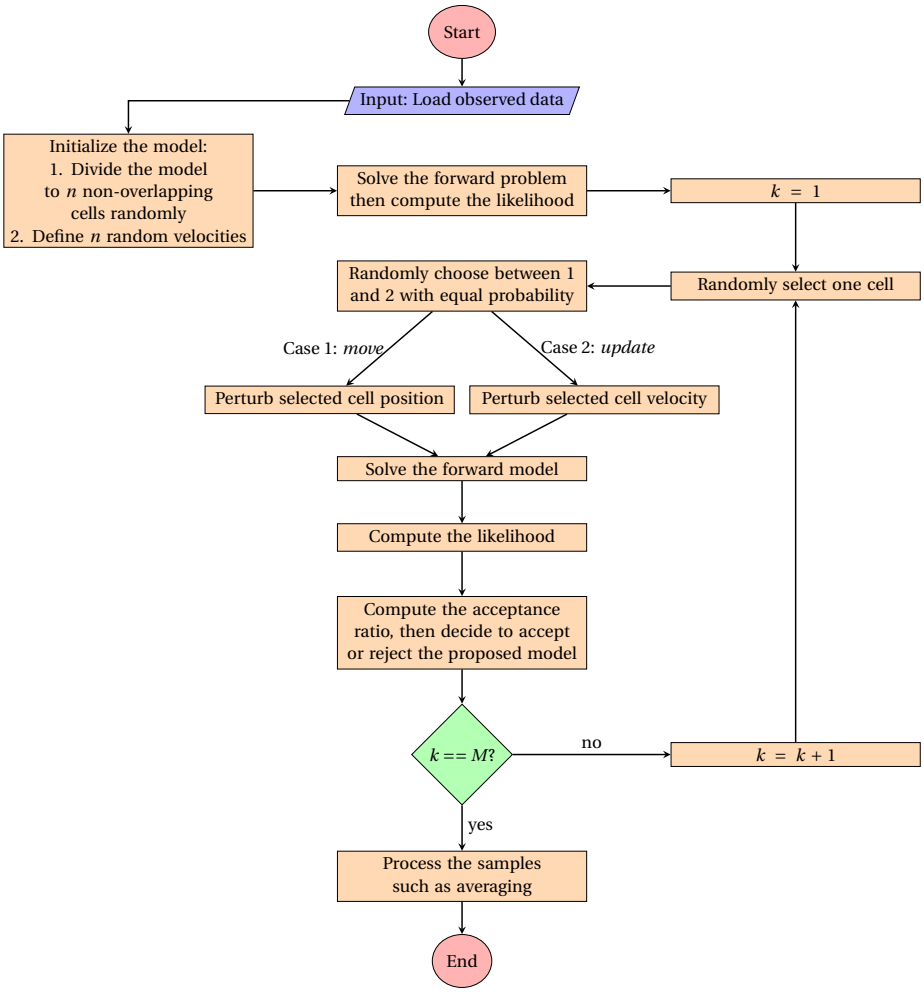

Figure 2.7. *Flowchart to draw M samples using the partition modeling McMC algorithm, wherein the number of cells is known and fixed. However, the position of cells and the velocity assigned to each cell are unknown and variable.*

The flowchart for this partition modeling McMC algorithm is depicted in Figure 2.7. A chain starts with an initial (random) model, in which the number of cells is known but the position of each cell and the velocity assigned to each cell is generated randomly. The next step is to perturb the model by randomly selecting a cell and proposing a new velocity (*update* step) or a new position (*move* step) with equal probability. The proposed model (sample) is then accepted or rejected based

on the acceptance probability ratio of Equation 2.16.

To assess the performance of the partition modeling Markov chain Monte Carlo (McMC) approach, we explored model parametrization using five and ten irregular partitioning cells. The outcomes of inverting the noisy dispersion curve from Figure 2.1b are presented in Figures 2.8 and 2.9. For an effective sampling of the posterior distribution, we employed 20 independent McMC chains, each generating 10,000 samples, with the initial 4,000 samples discarded as burn-in steps in both cases.

The results reveal that the partition modeling McMC inversion produces a naturally smooth outcome, exhibiting good agreement with the true velocity model. Notably, at the model's top, where the input data is more velocity-sensitive, the recovered model approximates the layer discontinuities. However, as depth increases and sensitivity diminishes (leading to increased uncertainty), the recovered pointwise averaged model exhibits enhanced smoothing. This indicates that the algorithm adapts to the input data resolution, employing local smoothing—a notable contrast to regularized least-squares algorithms (section 2.3), which uniformly smooths the entire resulting model.

Consequently, the partition modeling McMC approach yields a solution that is stable, self-regularized, and self-smoothed. However, users must exercise careful consideration when selecting the number of cells. A comparison between Figures 2.8 and 2.9 underscores that the selection of the number of cells influences the recovered posterior probability, even in this seemingly straightforward 1D inversion problem. Given that the true velocity model comprises 5 layers, our anticipation was to better recover the model using 5 variable cells. Surprisingly, the models sampled with 10 variable cells appear to provide a better representation of the posterior compared to the models sampled with 5 variable cells. In more complex scenarios, with a broader model space to explore, determining the optimal number of cells becomes a challenging aspect of the approach.

2.4.5 Transdimensional McMC

The number of cells/unknowns in the partition modeling McMC framework is a user-dependent parameter. Alternatively, the application of a reversible jump algorithm introduces variability to this parameter. The reversible jump algorithm, as introduced by Green (1995), is a statistical approach for Bayesian inference that accommodates a variable number of unknowns. This method was employed by Bodin & Sambridge (2009) in addressing seismic tomography challenges. Within this algorithm, all aspects of model parametrization, including the number of cells, cell position, and geometry, are integrated into the inversion process. This is achieved through the use of a variable number of mobile Voronoi cells exhibiting varying geometry and numbers. The size, position, shape, and number of the cells defining the velocity model, as well as the velocity assigned to each cell are directly determined by the available input data. Consequently, the prior distribution (as expressed in Equation 2.12) can be formulated as:

$$p(\mathbf{m}) = p(n)\,p(\mathbf{c}|n)\,p(\mathbf{v}|n). \tag{2.18}$$

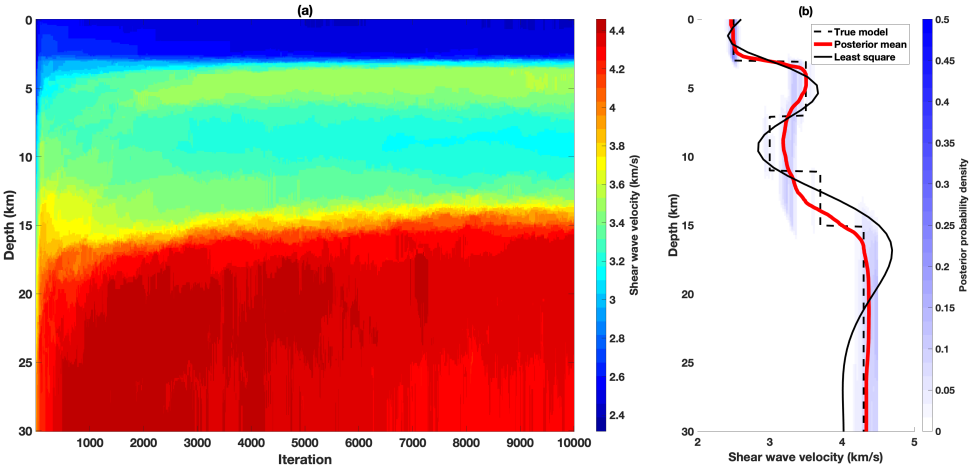

Figure 2.8. *Results of the partition modeling McMC using 5 cells with variable positions and velocities. (a) The average of the accumulated samples is computed at each iteration, wherein the sampled models from 20 chains are superimposed and averaged to collectively represent all samples. (b) True model (dashed black line), posterior mean (red), least-squares solution (black) as in Figure 2.3c, and the posterior probability density (white-blue colored histogram).*

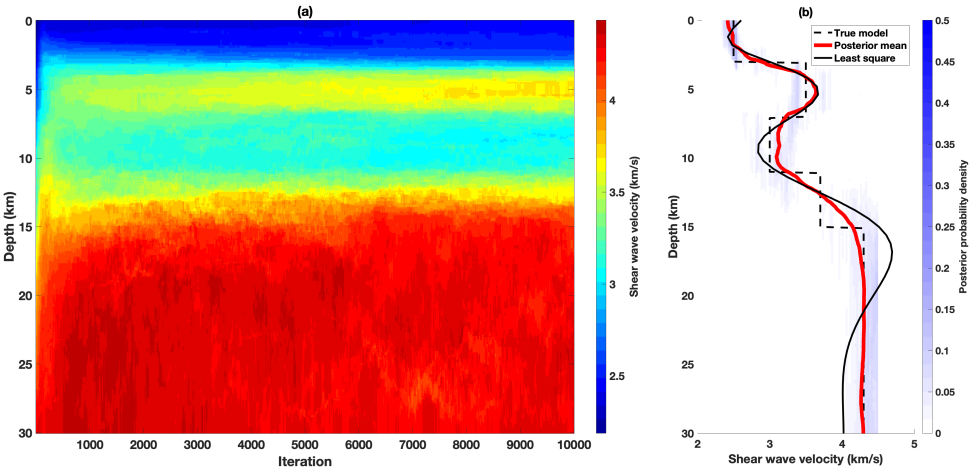

Figure 2.9. *As Figure 2.8, but using 10 variable cells.*

By assuming a minimal prior knowledge of velocity, cell nucleus position, and the number of cells, using a uniform prior distribution, and knowing that the velocity and cell nucleus position are independent in each cell, the prior for a 1D problem can be calculated by (Bodin & Sambridge, 2009):

$$p(\mathbf{m}) = \frac{1}{\Delta n} \frac{n!(N-n)!}{N!} \left(\frac{1}{\Delta v}\right)^n, \tag{2.19}$$

where $\Delta n = n_{max} - n_{min}$, n_{max} is the maximum allowed number of cells and n_{min} is the minimum allowed number of cells. Here, number of cells, n, is variable. Hence, the acceptance ratio (Equation 2.13) deviates from Equation 2.16.

The reversible jump algorithm employs four distinct perturbation types of model parameters: *update* for velocity, *move* for cell nuclei, *death* for cell removal, and *birth* for cell addition. In the *update* step, the velocity of a randomly selected cell is perturbed, the *move* step alters the nucleus position of a randomly selected cell, the *death* step eliminates a randomly selected cell nucleus, and the *birth* step adds a cell to the current model.

For perturbation types that do not induce a change in dimension (specifically, *update* for velocity and *move* for cell), the number of cells remains fixed. Consequently, like the partition modeling scenario, the prior ratio, proposal ratio, and Jacobian term evaluate to one. Therefore, the acceptance ratio aligns with the partition modeling McMC and can be straightforwardly computed using Equation 2.16.

However, for the *death* step (involving a jump from dimension n in the current model $\mathbf{m}$ to $n-1$ in the proposed model $\mathbf{m}'$), the acceptance ratio is derived as (see Bodin & Sambridge, 2009):

$$\alpha(\mathbf{m}'|\mathbf{m}) = min\left[1, \frac{\Delta v}{\sigma_{bd}\sqrt{2\pi}} \exp\left(\frac{\phi(\mathbf{m}) - \phi(\mathbf{m}')}{2} - \frac{(v'_j - v_i)^2}{2\sigma_{bd}^2}\right)\right], \tag{2.20}$$

where σ_{bd} is a user-defined variance for the Gaussian proposal distribution, v_i is the velocity of the deleted cell i, and v'_j is the velocity at the location of the deleted cell in the new proposed model.

For the *birth* step (jump dimension from n in current model $\mathbf{m}$ to $n+1$ in proposed model $\mathbf{m}'$), the acceptance ratio is similarly derived as (see Bodin & Sambridge, 2009):

$$\alpha(\mathbf{m}'|\mathbf{m}) = min\left[1, \frac{\sigma_{bd}\sqrt{2\pi}}{\Delta v} \exp\left(\frac{\phi(\mathbf{m}) - \phi(\mathbf{m}')}{2} + \frac{(v'_{n+1} - v_i)^2}{2\sigma_{bd}^2}\right)\right], \tag{2.21}$$

where v_i is the velocity at the location of the added cell in the current model, and v'_{n+1} is the proposed velocity for the added cell in the new proposed model.

The flowchart for the transdimensional McMC inversion algorithm is depicted in Figure 2.10. Analogous to the partition modeling McMC, a transdimensional McMC chain starts with an initial (random) model, where the number of cells, the position of each cell, and the velocity assigned to each cell are generated randomly. Subsequently, the model undergoes perturbation by randomly selecting one of four perturbation types: *update*, *move*, *birth*, or *death*.

Figure 2.11 represents the results of the transdimensional McMC inversion for the synthetic data of Figure 2.1b considering an irregular grid of cells, which were allowed to vary between n_{min} = 3 and n_{max} = 50 cells. We ran 20 independent McMC chains, each generating 15,000 samples, with the initial 5,000 samples discarded as burn-in steps. Figure 2.11a shows the sampled models at different iterations for all chains. At each iteration, the samples from all 20 chains are aggregated and

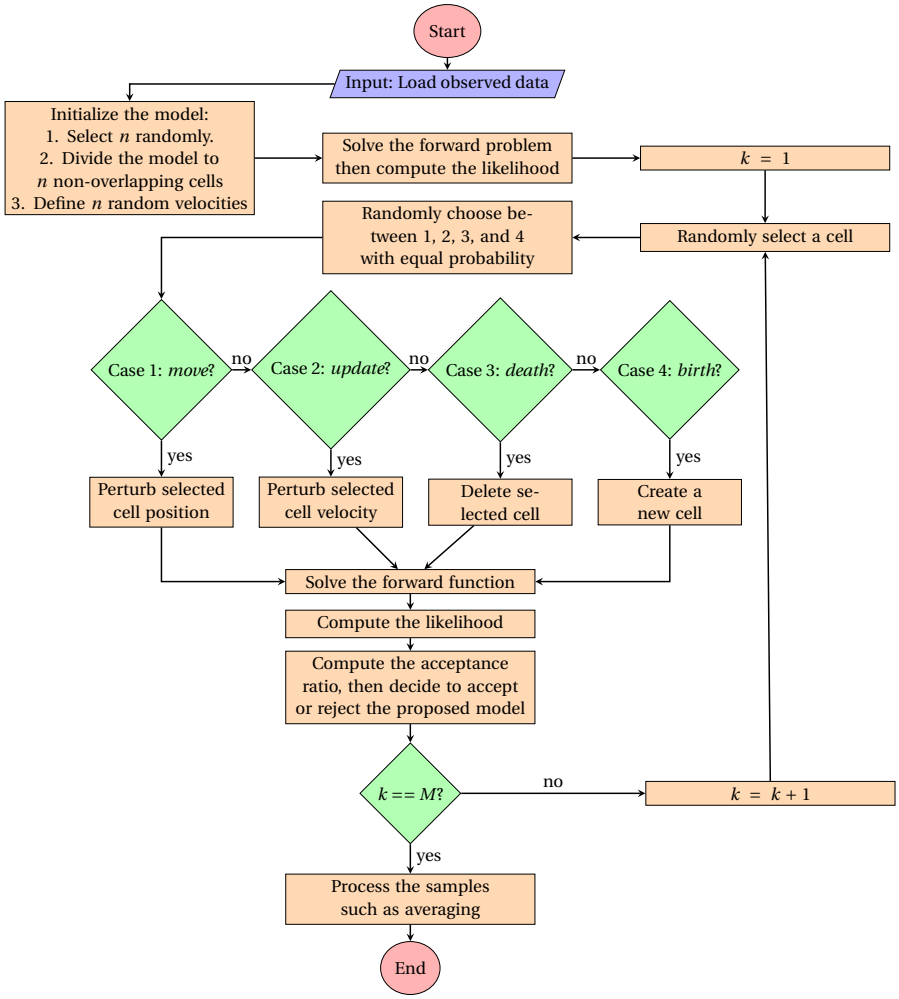

Figure 2.10. *Flowchart illustrating the Transdimensional McMC method for generating M samples, where the number of cells, their positions, and the assigned velocities are all unknown and variable.*

averaged to represent the collective set of samples. In Figure 2.11b, the true model, post-burn-in posterior mean, least-squares estimation, and the posterior probability density of the velocity model are presented. Notably, the pointwise posterior mean aligns reasonably well with the true model despite the overestimation of the velocity in the second layer. Looking at the samples depicted in Figure 2.11a implies that collecting more samples could effectively address the overestimated velocity in the second layer, as the velocity in the second layer decreases by iteration.

To evaluate the convergence of the transdimensional algorithm, we examined the variation in both misfit and the number of cells per iteration, as illustrated in

Figure 2.12a-b. It is evident that both parameters decrease until the 4000th iteration, indicative of the burn-in phase, after which they stabilize. To ensure a conservative approach, we excluded the initial 5000 steps as the burn-in phase. In Figure 2.12c, the histogram of the number of cells in post-burn-in samples is presented, representing the posterior probability density of the cell numbers. Notably, samples with a number of cells between 8-10 exhibit the highest probability. This observation sheds light on why the partition modeling McMC algorithm performed more effectively with 10 cells in Figure 2.9 compared to the scenario with 5 cells in Figure 2.8.

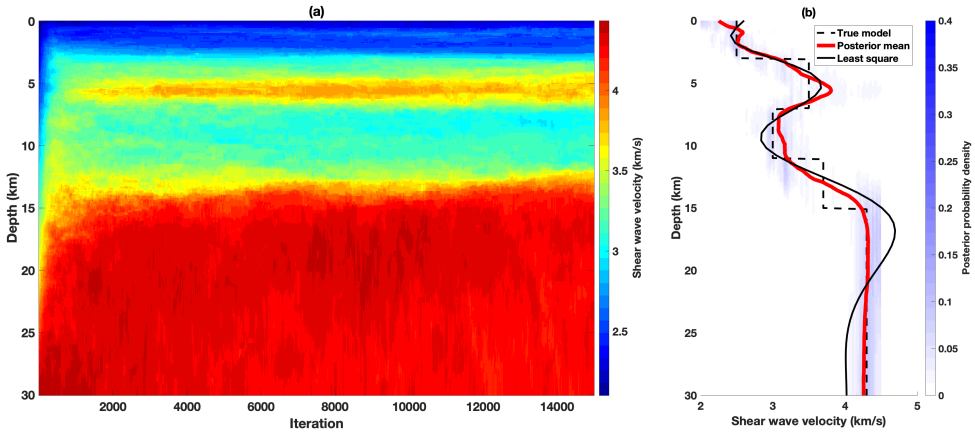

Figure 2.11. *Results of the transdimensional McMC. (a) The average of the accumulated samples is computed at each iteration, wherein the sampled models from 20 chains are superimposed and averaged to collectively represent all samples. (b) True model (dashed black line), posterior mean (red), least-squares solution (black) as in Figure 2.3c, and the posterior probability density (white-blue colored histogram).*

2.5 Field data example

To illustrate the functionality of the nonlinear least-squares and the transdimensional McMC algorithms with field data, we applied them to an average DC computed from ambient noise data recorded both on- and off-shore of the Reykjanes Peninsula. Details about the data retrieval process can be found in Weemstra et al. (2021), or in sections 5.3 and 5.4 of this thesis. Figure 2.13 displays the average DC along with its corresponding uncertainty, which is computed using all available DCs at each frequency. In the inversion algorithms, we used the average DC as the input data ($\mathbf{d}_{obs}$ in Equation 2.11), and the standard deviation served as the data uncertainty ($\sigma_{\mathbf{d}}$ in Equation 2.11).

Figure 2.14 illustrates the application of the least-squares inversion algorithm (i.e., the GN method) to the average dispersion curve of the Reykjanes Peninsula. Initially, by assuming $\eta = 0$, we determined the minimum damping factor λ for

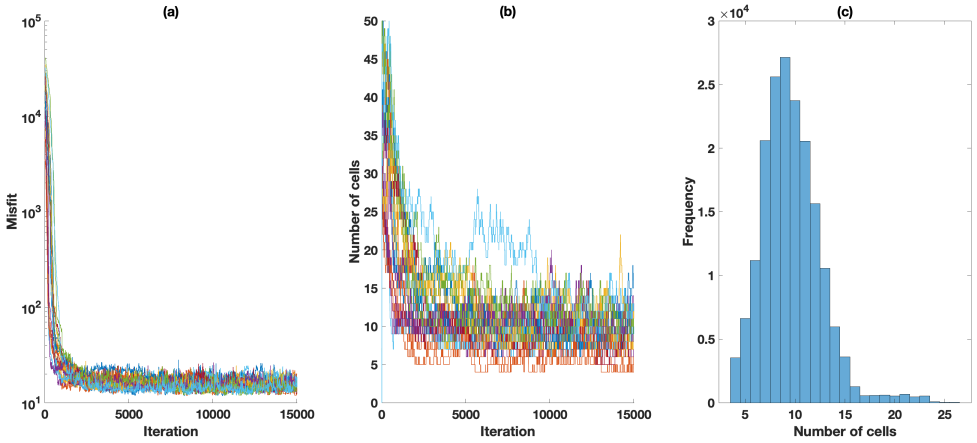

Figure 2.12. *The transdimensional McMC chains statistics. (a) Misfit variation. (b) Number of cells variation. (c) Number of cells posterior probability density. Different colors in (a-b) represents different chains.*

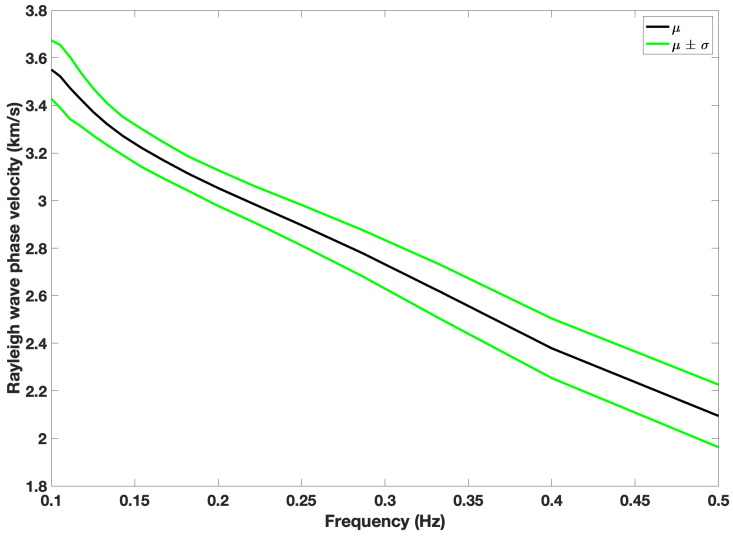

Figure 2.13. *An average dispersion curve (μ; black curve), which is computed by all available dispersion curves retrieved from cross-correlated noise recorded at various stations on the Reykjanes peninsula. The green curves show $\mu \pm \sigma$, where σ is the standard deviation. All the available dispersion curves are presented in Figure 5.3a.*

Equation 2.8 to remain stable and converge; the optimal λ was found to be $\lambda = 1$. Subsequently, employing the L-curve method (Figure 2.14a), we identified the optimum smoothing parameter η as $\eta = 0.67$. The modeled dispersion curve at each iteration is depicted in Figure 2.14b, highlighting a close fit of the final dispersion curve to the input average dispersion curve. Figure 2.14c showcases the inverted model at various iterations, revealing the algorithm's convergence to a smooth velocity model consistent with the known geological setting of the study area. Further details on the geological setting are provided in section 5.2, and for an interpretation of the inverted model, refer to section 5.5.3.

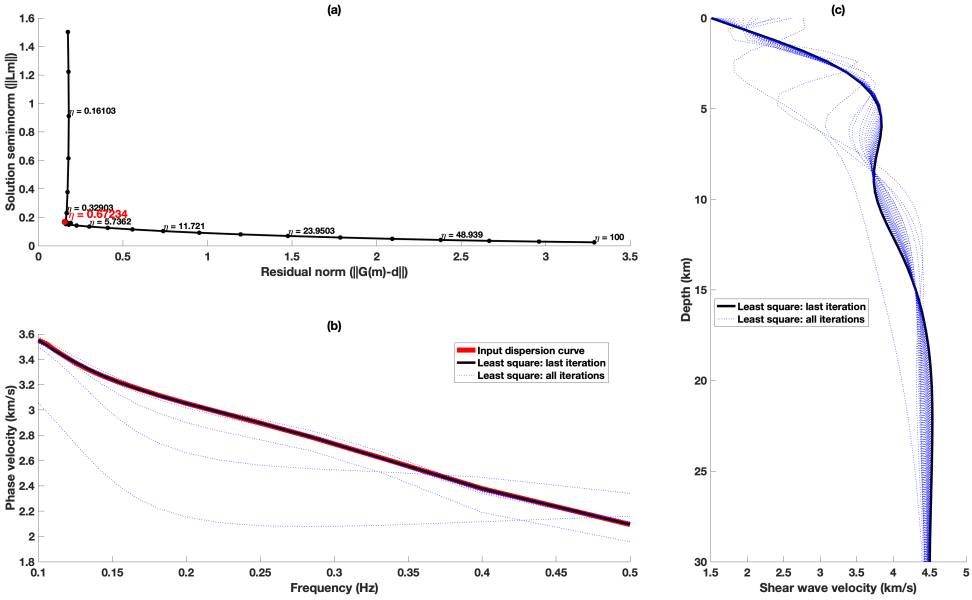

Figure 2.14. *The regularized GN method for the inversion of the Reykjanes Peninsula average dispersion curve. (a) The L-curve to find the optimum smoothing parameter η. (b) The input DC (red) and the modeled DCs (dotted blue) at different iterations of the inversion algorithm. (c) The true shear wave velocity model (dashed black) and the inverted shear wave velocity model (dotted blue) at different iterations of the inversion and the final inverted model (black solid).*

Figure 2.15 illustrates the application of the transdimensional Markov chain Monte Carlo (McMC) algorithm to the average Dispersion Curve (DC) of the Reykjanes Peninsula. Similar to the synthetic data case, we used 20 independent chains with a variable number of cells ranging from n_{min} = 3 and n_{max} = 50. Each chain generated 15,000 samples, and the initial 5,000 samples were discarded as the burn-in phase. In Figure 2.15a, the sampled models at different iterations for all chains are displayed. At each iteration, samples from all 20 chains are aggregated and averaged to represent the collective set of samples.

Figure 2.15b presents the post-burn-in pointwise-averaged posterior mean, least-squares estimate, and the posterior probability density of the velocity model. The pointwise-averaged posterior mean is smooth due to the inherent high uncertainty resulting from averaging DCs over a large study area. This smoothing effect is also evident in the least-squares inverted model. In contrast to the least-squares method, the transdimensional algorithm successfully recovered sharp variations in velocity, particularly at a depth of around 3 km. This observation emphasizes the automatic and localized smoothing applied in the transdimensional McMC algorithm. Furthermore, the transdimensional McMC algorithm provides an informative posterior probability density, offering valuable insights.

Finally, Figure 2.16 presents two statistical measures of the sampling chains. Figures 2.16a-b show the variation in misfit and number of cells, respectively. Both parameters stabilize after around 2000 iterations indicating the burn-in phase. However, we discarded the first 4000 iterations as the burn-in to be on the safe side. Figure 2.16c shows the histogram of the number of cells in the post-burn-in samples. Notably, lower number of cells have higher probabilities. This is due to the high noise level introduced as the input data.

Finally, in Figure 2.16, two key statistical measures of the sampling chains are presented. Figures 2.16a-b depict the variation in misfit and the number of cells, respectively. Both parameters stabilize after approximately 2000 iterations, indicating the end of the burn-in phase. However, to stay on the safe side, we chose to discard the first 4000 iterations as the burn-in period. Figure 2.16c displays the histogram of the number of cells in the post-burn-in samples. Notably, a lower number of cells have higher probabilities, which can be attributed to the high noise level introduced in the input data.

2.6 Conclusion

In this chapter, we delved into a comprehensive exploration of transdimensional inversion, a Bayesian algorithm. We discussed the efficiency, stability, and self-regularization capabilities of the transdimensional algorithm, and compared it with conventional techniques such as a nonlinear least-squares inversion and a conventional McMC algorithm with fixed parametrization.

The challenges associated with a nonlinear least-squares inversion algorithm were discussed, shedding light on issues such as the need for precise parametrization, and regularization. The discussion acknowledged the sensitivity of this algorithm to the initial guess (model) and the risk of getting stuck in local minima.

The conventional McMC method with fixed parametrization, was identified as relatively inefficient, particularly in scenarios with numerous model parameters. In contrast, partition modeling McMC emerged as a viable alternative, with its self-parametrizing nature and natural smoothing characteristics. However, challenges related to the user's decision on the optimal number of cells were acknowledged. Transdimensional McMC was introduced as an evolution, allowing the number of unknowns to be a variable. Its ability to simultaneously determine the number of cells, their positions, and the velocity field showcased a higher level of adaptability.

Finally, we discussed the application of the nonlinear least-squares algorithm

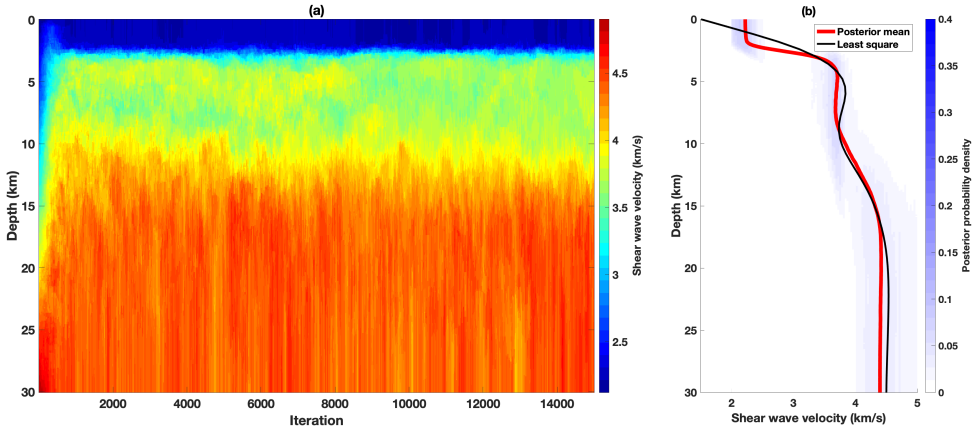

Figure 2.15. *Results of the transdimensional McMC applied to the average DC of the Reykjanes Peninsula. (a) The average of the accumulated samples is computed at each iteration, wherein the sampled models from 20 chains are superimposed and averaged to collectively represent all samples. (b) Posterior mean (red), least-squares solution (black) as in Figure 2.14c, and the posterior probability density (white-blue colored histogram).*

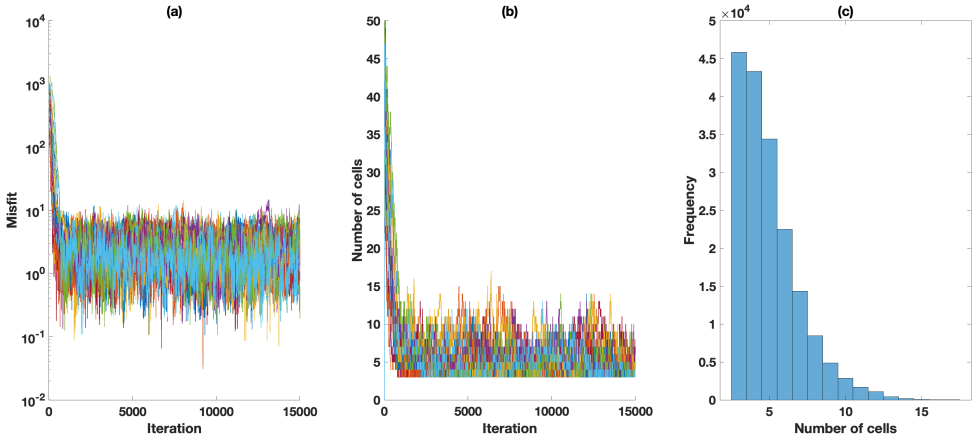

Figure 2.16. *The transdimensional McMC chains statistics. (a) Misfit variation. (b) Number of cells variation. (c) Number of cells posterior probability density. Different colors in (a-b) represent different chains.*

and the transdimensional McMC method to field data from the Reykjanes Peninsula. We assessed the results of both methods in reconstructing the subsurface velocity structure. Notably, transdimensional McMC stood out, displaying automatic and localized smoothing, showcasing superior adaptability compared to the uniform smoothing inherent in regularized least-squares inversions.

In conclusion, the exploration of transdimensional inversion and its comparison

with traditional methods with fixed parametrization underscores the need for more flexible and adaptive Bayesian inversion algorithms in seismic tomography. The potential efficiency gains, self-regularization capabilities, and adaptability to complex model spaces position transdimensional McMC as a promising tool for advancing our understanding of subsurface structures. As we navigate the challenges posed by conventional methods, embracing innovative approaches becomes imperative for pushing the boundaries of seismic inversion research.

3

2D surface wave inversion: near-surface application using distributed acoustic sensing

Abstract: Distributed Acoustic Sensing (DAS) is a novel technology which allows the seismic wavefield to be sampled densely over a broad frequency band. This makes it an ideal tool for surface wave studies, which are predominantly sensitive to the shear wave velocity structure of the subsurface. In this study, we evaluate the potential of DAS to image the near-surface using active-source surface waves recorded with straight fibers on a field in the province of Groningen, the Netherlands. Importantly, DAS is used here in conjunction with a Bayesian transdimensional inversion approach, making this the first application of such an algorithm to DAS-derived wavefields. First, we recover laterally varying surface wave phase velocities (i.e., "local" dispersion curves) from the fundamental mode surface waves. We utilize the multi-offset phase analysis (MOPA) for this purpose. MOPA allows us to take into account the lateral variability of the subsurface shear wave velocity. Then, instead of inverting each local dispersion curve separately, we use a novel 2D transdimensional algorithm to estimate the subsurface's shear wave velocity structure. The transdimensional approach involves parameterization of the model space using 2D Voronoi cells. As such, all dispersion curves are included simultaneously, preserving the lateral correlation of the shear wave velocity structure. In addition, this approach does not suffer from non-uniqueness, which is a well-known problem of tomographic inversions. We first validate our approach by successfully recovering the shear wave velocity in a synthetic experiment. Application

An initial draft of this chapter has been published as:
Rahimi Dalkhani, A., Hasani, M. A. A., Drijkoningen, G., & Weemstra, C. (2023). Transdimensional surface wave tomography of the near-surface: Application to DAS data, https://doi.org/10.48550/arXiv.2304.10678.
The current version is submitted to "*Geophysics*" for consideration and potential publication.

to the field data then confirms the reliability of the proposed algorithm. The recovered 2D shear wave velocity section is compared to shear wave velocity logs obtained along two boreholes positioned at two separate locations along the fiber, and shows reasonable agreement with these two 1D profiles.

3.1 Introduction

After initial Distributed Acoustic Sensing (DAS) field trials (Paulsson et al., 1997; Bostick III, 2000; Molenaar et al., 2012; Johannessen et al., 2012), the technique was investigated and applied in the context of a variety of geophysical problems (e.g., Daley et al., 2013; Lindsey et al., 2017; Barone et al., 2021; Mata Flores et al., 2023). Due to the dense sampling of the wavefield and its broadband character, DAS has also become popular to sample surface waves; both in active (e.g., Qu et al., 2023; Yust et al., 2023) and passive (e.g., Ajo-Franklin et al., 2019; Nayak et al., 2021) surveys. Surface waves are useful because of their wave speed's sensitivity to the subsurface's shear wave velocity.

A material's shear wave velocity is to a large extent determined by its shear strength (or stiffness). Consequently, the shear wave velocity of the near-surface is a valuable parameter in many subsurface engineering applications. And because the velocity of surface waves strongly depends on that shear wave velocity, near-surface shear wave velocity models are frequently derived from surface wave measurements (Socco et al., 2010). Typically, two types of surface waves are recorded: Rayleigh and Love waves (Aki & Richards, 2002). Surface waves are dispersive when the shear wave velocity varies as a function of depth, meaning that different frequencies propagate with different velocities. A surface wave's propagation velocity at an individual frequency is referred to as that frequency's "phase velocity". The first step in surface wave imaging is therefore usually the retrieval of the frequency-dependent phase velocities. An inversion subsequently results in a model of the shear wave velocity as a function of depth (Schaefer et al., 2011; Zhang et al., 2020).

Conventionally, in an active-source surface wave analysis, a dispersion curve is retrieved from each common shot record using Multichannel Analysis of Surface Waves (MASW; Park et al., 1999) assuming that the subsurface is a stack of horizontal layers. Then, an inversion algorithm is used to recover a 1D shear wave velocity profile (e.g., Vantassel et al., 2022; Qu et al., 2023). Due to the dense spatial sampling and the high-frequency content of active-source DAS surveys, however, the lateral resolution could in principle be increased significantly (Barone et al., 2021). Consequently, to account for the lateral variation of the subsurface's velocity structure, many authors suggested recovering local dispersion curves (DCs) (e.g., Neducza, 2007; Luo et al., 2008; Vignoli et al., 2011; Barone et al., 2021). These local DCs can then be used in an inversion algorithm to recover a 2D profile (or 3D cube) of the subsurface shear wave velocity (Vignoli et al., 2016; Barone et al., 2021).

Several approaches have been proposed to recover lateral variations of the subsurface's shear wave velocity, most of them based on laterally varying dispersion curves. The most common approach involves the application of a moving window to the recorded shot gathers in the time-space domain (e.g., Bohlen et al., 2004; Luo et al., 2008; Socco et al., 2009; Boiero & Socco, 2010). The windowed part of the data

is then transformed into a spectral domain to estimate the "local" dispersion curve at the location of the center of that window. Alternatively, multi-offset phase analysis (MOPA; Vignoli et al., 2016) can be used to recover lateral variations (Barone et al., 2021). Vignoli et al. (2016) and Barone et al. (2021) successfully retrieved laterally varying fundamental mode dispersion curves using MOPA. Then, they inverted these local dispersion curves at each location independently to recover a 2D shear wave velocity pseudo-section of the subsurface. It is worth noting that both studies (Vignoli et al., 2016; Barone et al., 2021) applied the MOPA algorithm to geophone recordings.

In this study, we apply the MOPA algorithm to surface waves extracted from a 2D, active-source DAS survey. As such, we recover the laterally varying fundamental mode local phase velocities. Importantly, we then "invert" all the dispersion curves simultaneously using a non-linear 2D transdimensional tomographic algorithm (Bodin & Sambridge, 2009). This transdimensional inversion algorithm was originally developed for surface wave travel time tomography. Later, it has been applied to many geophysical problems (e.g., Dettmer et al., 2012; Ghalenoei et al., 2022; Yao et al., 2023). Here, we adapt the algorithm to invert (MOPA-derived) dispersion curves extracted from active-source surface waves recorded with DAS. This allows us to generate a 2D shear wave velocity image (vertical cross-section) of the subsurface with improved lateral correlation. We validate the obtained 2D shear wave velocity section using shear wave velocity logs obtained from two boreholes located at two specific points on the acquisition line.

3.2 Theory & methodology

In this section, we detail the various methods used in this study. First, we describe how the surface waves are extracted from the fiber optic recordings. Subsequently, we explain how we locally estimate the surface waves' phase velocity as a function of frequency. Finally, we provide the details of the McMC implementation.

3.2.1 Distributed acoustic sensing (DAS)

In this part, we describe the physical quantity measured by DAS and how it relates to geophone measurements. Unlike geophones, which are point sensors that record the particle velocity at a specific location, DAS effectively yields strain rate along the fiber optic cable, i.e. $\dot{\varepsilon}_{xx} = \partial_t(\partial_x u_x)$, averaged over a specific distance called the gauge length (L_g). Alternatively, DAS recordings can be represented by the spatial derivative of the particle velocity vector, i.e. $\partial_x(\partial_t u_x) = \partial_x V_x$ (Daley et al., 2016).

In Figure 3.1 we depict a schematic illustrating a scenario mimicking our field experiment. A vertical force source F_z will excite different types of waves of which the Rayleigh waves will be the most energetic at the Earth's surface. As DAS relies on the elongation and contraction of the fiber as a function of time, its maximum sensitivity is in the axial direction. It is therefore safe to say that the majority of the energy that is being recorded is associated with the horizontal component of the Rayleigh waves. To compare geophone recordings to DAS recordings, we consider horizontal component (x) geophones separated by a distance dx. As a function of

time, these geophones sample the horizontal particle velocity V_x at $x - dx/2$ and $x + dx/2$, respectively. The equivalent DAS response between the two geophones can be estimated as the spatial derivative of the particle velocity using the following expression (adapted from Zulic et al., 2022):

$$\dot{\varepsilon}_{xx}\left(x - \frac{dx}{2}, x + \frac{dx}{2}\right) \approx \frac{V_x\left(x + \frac{dx}{2}\right) - V_x\left(x - \frac{dx}{2}\right)}{dx}, \tag{3.1}$$

where $\dot{\varepsilon}_{xx}$ is estimated to be the average strain rate obtained by DAS and dx is equivalent to the gauge length L_g of the DAS measurement.

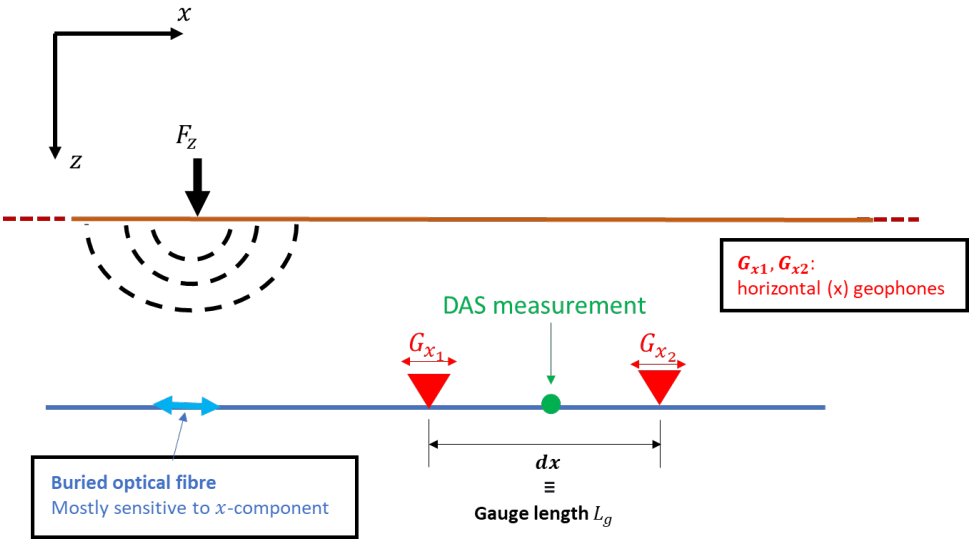

Figure 3.1. *An illustration to compare DAS and geophone measurements.*

3.2.2 Phase velocity retrieval

A variety of methods exist to retrieve a surface wave mode's dispersion curve. The dispersion curve describes the mode's phase velocity as a function of frequency. Often, dispersion curves are estimated by transforming the data into a different (spectral) domain. For example, the recorded data can be transformed from the time-space domain to the phase velocity-frequency ($cp - f$; McMechan & Yedlin, 1981) domain, to the frequency-wavenumber ($f - k$; Foti et al., 2000) domain, or to the phase-offset ($\phi - x$; Strobbia & Foti, 2006) domain. These methods have in common that they rely on the assumption that the subsurface is a stack of horizontal layers. In other words, the subsurface is assumed to be laterally invariant. Consequently, in the case of laterally rapidly varying structure, the retrieved dispersion relation is effectively a (non-exact) average (Boiero & Socco,

2010). In practice, these methods are still very useful when the subsurface is laterally smooth.

In case the subsurface is laterally invariant, the relation between the phase (ϕ) and offset (x) will be linear at each discrete frequency (f_i), with the slope coinciding with the wavenumber (k). This can be formulated as (Strobbia & Foti, 2006):

$$\phi(f_i, x) = k(f_i)x + \phi_0(f_i), \tag{3.2}$$

where ϕ_0 is the phase at the location of the source. Equation (3.2) allows the estimation of a wavenumber by means of a least-squares fit of the phase-offset data at each discrete frequency f_i, i.e., using a linear regression (for detailed formulation see Strobbia & Foti, 2006). The estimated wavenumber ($k(f_i)$) can be translated to the frequency-dependent phase velocity ($cp(f_i)$) using:

$$cp(f_i) = \frac{2\pi f_i}{k(f_i)}, \tag{3.3}$$

where $i = 1, 2, ..., N_f$, and N_f denotes the number of discrete frequencies. This approach is referred to as the "multi-offset phase analysis" (MOPA; Strobbia & Foti, 2006; Vignoli & Cassiani, 2010).

In the presence of (smooth) lateral variations, Equation (3.2) can be formulated such that the wavenumber k varies as a function of both offset and frequency. That is, $k = k(f_i, x^{(c)})$, where $x^{(c)}$ denotes the center position of a set of adjacent (Fourier transformed) wavefield recordings running from $x^{(c)} - W/2$ to $x^{(c)} + W/2$ (here, W is the spatial window along which $k(f_i, x^{(c)})$ is assumed to be constant). Vignoli et al. (2011) "move" this spatial window along the recording line with small steps (i.e., significantly smaller than W). This is done separately for each discrete frequency, allowing W to be frequency dependent (Vignoli et al., 2016). The wavenumbers are subsequently derived using linear regression according to Equation (3.2). These laterally varying wavenumbers are then converted to laterally varying phase velocities $cp(f_i, x^{(c)})$ using Equation 3.3. Since the lateral resolution of the surface waves is directly related to the wavelength (Barone et al., 2021), Vignoli et al. (2016) proposed to have the spatial window length W be a function of the wavelength of the surface waves.

In this study, we use the MOPA algorithm of Vignoli et al. (2016) to estimate local dispersion curves. Chiefly, this is because of the algorithm's robustness and simplicity. A drawback of the MOPA algorithm, however, is that it can only be applied to a single surface wave mode. Therefore, only one mode will be considered, and other (potential) surface wave modes will be muted. Finally, it should be understood that the recovered wavenumbers are associated with the wavefield. That is, they will deviate from the medium's true wavenumber distribution (sometimes referred to as "structural wavenumbers"; Wielandt, 1993), with the discrepancy between the two being larger for more heterogeneous subsurfaces.

3.2.3 Transdimensional surface wave tomography

A single dispersion curve, i.e., $cp(f_i, x^{(c)})$ for a specific location $x^{(c)}$ (with $i = 1, 2, ..., N_f$), can be "inverted" to recover a (1D) shear wave velocity profile.

Numerous inversion algorithms are described in the literature. Roughly speaking, one can distinguish between linearized algorithms (e.g., Xia et al., 1999) and nonlinear global search methods. The latter includes genetic algorithms (Yamanaka & Ishida, 1996), simulated annealing (Beaty et al., 2002), the neighborhood algorithm (Wathelet, 2008), Monte Carlo methods (Socco & Boiero, 2008), particle swarm optimization (Wilken & Rabbel, 2012), and a 1D transdimensional algorithm (Bodin et al., 2012).

In the presence of lateral variations, the dispersion relation varies as a function of location. In that case, the different dispersion curves are often inverted independently using one of the mentioned 1D inversion algorithms (e.g., Bohlen et al., 2004; Socco et al., 2009; Vignoli et al., 2016; Barone et al., 2021), after which the independently inverted 1D profiles are pieced together to obtain a 2D (or 3D) shear wave velocity pseudo-section (or pseudo-cube). However, by independently inverting the adjacent dispersion curves, lateral correlations in the subsurface structure are ignored (Zhang et al., 2020). Socco et al. (2009) propose to invert all dispersion curves simultaneously to mitigate the solution's non-uniqueness, and retain lateral smoothness. They use a laterally constrained least-squares algorithm in which each 1D model is linked to its neighbors. Zhang et al. (2020) invert all dispersion curves simultaneously using a (Bayesian) 3D transdimensional algorithm. In this study, we invert all $cp(f_i, x^{(c)})$ simultaneously using a 2D transdimensional algorithm (Bodin & Sambridge, 2009). As such, we retain lateral correlations of the shear wave velocity and circumvent (rather arbitrary) smoothing and damping procedures (e.g., Xia et al., 1999).

The 2D transdimensional tomographic algorithm by Bodin & Sambridge (2009) is developed for surface wave travel time tomography (for individual discrete frequencies). Here, we modify the algorithm to invert all DAS-derived dispersion curves simultaneously. Our transdimensional algorithm uses a 2D Voronoi tessellation to parameterize the subsurface, in combination with a reversible jump Markov chain Monte Carlo (rjMcMC) approach. A single unique model is defined by the number of Voronoi cells, their nuclei, and the shear wave velocity assigned to them. Note that the location of an individual Voronoi cell is defined by the location of its nucleus, and that its geometry is controlled by its neighboring cells. As such, it allows a variable parameterization of the subsurface, meaning that the number of Voronoi cells, their locations, and the assigned velocities are all unknowns. Because the number of variables is a variable itself, this algorithm is referred to as "transdimensional" (Bodin & Sambridge, 2009). The transdimensional parameterization allows the algorithm to sample the posterior, without the need to introduce any kind of regularization (Bodin & Sambridge, 2009). Effectively, the regularization is inherent in the algorithm.

The transdimensional algorithm is a Bayesian inference method that aims to sample the posterior probability density (henceforth simply "posterior") of the model parameters given the observed data, $p(\mathbf{m}|\mathbf{d})$. The posterior is proportional to the product of the likelihood $p(\mathbf{d}|\mathbf{m})$ and the prior $p(\mathbf{m})$ (Bodin & Sambridge, 2009; Tarantola, 2005):

$$p(\mathbf{m}|\mathbf{d}) \propto p(\mathbf{d}|\mathbf{m})\, p(\mathbf{m}). \tag{3.4}$$

The prior probability distribution, $p(\mathbf{m})$, incorporates all (a priori) known

independent information about the model space. Similar to Bodin & Sambridge (2009), we consider an (uninformative) uniform prior for all model parameters (i.e., number of cells, Voronoi nuclei location, and velocity assigned to each cell).

The likelihood function $p(\mathbf{d}|\mathbf{m})$ plays a fundamental role in the inference of the model space as it quantifies the probability of the observed laterally varying dispersion curves given a specific velocity model. Assuming the likelihood to be Gaussian, it is formulated as:

$$p(\mathbf{d}|\mathbf{m}) = A \exp\left(-\frac{\phi(\mathbf{m})}{2}\right), \tag{3.5}$$

where A is a normalization factor and $\phi(\mathbf{m})$ a simple least-squares misfit ($\phi(\mathbf{m}) = ||\frac{\mathbf{g}(\mathbf{m})-\mathbf{d}}{\sigma}||^2$). In our case, Equation 3.5 reads

$$p(\mathbf{d}|\mathbf{m}) = \prod_{i=1}^{N_f}\prod_{j=1}^{N_x}\left(\frac{1}{\sqrt{2\pi}\sigma_{ij}}\exp\left(-\frac{\left(g_{ij}(\mathbf{m})-d_{ij}\right)^2}{2\sigma_{ij}^2}\right)\right), \tag{3.6}$$

where N_x is the number of locations $x_j^{(c)}$ for which a dispersion curve is estimated (i.e., $j = 1, 2, ..., N_x$). Data point d_{ij} is the phase velocity at discrete frequency f_i and location $x_j^{(c)}$ (Figure 3.3e). The vector $\mathbf{m}$ contains the parameters describing the proposed model. Due to the variable number of Voronoi cells, its length (or its "dimension") changes while the posterior is being sampled. Furthermore, g_{ij} is the modeled laterally varying phase velocity and σ_{ij} is the data uncertainty for the phase velocity at discrete frequency f_i and location $x_j^{(c)}$.

It is worth noting that the input data in our case (i.e., laterally varying, frequency-dependent phase velocities along a 2D line) is different from the travel times used in Bodin & Sambridge (2009). Consequently, a different forward function (g in Equation 3.6) is necessary to compute the modeled data. For this purpose, we use a MATLAB package developed by Wu et al. (2019) using the reduced delta matrix method proposed in Buchen & Ben-Hador (1996). This algorithm computes the dispersion curve (i.e., phase velocity versus frequency) in a 1D earth model. Therefore, to model the laterally varying dispersion curves, we take the 1D velocity profile at each location and compute the dispersion curves independently. It should be understood, however, that these dispersion curves are not uncorrelated: the correlation between "adjacent" dispersion curves results from the Voronoi partitioning.

Reversible jump Markov chain Monte Carlo algorithm

The reversible jump Markov chain Monte Carlo (rjMcMC) algorithm draws samples from the posterior distribution employing a Metropolis-Hasting (MH) algorithm which includes changing the dimension of the model space. The process starts with some random initial model $\mathbf{m}$. Then, the algorithm draws the next sample of the chain by proposing a new model, $\mathbf{m}'$, based on a known proposal probability function, $q(\mathbf{m}'|\mathbf{m})$, which only depends on the previous state of the model $\mathbf{m}$. The

proposed model $\mathbf{m}'$ will be accepted with probability (Bodin & Sambridge, 2009):

$$\alpha(\mathbf{m}'|\mathbf{m}) = \min\left[1, \frac{p(\mathbf{m}')}{p(\mathbf{m})}\frac{p(\mathbf{d}|\mathbf{m}')}{p(\mathbf{d}|\mathbf{m})}\frac{q(\mathbf{m}|\mathbf{m}')}{q(\mathbf{m}'|\mathbf{m})} \times |\mathbf{J}|\right], \tag{3.7}$$

where, $\frac{p(\mathbf{m}')}{p(\mathbf{m})}$ is the prior ratio, $\frac{p(\mathbf{d}|\mathbf{m}')}{p(\mathbf{d}|\mathbf{m})}$ the likelihood ratio, $\frac{q(\mathbf{m}|\mathbf{m}')}{q(\mathbf{m}'|\mathbf{m})}$ the proposal ratio, and $\mathbf{J}$ the Jacobian associated with the transformation from $\mathbf{m}$ to $\mathbf{m}'$. The latter is needed to account for scale changes involved when the perturbation involves a jump between dimensions (Green, 1995).

The acceptance probability, $\alpha(\mathbf{m}'|\mathbf{m})$, is the key to ensuring that the samples will be generated according to the target posterior distribution, $p(\mathbf{m}|\mathbf{d})$. Similar to Bodin & Sambridge (2009), we use four perturbation types to propose a new model ($\mathbf{m}'$) based on the current model ($\mathbf{m}$). These are nuclei *move*, velocity *update*, *birth*, and *death* steps. We parameterize the subsurface using the aforementioned (2D) Voronoi tesselation. An example of a Voronoi partitioned model is depicted in Figure 3.4b. As derived in Bodin & Sambridge (2009), the acceptance probability in case of a *move* or *update* step (i.e., no change in model dimension) reads,

$$\alpha(\mathbf{m}'|\mathbf{m}) = \min\left[1, \exp\left(\frac{\phi(\mathbf{m}) - \phi(\mathbf{m}')}{2}\right)\right]. \tag{3.8}$$

Note that this acceptance probability only depends on the likelihood ratio, since (i) the priors for $\mathbf{m}$ and $\mathbf{m}'$ coincide for models of the same dimension and (ii) the proposal distribution is symmetrical if the dimension of the model space stays the same (i.e., $q(\mathbf{m}'|\mathbf{m}) = q(\mathbf{m}|\mathbf{m}')$; Bodin & Sambridge, 2009).

In case of *birth* and *death* steps, the dimension of the proposed model differs from the dimension of the current model. Consequently, in contrast with the *update* and *move* steps, both the prior ratio and the proposal ratio do not evaluate to unity. Explicit expressions therefore need to be derived for the prior ratio and the proposal ratio.

For a *birth* step, we again follow Bodin & Sambridge (2009) and randomly select a point from an underlying finite (and dense) two-dimensional grid of N grid points. The proposal distribution governing the selection of this grid point is uniform within the two-dimensional spatial domain (approximately the distance of the DAS cable times the maximum depth at which the longest surface waves have sufficient sensitivity). A cell nucleus is subsequently placed in that grid point and a new shear wave velocity is assigned. Bodin & Sambridge (2009) draw this new shear wave velocity from a Gaussian proposal distribution centered at the current velocity of the randomly selected grid point. As such, they derive that the acceptance ratio for the *birth* step becomes,

$$\alpha(\mathbf{m}'|\mathbf{m}) = \min\left[1, \frac{\sigma_v\sqrt{2\pi}}{\Delta v}\exp\left(\frac{(v' - v_i)^2}{2\sigma_v^2} + \frac{\phi(\mathbf{m}) - \phi(\mathbf{m}')}{2}\right)\right], \tag{3.9}$$

where σ_v is the "width" of the Gaussian distribution used to propose the new velocity, Δv the prior range on velocity (i.e., the maximum shear wave velocity

considered minus the minimum shear wave velocity considered), v' the proposed shear wave velocity for the new cell, and v_i the velocity at the nucleus' location prior to birth.

A *death* step is the reverse of a *birth* step. It hence involves the random (uniform probability) selection of a grid point and subsequent elimination of the cell that contains it. For the *death* step, the acceptance ratio can be found to read (Bodin & Sambridge, 2009),

$$\alpha(\mathbf{m}'|\mathbf{m}) = \min\left[1, \frac{\Delta v}{\sigma_v\sqrt{2\pi}} \exp\left(\frac{-(v_i - v')^2}{2\sigma_v^2} + \frac{\phi(\mathbf{m}) - \phi(\mathbf{m}')}{2}\right)\right], \tag{3.10}$$

where v' is the velocity after death at the selected location and v_i the velocity of the cell that was killed.

A problem reported in the literature for the above birth/death proposals is the very low acceptance ratio (e.g., Dosso et al., 2014). This adversely affects the mixing of the transdimensional Markov Chain and the efficiency with which the model space is being sampled. For example, consider two adjacent Voronoi cells in an area barely sampled by the data. The poor sampling implies that the likelihood would barely change (because $\phi(\mathbf{m}) - \phi(\mathbf{m}') \approx 0$). Considering that the simplest model should be preferred in such cases (Occam's razor), one of these cells is desirably killed. If their velocities differ significantly ($|v' - v_i| > 3\sigma_v$), however, the chance that this happens is slim because of the very low value of the exponential term in Equation 3.10 (i.e., $\exp(-4.5) < 0.01$). The "inability" of a death step to kill such a cell (with anomalous velocity) delays the convergence of the algorithm.

To improve the acceptance probability of a birth/death step, several studies suggested proposing the velocity in a birth step using a uniform distribution over the prior range (e.g., Dosso et al., 2014; Xiang et al., 2018). This way the prior and proposal ratios cancel and the acceptance probability for both the *birth* and the *death* step will be equal to the likelihood ratio, that is (Dosso et al., 2014; Xiang et al., 2018):

$$\alpha(\mathbf{m}'|\mathbf{m}) = \min\left[1, \exp\left(\frac{\phi(\mathbf{m}) - \phi(\mathbf{m}')}{2}\right)\right]. \tag{3.11}$$

This formulation is shown to have a higher acceptance ratio (e.g., Dosso et al., 2014; Xiang et al., 2018). This can be understood by considering a region in the subsurface with low sensitivity to the input data. Any perturbation in that region results in a likelihood ratio close to unity and hence is likely to be accepted. Consequently, when the sampled data is not equally sensitive to all regions in the subsurface, most of the accepted births/deaths occur in areas of the subsurface with rather low sensitivity to the data. Contrary to the original birth/death proposal scheme, however, this formulation does not result in a preference over simpler models, whereas this is desirable. In the following section, we therefore introduce a modified birth/death step that enhances the acceptance ratio while at the same time having a clear preference over simpler models (i.e., a preference over larger cells in case the likelihood ratio coincides for two Voronoi configurations).

An improved birth/death scheme

For the birth step, we randomly (uniform probability) select a point in the subsurface and make that the nucleus of a new cell. This new cell modifies the shape of the neighboring cells and constitutes parts of these cells. We compute the spatial average velocity over the area of the proposed cell (before birth) using the dense underlying two-dimensional grid of N grid points. Specifically,

$$\overline{v}_i = \frac{\sum_{j=1}^{N_c} v_j}{N_c}, \tag{3.12}$$

where, $\overline{v}_i$ is the average velocity, N_c is the number of grid points captured by the proposed Voronoi cell, and v_j the velocity at the location of grid point j prior to birth. We, then propose a new velocity v' for the new cell using a Gaussian proposal distribution centered at $\overline{v}_i$ and with a width of σ_v. The proposal probability distribution associated with such a birth step reads

$$q(\mathbf{m}'|\mathbf{m}) = \frac{1}{N-n}\frac{1}{\sigma_v\sqrt{2\pi}}\exp\Big(-\frac{(v'-\overline{v}_i)^2}{2{\sigma_v}^2}\Big), \tag{3.13}$$

where n is the number of grid points already acting as a cell's nucleus (prior to birth).

A *death* step is the reverse of *birth* step. We therefore consider the probability of randomly selecting a point that is contained in the birth cell. This probability is the size of the birth cell divided by the size of the spatial extent of the model. Approximating the cell size by the number of grid points inside it (i.e., N_c), and the size of the spatial domain by the total number of grid points in the model (i.e., N), the probability of such a proposal is,

$$q(\mathbf{m}|\mathbf{m}') = \frac{\text{cell size}}{\text{domain size}} \approx \frac{N_c}{N}. \tag{3.14}$$

Using these two expressions, the proposal ratio for a birth step becomes

$$\left[\frac{q(\mathbf{m}|\mathbf{m}')}{q(\mathbf{m}'|\mathbf{m})}\right]_{\text{birth}} = \frac{N_c}{N}(N-n)\sigma_v\sqrt{2\pi}\exp\Big(\frac{(v'-\overline{v}_i)^2}{2{\sigma_v}^2}\Big). \tag{3.15}$$

And just as in Bodin & Sambridge (2009), the Jacobian coincides with unity for a *birth/death* step.

Substituting the prior ratio for a birth step (as derived by Bodin & Sambridge, 2009),

$$\left[\frac{p(\mathbf{m}')}{p(\mathbf{m})}\right]_{\text{birth}} = \frac{n+1}{N-n}\frac{1}{\Delta v}. \tag{3.16}$$

Equation (3.15), and the likelihood ratio (computed using Equation (3.6)) in Equation (3.7), gives for the acceptance probability of a *birth* step:

$$\alpha(\mathbf{m}'|\mathbf{m}) = \min\left[1, \frac{n+1}{\Delta v}\frac{N_c}{N}\sigma_v\sqrt{2\pi}\exp\left(\frac{(v'-\overline{v}_i)^2}{2\sigma_v^2} + \frac{\phi(\mathbf{m})-\phi(\mathbf{m}')}{2}\right)\right], \tag{3.17}$$

where v' is the velocity of the new cell, and $\overline{v}_i$ is the spatially averaged velocity in the area constituting the new cell before its birth. A death step is the reverse of the birth step, following a similar procedure as above, we find the acceptance probability of a death step:

$$\alpha(\mathbf{m}'|\mathbf{m}) = \min\left[1, \frac{\Delta v}{n}\frac{N}{N_c}\frac{1}{\sigma_v\sqrt{2\pi}}\exp\left(-\frac{(v'-\overline{v}_i)^2}{2\sigma_v^2} + \frac{\phi(\mathbf{m})-\phi(\mathbf{m}')}{2}\right)\right], \tag{3.18}$$

where v' is the velocity of the cell that was killed and $\overline{v}_i$ is the spatial average of the (new) velocities at the grid points that were located in that cell. One can see that the new formulation depends not only on the velocity of the *birth/death* cell but also on the size of the cell. It prefers giving birth to cells larger than the average size of all cells (i.e., $\frac{N_c}{N}$) and killing cells smaller than the average cell size. While creating a new cell or killing an available cell, the algorithm doesn't rely on the velocity of a single point (i.e., the cell nuclei) but considers the velocity of all points located inside the death/birth cell. This suppresses the effect of cells with anomalous velocities close to each other discussed in the previous section.

3

Noise parametrization and inference

The data uncertainty (σ_{ij} in Equation 3.6) plays a crucial role in the convergence of a Bayesian algorithm (Bodin et al., 2012). Ideally, this data uncertainty accounts for the uncertainty resulting from seismic noise as well as for the fact that the model used is a simplification of the true physics describing surface wave propagation. As we will explain in Section 3.4, the application of the MOPA algorithm to multiple shots provides us with an estimate of the data uncertainty (Figure 3.3d). This estimate, however, does not take into account the second source of data uncertainty (i.e., inaccuracy inherent in the forward function). For this reason, similar to Bodin et al. (2012), we consider this data uncertainty to be an unknown, and parameterize it as a linear relation:

$$\sigma_{ij} = a\sigma'_{ij}, \tag{3.19}$$

where σ'_{ij} is the uncertainty derived from the MOPA algorithm (Figure 3.3d) at location $x_j^{(c)}$ and discrete frequency f_i. Here, a is a hyperparameter to take into account data, processing, and modeling-related errors. Bodin et al. (2012) used an additional MH step to infer this hyperparameter from the data automatically.

Here, following Andrieu et al. (1999), we propose a Gibbs sampling step (Gilks et al., 1995; Yildirim, 2012) to infer the noise hyperparameter (a) efficiently. Gibbs sampling is a Markov chain that samples the posterior probability density of a parameter. It uses the conditional posterior distribution of the parameter with the remaining variables fixed to their current values (Yildirim, 2012). Accordingly, to sample the hyperparameter a, we need to derive its posterior distribution ($p(a|\mathbf{d})$) under the condition of the model $\mathbf{m}$. Applying Bayes' theorem, the posterior distribution ($p(a|\mathbf{d},\mathbf{m})$) is proportional to the product of the likelihood and the prior (Gelman et al., 2014):

$$p(a|\mathbf{d}) \propto p(\mathbf{d}|a)p(a), \tag{3.20}$$

where $p(\mathbf{d}|a)$ is the likelihood function introduced in Equation 3.6, and $p(a)$ is the prior on a. By substituting Equations 3.6 and 3.19 into Equation 3.20 and performing some algebraic manipulation (see appendix A.1 for the detailed derivation):

$$p(a|\mathbf{d}) \propto L\tau^{\alpha-1}\exp(-\beta\tau), \tag{3.21}$$

where,

$$\begin{aligned}
L &= p(a)\prod_{i=1}^{N_f}\prod_{j=1}^{N_x}\frac{1}{\sqrt{2\pi}\sigma'_{ij}},\\
\tau &= \frac{1}{a^2},\\
\alpha &= \frac{N_x N_f}{2}+1,\\
\beta &= \sum_{i=1}^{N_f}\sum_{j=1}^{N_x}\frac{\left(g_{ij}(\mathbf{m})-d_{ij}\right)^2}{2\sigma'^{\,2}_{ij}}.
\end{aligned}$$

Assuming a (non-informative) uniform prior to the noise hyperparameter, $p(a)$ is a constant. Therefore, L in Equation 3.21 is also independent of a. By having the exact formulation for the conditional posterior distribution of the noise hyperparameter, $a = \sqrt{1/\tau}$, we can simply sample the parameter posterior using a Gibbs sampler.

The Gibbs sampler is a special case of the MH algorithm: instead of accepting/rejecting a sample that is drawn from a proposal probability distribution, the Gibbs sampler draws a sample from the conditional posterior distribution of the desired parameter, Equation 3.21 in our case. Because of this, the proposed sample is always accepted (Geman & Geman, 1984). This makes the Gibbs sampler an efficient sampling algorithm for the introduced noise hyperparameter. We draw samples of the noise hyperparameter a using a Gibbs step after each iteration of the rjMcMC sampler. Equation 3.21 has the form of a Gamma distribution. The Gibbs sampler, then, becomes the generation of random samples from a Gamma distribution with the parameters given in Equation 3.21.

Compared to the MH step, the proposed Gibbs sampler is fast (no rejection) and unbiased. It doesn't need user-defined parameters except for a wide prior range for the hyperparameter a. The downside of the proposed algorithm compared to the MH step proposed by Bodin et al. (2012) is that the way we can parameterize the noise is limited. In other words, we can only assume that the noise level is a constant or it is a factor of a constant value like what we discussed (i.e., $\sigma = a\sigma'$, where σ' is known). If we want to parametrize the noise like $\sigma = a\sigma' + b$, then our proposed method is not working and the Metropolis-Hasting step proposed by Bodin et al. (2012) is applicable.

Constraining the inversion using (borehole) shear wave logs

It is possible to measure physical properties directly using borehole logging tools. In our case, two dedicated boreholes were drilled down to approximately 80 m depth. Using a P-S suspension logging tool, S wave velocities were measured using ~400

Hz shear waves. These shear wave velocity profiles can be incorporated into the transdimensional algorithm in two ways. First, the shear wave velocity profile can be used to constrain the prior probability and make it depth-dependent. This can be achieved by assuming a Gaussian distribution centered at the measured shear wave velocity profile (see for example Sen & Biswas, 2017). This approach, however, needs the rjMcMC algorithm to be modified. Additionally, it is difficult to define the prior mean in a Voronoi partitioned, variable parameterization of the model. An alternative approach is to use the shear wave velocity profiles to constrain the misfit function (see Wang, 2016, pp. 5) by the available data as:

$$\phi(\mathbf{m}) = \left\| \frac{\mathbf{g}(\mathbf{m}) - \mathbf{d}}{\sigma} \right\|^2 + \left\| \frac{\mathbf{V_m} - \mathbf{V_{ref}}}{\sigma_{bh}} \right\|^2, \tag{3.22}$$

where $\mathbf{V_m}$ is the shear wave velocity of the proposed model on a computational fine grid during McMC sampling and $\mathbf{V_{ref}}$ a reference shear wave velocity model defined on the same computational fine grid, but based on the available borehole data. σ is the data uncertainty, and σ_{bh} is the reference model uncertainty. A lower σ_{bh} imposes a stronger constraint on the exploration of the model space, whereas a larger σ_{bh} reduces this constraint. One can use a single (depth-independent) σ_{bh} to constrain the misfit function close to the borehole for the whole model or make it location-dependent. It depends on the level of information we have from the study area. In this study, we used a scalar single value for the whole model.

Parallel tempering

Parallel tempering is a technique used in McMC sampling to improve the exploration of a probability distribution. In McMC sampling, the Markov chain tends to get stuck in local modes of distribution, making it difficult to explore the entire distribution efficiently. To overcome this, one can resort to "simulated annealing". In simulated annealing, the likelihood function is smoothed employing a temperature parameter T (Sambridge, 1999):

$$p(\mathbf{d}|\mathbf{m}) = A\exp\left(-\frac{\phi(\mathbf{m})}{2}\right)\frac{1}{T} = A\exp\left(-\frac{\phi(\mathbf{m})}{2T}\right). \tag{3.23}$$

The temperature T determines the roughness of the distribution that is being explored. Higher temperatures result in flatter distributions, allowing the Markov chain to move more easily between modes. At lower temperatures, chains tend to focus on specific modes. See Figures 3.4c-d for the effect of a low temperature and a high temperature on the McMC sampling.

Parallel tempering subsequently involves running multiple chains, each at a different temperature. The key idea of parallel tempering is to occasionally exchange samples (or temperatures) between chains. These exchanges allow for information to be shared between chains and help chains explore different parts of the distribution. Exchanging samples between chains at different temperatures effectively moves samples from flatter (higher temperature) chains to sharper (lower temperature) chains and vice versa. This helps the chains, collectively, to explore the entire

distribution more efficiently and improves the rate of convergence to the target distribution. This is particularly beneficial when the distribution is multimodal. For details and additional information about the implementation, we refer the readers to Sambridge (2014).

3.3 Application to synthetic data

To test the proposed 2D transdimensional approach, we consider a simple 2D synthetic model with lateral variation (Figure 3.2a). The wavefield is modeled using a two-dimensional finite-difference elastic wave equation solver (SOFI2D; Bohlen et al., 2016) assuming a free surface at the top of the model and vertical (z) point forces. The source time function is a 10 Hz Ricker wavelet. The source is positioned at the model's surface, spanning the range from $x = 10$ to $x = 150$ and $x = 600$ to $x = 740$ with a source interval of 10 meters.

Since the straight fibers record the radial component of the surface waves, we use the horizontal component of the wavefield recorded at the surface of the synthetic model (Figure 3.2b). In this experiment, the recorded surface wave on the horizontal component of the wavefield is the Rayleigh wave. We indicated the fundamental mode surface wave (R0), higher-modes surface waves (R+), and the direct body wave (DW) on the seismic record in Figure 3.2b. The $f-k$ spectrum is shown in Figure 3.2c. The fundamental mode Rayleigh wave is dominant in Figure 3.2b-d.

3.3.1 Multi-offset phase analysis

To obtain a reliable phase-versus-offset spectrum that is associated with the fundamental mode only, we isolate the fundamental mode (Figure 3.2d) by retaining the energy associated with fundamental mode surface-wave velocities (indicated by blue lines in Figure 3.2c) and muting the rest of the spectrum ($f-k$ filtering). The filtered data, after computation of the inverse transform, is presented in Figure 3.2d. For each discrete frequency f_i, the phases of the individual traces of the "cleaned" shot records are unwrapped (e.g., Weemstra et al., 2021), resulting in the $\phi - x$ spectrum. For the ($f-k$ filtered) shot record in Figure 3.2, the (unwrapped) phase is shown as a function of offset for six different frequencies in Figure 3.3a.

The retrieved laterally varying dispersion relation using the MOPA is depicted in Figure 3.3b for the single shot record of Figure 3.2d. Here, we used a spatial window length $W(f_i)$ equal to two wavelengths, where the latter is computed using a reference phase velocity based on the (averaged) phase velocity retrieved through the application of MOPA to the whole shot record. This frequency dependency implies that W decreases with increasing frequency. Linear regression using Equation (3.2) subsequently results in frequency-dependent "local" wavenumbers for each f_i and $x_j^{(c)}$ separately. These wavenumbers are then transformed into phase velocities using Equation (3.3), yielding the set of laterally varying dispersion relations depicted in Figure 3.3b.

To improve the quality of the recovered dispersion curves, MOPA is conventionally applied to multiple shots, each located at a different (in-line) position. In this synthetic experiment, we generate 30 shot records with sources located between

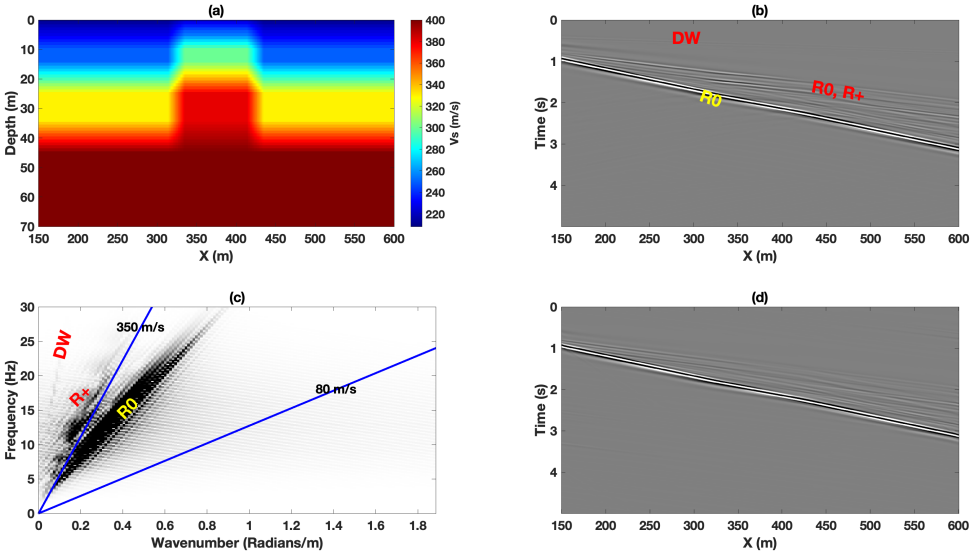

Figure 3.2. *Surface wave spectral analysis of a synthetic active seismic record. (a) The prescribed synthetic model. (b) The horizontal component of the wavefield recorded at the surface for a source located at x = 20 m. (c) $f-k$ spectrum. fundamental mode surface waves (R0), higher-modes surface waves (R+), and direct body waves (DW) are indicated in (b-c). (d) An isolated fundamental mode is retained after an $f-k$ filter has been applied. The blue lines in (c) represent the corner frequencies of the applied (velocity) filter.*

10-150 m and 600-740 m, and with a source spacing of 10 m. Additionally, an $f-k$ filter is applied to each (Fourier-transformed) shot record to facilitate a reliable phase analysis by isolating the fundamental mode. Subsequently, laterally varying dispersion curves are estimated by applying MOPA to each shot record separately. At each position $x_j^{(c)}$, this results in 30 independently estimated dispersion curves. The average of these 30 sections is presented in Figure 3.3c. The associated standard deviation is given in Figure 3.3d, which can be considered as a measure of the uncertainty of the recovered $cp(f_i, x_j^{(c)})$.

Figure 3.3e shows the (true) theoretical location-dependent phase velocities as a reference. These are computed by taking the true 1D shear wave velocity profile at each location and then computing the theoretical dispersion curve using the aforementioned reduced delta matrix method (Buchen & Ben-Hador, 1996; Wu et al., 2019). Figure 3.3f displays the actual phase velocity error computed based on the theoretical dispersion curve (i.e., Figure 3.3e) and the MOPA-derived phase velocities (i.e., Figure 3.3c). Figures 3.3c,e-f show that lower frequencies (less than 3 Hz) are associated with higher uncertainties and deviate from the theoretical dispersion relation. This is due to the low amplitude of the source time function (i.e., a 10 Hz Ricker wavelet) at those frequencies. Additionally, the MOPA algorithm does not cover the regions close to the ends of the line due to the spatial windowing: since this window length W is larger at lower frequencies, lower frequencies are sampled

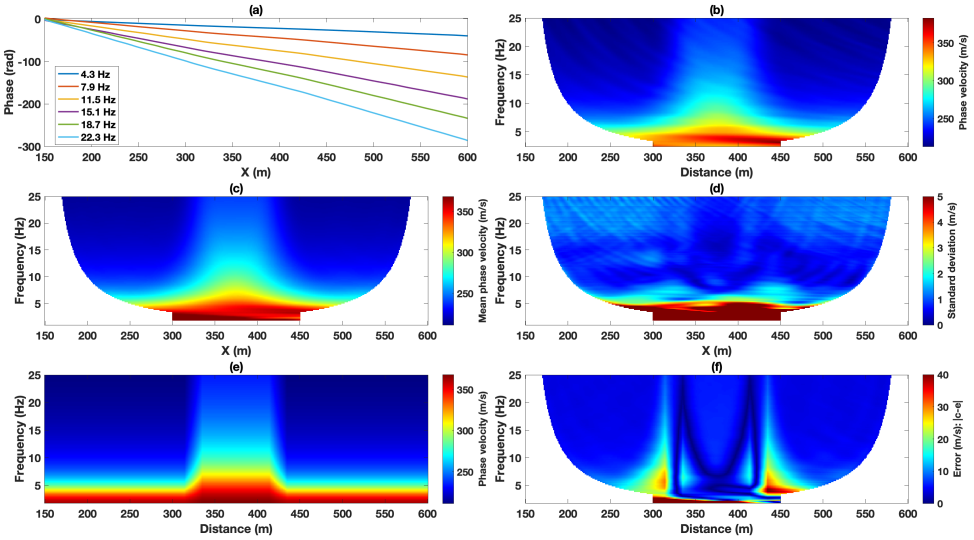

Figure 3.3. *Phase velocity retrieval using MOPA: application to synthetic recordings. (a) Phase-versus-offset for six discrete frequencies of the filtered shot record presented in Figure 3.2d. (b) Phase velocities $cp(f_i, x_j^{(c)})$ retrieved from one single shot record. (c) Mean local phase velocities retrieved from shots with sources at 30 different locations. (d) Standard deviation corresponding to (c). (e) Theoretical (true) laterally varying phase velocities. (f) The phase velocity error is computed based on the MOPA-derived phase velocity (c) and the theoretical phase velocities (e).*

over a shorter spatial interval in Figure 3.3b,c.

3.3.2 Transdimensional 2D inversion

To assess the performance of the proposed algorithm, the theoretical phase velocities (Figure 3.3e) and the recovered phase velocities (Figure 3.3c) are used as input to the proposed 2D transdimensional algorithm. In the next two Sections, we present the results of these tests separately for the two sets of phase velocities.

Inverting theoretical phase velocities

We first add random zero-mean Gaussian noise with a standard deviation of 10 m/s to the theoretical phase velocities Figure 3.3e. The resulting noisy phase velocities (depicted in Figure 3.4a) are then used as the input to the proposed inversion algorithm. We sample the posterior probability distribution with 20 parallel chains, each sampling 500k samples. Ten chains have a temperature of one and the other ten chains have a temperature logarithmically spaced between 2 and 100. The tempering (exchanging temperature values between chains) starts at iteration 75k. The initial samples are generated randomly from the prior range with a velocity increasing monotonically with depth. A sample initial model is depicted in 3.4b. The true velocity profile at $x = 150$ m is extended horizontally and is considered as

the reference model while constraining the misfit function. The model uncertainty (σ_{bh} in Equation 3.22) is assumed to be 100 m/s. The shear wave velocity prior is a uniform prior between 150 and 600 m/s. For the data uncertainty (noise level), we assume an unknown noise hyperparameter (a in Equation 3.19) to be estimated by the proposed Gibbs step during the McMC sampling. By prescribing $\sigma'_{ij} = 1$ (see Equations 3.19, 3.21) and given that $\sigma_{ij} = 10$, a can be expected to approach 10 (asymptotically). The first 200k samples are discarded as the burn-in phase. Then, we retain a sample every 100 iterations. The posterior mean and standard deviation are then computed based on the retained samples with a temperature of one (i.e., $T = 1$). Figures 3.4c-d show two samples at iteration 50k (burn-in phase) in two chains with temperatures of $T = 1$ and $T = 100$, respectively. This clearly shows the effect of the temperature on the sampling.

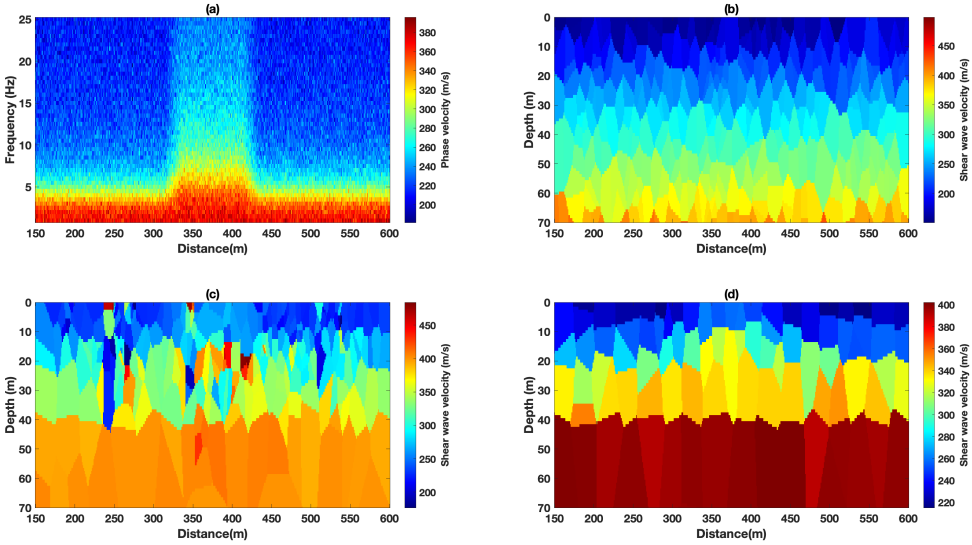

Figure 3.4. *(a) The theoretical phase velocity after the addition of Gaussian noise with the standard deviation set to 10 m/s. (b) An initial sample (i.e., model) is generated randomly with an increasing shear wave velocity by depth. Two samples collected after 50k iterations are depicted in (c) for a "cold" chain with $T = 1$, and (d) for a hot chain with $T = 100$, showing that higher temperatures result in coarser models (and hence also fewer Voronoi cells).*

Figure 3.5 exhibits the results of the transdimensional inversion. Figure 3.5a shows how the number of cells varies as a function of iteration and temperature. The initial temperature of each chain is indicated by the color of each curve. The number of cells stabilizes after a few thousand iterations with the higher temperature chains (red ones) having fewer cells. After the start of parallel tempering (i.e., the exchange of temperature values after iteration 75k), the number of cells associated with the chains initially at lower temperatures reduces and the number of cells associated with the chains initially at higher temperatures increases, both effectively

converging to the same range of number of cells. This demonstrates the convergence of the chains and also highlights the effect of temperature on the exploration of the model space.

Figure 3.5b shows the inferred noise level at different iterations. Not surprisingly, a converges to the standard deviation of the additive random noise (i.e., 10 m/s) for chains without tempering (i.e., $T = 1$). For the tempered chains, the inferred noise level is increasing for higher temperature values. Increasing temperature leads to a more global search of the model space and leads to a higher acceptance rate. This means that models with higher uncertainties are allowed in the collected samples. This explains why the algorithm infers a higher noise level in chains with higher temperatures.

Figure 3.5c shows that the mean of the post-burn-in retained samples associated with a temperature of one nicely correlates with the true shear wave velocity (Figure 3.2a). The layer interfaces and the velocity structure is recovered correctly, even though it is a bit smoother than the true velocity model. The smoothing is mainly due to the additive random noise. Figure 3.5d depicts the posterior standard deviation computed from the retained post-burn-in samples with a temperature of one. As expected, the layer interfaces appear with higher uncertainties. It should be understood that, by using the true local dispersion curves, these results overestimate the performance of the proposed Bayesian approach. That is, in application to field date we do not have the local (1D) phase velocities at our disposal. Instead, we rely on the MOPA-derived dispersion curves, which approximate the true dispersion phase velocity dispersion in the sense that wavefield amplitudes are ignored (Wielandt, 1993). In the next section, we therefore apply our algorithm to dispersion curves estimated through MOPA applied to (finite-difference) modeled wavefields.

Inverting MOPA-derived phase velocities

After the successful recovery of the true shear wave velocity from the theoretical phase velocities, the MOPA-derived local phase velocities are now used in the proposed 2D transdimensional inversion algorithm. Again, we use 20 independent chains to sample the posterior, each sampling 500k models. The initial model of each chain is generated randomly with a randomly selected number of cells and based on a randomly chosen location. We only assume an increasing velocity with depth for the initial model (Figure 3.6a). Again, we discard the first 200k samples as the burn-in period. Then samples are retained at every 100 iterations to avoid collecting correlated samples. The retained samples with a temperature of one are then used for the calculation of the posterior mean (Figure 3.6c) and the posterior standard deviation (Figure 3.6d).

Figure 3.6c shows that the proposed algorithm recovers a smooth version of the true shear wave velocity model in Figure 3.2a. The “smoothing” is predominantly due to the approximation inherent in the MOPA algorithm. The uncertainty presented in Figure 3.6d is also meaningful by having higher values at the layer interfaces.

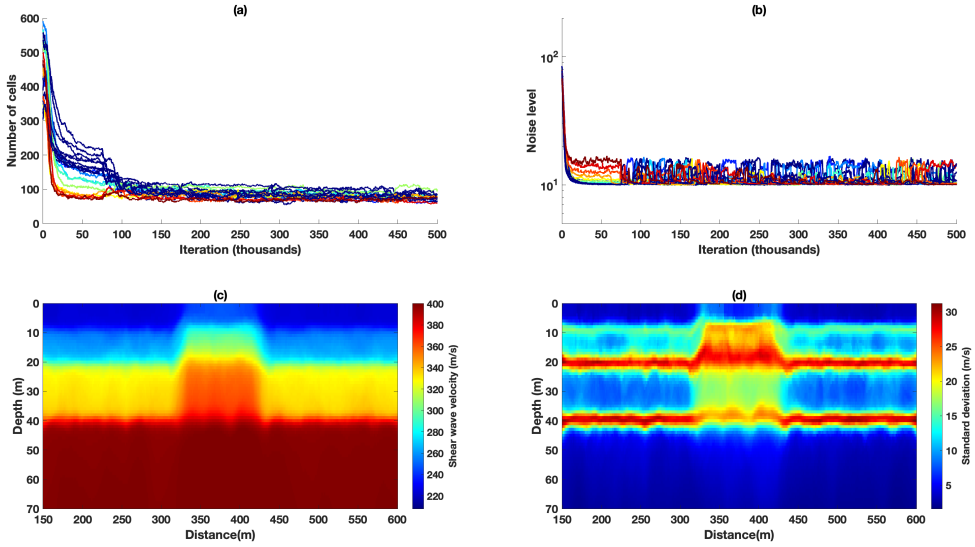

Figure 3.5. *Transdimensional inversion results by using the noisy theoretical phase velocities (Figure 3.4a) as the input data. (a) Number of cell variations by iteration at 20 different chains. The color of each line indicates the initial temperature of the corresponding chain with red for the highest temperature (i.e., $T = 100$) and blue for the coldest chain (i.e., $T = 1$). (b) The variation of inferred noise level (standard deviation) by iteration at 20 different chains. The y-axis is plotted in a log scale for better visibility of variations. The color of each line is similar to (a) indicating the initial temperature of each chain. (c) The posterior mean of the collected samples with a temperature of one from 20 parallel chains. (d) The posterior standard deviation of the retained samples with a temperature of one.*

3.4 Application to DAS data recorded near Zuidbroek, Groningen

In this section, we discuss the application of the proposed Bayesian algorithm to data recorded using a straight fiber DAS system. We first introduce the data. We subsequently recover the local phase velocities, which we then exploit to recover a 2D shear wave velocity model of the subsurface. In the last section, we compare the recovered shear wave velocity sections to shear wave velocity profiles measured along two boreholes positioned on the acquisition line.

3.4.1 DAS data characteristics

The proposed methodology has been applied to DAS data obtained in the province of Groningen in the north of the Netherlands. The top 800 m of the subsurface mainly consists of unconsolidated sediments in this region, with the uppermost layers being of Pleistocene age (down to 25 m, but varying from one place to the other; Kruiver et al., 2017). The data were obtained with fibers as part of a Distributed Acoustic Sensing (DAS) system. Figure 3.7 shows the acquisition setup of the DAS recording system. Different types of fibers were used, namely straight and helically wound fibers (for more details see Al Hasani & Drijkoningen, 2023).

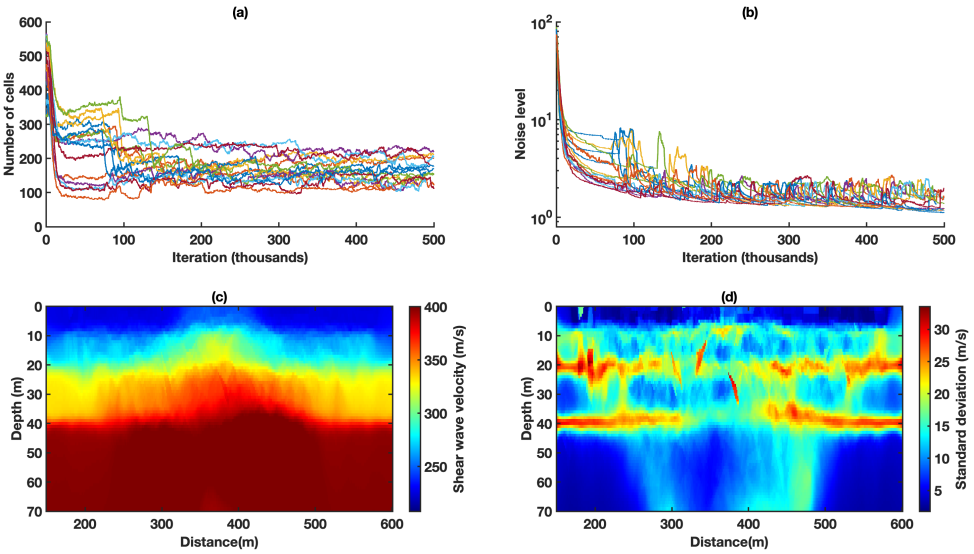

Figure 3.6. *As Figure 3.5, but using the MOPA-derived phase velocities (Figure 3.3c) as input.*

However, we opted for the straight fiber data as it showed the highest sensitivity to the surface waves. The source used is an electrically driven vertical seismic vibrator (Noorlandt et al., 2015) generating two shots per position from $x = 0$ to $x = 750$ every 2 m. The straight fiber was buried at a depth of 2 m with a length of 450 m from $x = 150$ to 600 m. More information on the acquisition can be found in Al Hasani & Drijkoningen (2023). The (receiver) spacing of the recordings is 1 m with a gauge length of 2 m.

All shots positioned on the recording line (i.e., source location between $x = 150$ and 450 m) are split into two off-end shot records to be used in the MOPA algorithm. However, to take into account the near-offset effect (see Park et al., 1999), any trace having an offset smaller than 80 m (i.e., half of the expected maximum wavelength) is discarded. In addition, after removal of the near offsets, any shot record that has a length of less than 50 m is discarded. This is to make sure that there is enough data for the $f-k$ filtering and then the calculation of phase versus offset.

Figure 3.8 shows a sample shot gather of the DAS data. The $f-k$ and $cp-f$ spectra are also provided for a better understanding of the data. The straight fiber records the radial component of the wave field. Since the vertical source is in line with the fiber (i.e., receivers), the recorded surface wave in the radial direction can be interpreted as the Rayleigh wave (assuming low amplitude oblique incident Rayleigh and Love waves, i.e., little surface wave scattering, and low amplitude oblique incident body waves in the f-k domain of interest). Indeed, the shot record appears to be dominated by the fundamental mode Rayleigh wave indicated by **R0**. The fundamental mode is easily detectable in the frequency range of 4-20 Hz in both $f-k$ and $cp-f$ spectra. The higher-modes are also clearly visible in both shot records and their corresponding spectra. We have indicated

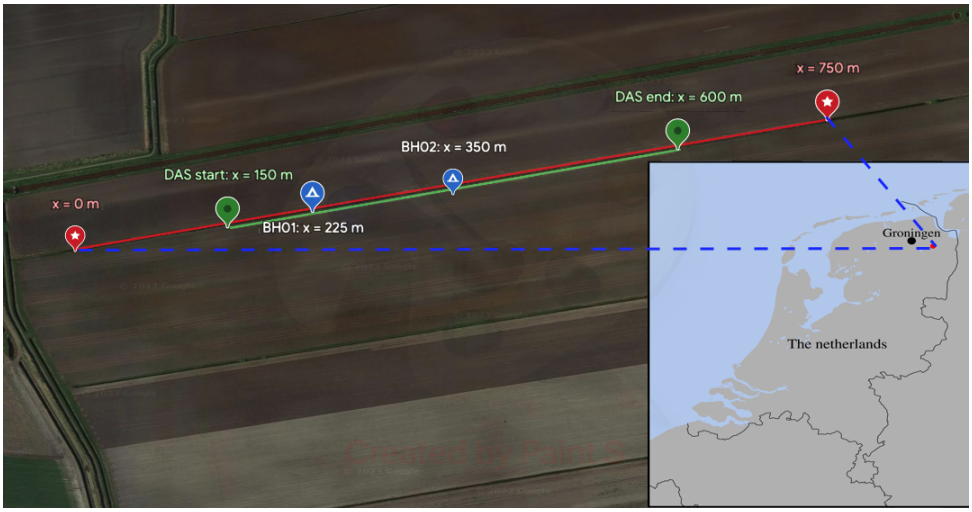

Figure 3.7. *The acquisition setup of the DAS experiment near Zuidbroek, Groningen. The solid red line represents the source line, which has a length of 750 m. The green line represents the DAS straight fiber buried at 2 m depth, and with a length of 450 m. The position of the first source line is defined as $x = 0$ with the end of the source line then being $x = 750$ m. The DAS fiber is buried between $x = 150$ to 600 m. Two boreholes were drilled to a depth of 80 m at $x = 225$ m and $x = 350$ m to measure the shear wave velocity directly.*

higher-modes by **R+** since more than one higher-mode is visible in the $f-k$ and $cp-f$ spectra and because it is difficult to separate them. The colored lines in the $f-k$ spectra represent phase velocities used to design a velocity filter for isolating the fundamental mode. The velocity lines are also depicted on the $cp-f$ spectra for the reader's reference. The red line separating the fundamental mode from higher-modes is velocity dependent. The $f-k$ spectrum between the blue and the red line is preserved and the rest of the spectrum is filtered out ($f-k$ filtering). The filtered record is presented in Figure 3.8d and is dominated by the fundamental mode Rayleigh wave. We have applied this velocity filter to all shot records.

3.4.2 Borehole data

In this study, two open boreholes were drilled down to a depth of 80 m at $x = 225$ m and $x = 350$ m. The (vertical) shear wave velocity and the compressional wave velocity were measured directly using a PS suspension logging tool (Geovista Digital P&S Sonde). In addition to these seismic velocities, the bulk electrical conductivity and the gamma radiation were also measured. The measured logs are presented in Figure 3.9. From 2-10 m below ground level, the subsurface is predominantly sandy. The relatively low electrical conductivity values down to 10 m depth indicate fresh water, and the relatively low gamma ray values in the same depth range suggest low clay content. The main feature observable from the logs is a clear reduction of shear wave velocity between 10 and 20 m together with an increase in gamma-ray

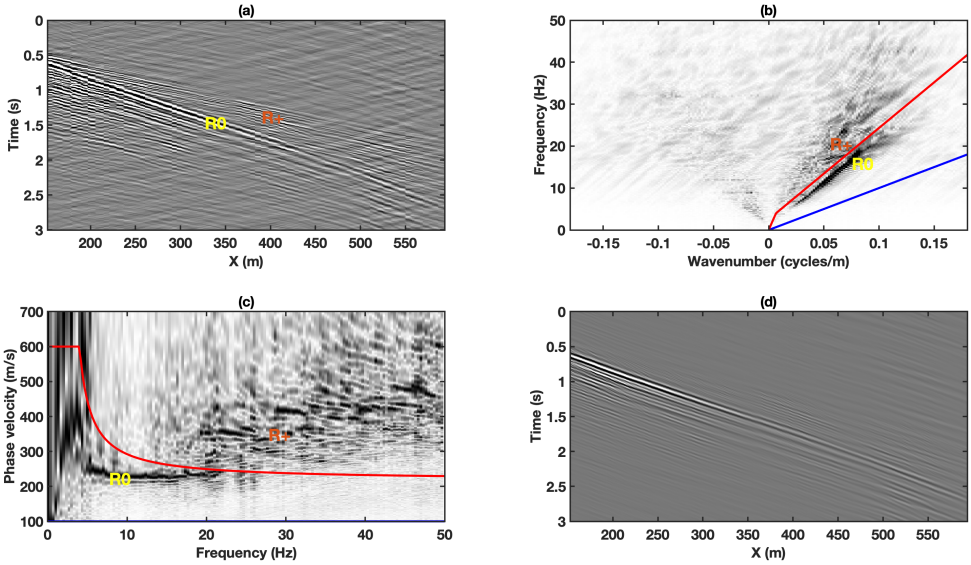

Figure 3.8. *A common shot record (a), its corresponding $f-k$ amplitude spectrum (b), and its corresponding dispersion image (c). The source is located at x = 10 m. The fundamental mode and higher-modes are indicated by R0 and R+, respectively. The blue line represents a phase velocity of 100 m/s and the red line a frequency-dependent phase velocity between 220-600 m/s. Higher-mode surface waves are effectively removed by retaining the $f-k$ spectrum between the blue and red lines ($f-k$ filter). The resulting (time-domain) fundamental mode surface wave shot records are shown in (d).*

and conductivity, especially in Figure 3.9a. The reduction in shear wave velocity is due to the higher clay content, apparent from the conductivity and gamma-ray readings (solid red and black lines, respectively) being higher than above and below that depth range. From 20 m to about 55-60 m a gradual fining-up trend is present in both boreholes, intersected by some more clayey units, for example in Figure 3.9a around 35 m. From 55-60 m a heterogeneous clayey unit can be recognized in both boreholes. Below, until the bottom of the borehole, a second gradual fining-up sequence is present.

The shear wave logs are used to constrain the misfit function as explained in section 3.2.3. To that end, we use moving averages of the shear wave velocity obtained at the two boreholes as 1D reference velocity profiles. We extend these 1D shear wave velocity profiles horizontally to build a 2D reference model for constraining the misfit function. For the uncertainty of this reference model, we opted for a constant value of σ_{bh} = 150 m/s.

To compute the surface wave dispersion curves theoretically, we need the shear wave velocity (v_s), the compressional wave velocity (v_p), and density (ρ). The shear wave velocity, however, is predominantly controlling surface wave phase velocities, and therefore the effect of v_p and ρ are usually ignored (e.g., Wathelet, 2008). Here, we use the velocity logs to get an estimate of the v_p/v_s ratio to be used in the

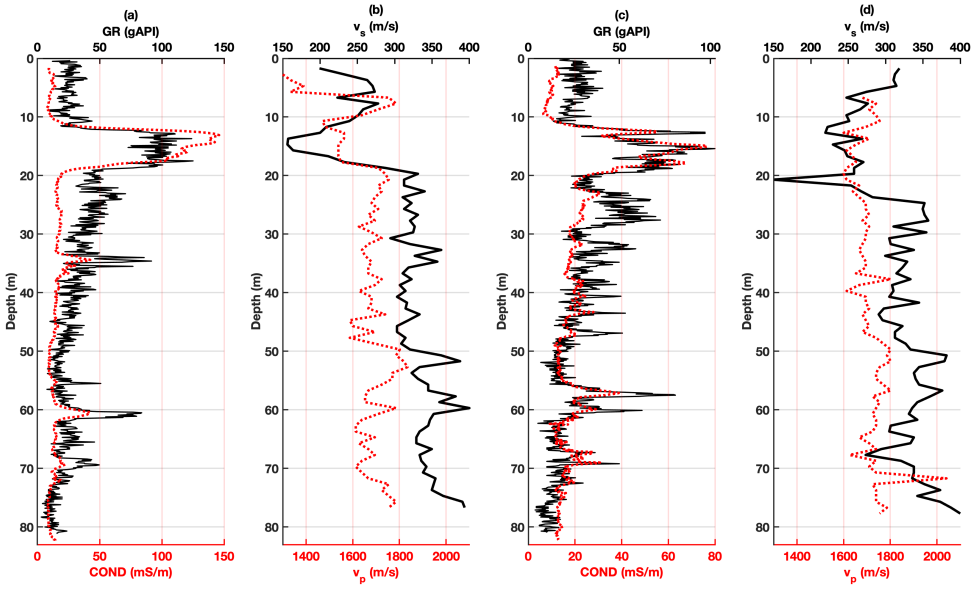

Figure 3.9. *The measured logs of (a-b) first borehole at x = 220 m and (c-d) second borehole at x = 350 m. (a,c) Conductivity (COND; red dashed curve, bottom axis) from Induction-Log readings and Gamma Ray (GR; black curve; top axis). (b,d) Shear wave velocity profile (v_s; black curve; top axis) and compressional wave velocity profile (v_p; red dashed curve, bottom axis).*

theoretical calculation of the dispersion curves. To that end, we compute moving averages of both the shear wave velocity profile and the compressional wave velocity profile. A depth-dependent v_p/v_s ratio is subsequently computed based on these smoothed curves. We then take the average of this curve as the v_p/v_s ratio that dictates the v_p in our Bayesian algorithm. This average v_p/v_s turned out to be close to 5.

3.4.3 Multi-offset phase analysis

After isolating the fundamental mode (Figure 3.8d), we apply the MOPA algorithm to all shot records extracted from the DAS data. Figure 3.10 shows the results of the MOPA method applied to the field DAS data to retrieve the dispersion curves. The unwrapped phase versus offset is depicted for 7 frequency components of a single shot record (Figure 3.8b) in Figure 3.10a. The retrieved laterally varying dispersion curves are presented in Figure 3.10b. The shot record is somewhat noisy, which manifests itself in relatively rapidly varying gradients of the phase-versus-offset curves. A smoother and more reliable dispersion curve is derived by repeating the process for multiple shot records. Figure 3.10c presents the average laterally varying dispersion curves derived from all shot records. The uncertainty (quantified by means of a standard deviation) is depicted in Figure 3.10d.

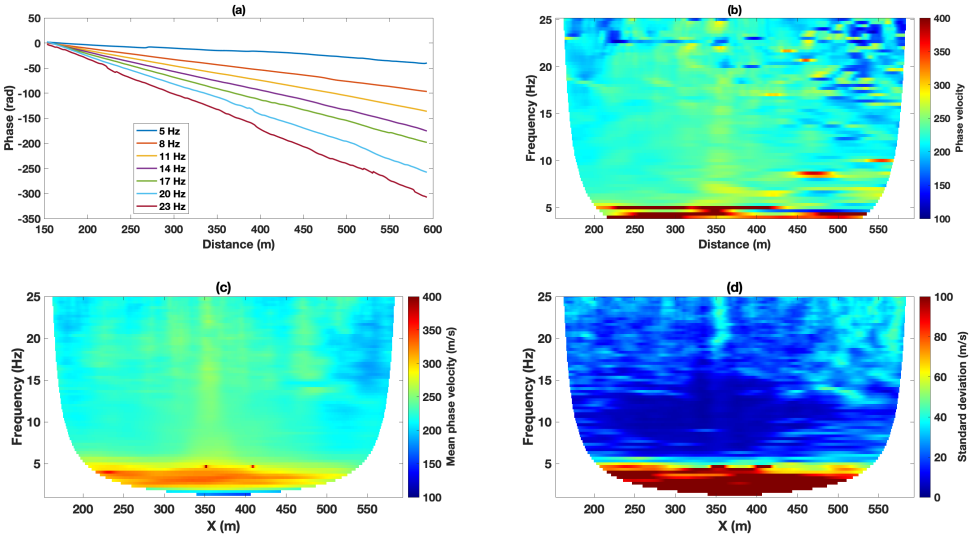

Figure 3.10. *MOPA applied to the DAS-derived shot records to estimate lateral shear wave velocity variations in the subsurface. (a) Unwrapped phase-versus-offset at seven different frequencies (different colors) for the filtered seismic record depicted in Figure 3.8d. (b) laterally varying phase velocity retrieved from the single shot record of Figure 3.8d. (c) Mean of the laterally varying dispersion curves retrieved from all shots. (d) Standard deviation corresponding to (c).*

3.4.4 Transdimensional 2D inversion

The retrieved laterally varying phase velocities (Figure 3.10c) serve as input to the 2D transdimensional algorithm. We run 20 independent McMC chains in parallel, each sampling 750k models. 10 chains had a temperature of one and 10 chains had their temperatures logarithmically spaced between 2-100. Tempering starts at iteration 75k. The initial model at each chain is selected randomly, but with velocity increasing monotonically with depth. Figure 3.11 shows the variation of the dimension of the model space (a) and also the progression of the inferred noise level (b). Similar to the synthetic data, chains with a higher initial temperature converge to a lower number of cells. By interchanging temperatures between chains, the number of cells converges to a lower range in (initially) cold chains, effectively preventing them from being "stuck in local modes. For the inference of the noise level, we used the MOPA-derived phase velocity uncertainties (Figure 3.10d) as σ'_{ij} in Equation 3.19. We subsequently infer a using the proposed Gibbs step. The first 250k samples of each chain are discarded as the burn-in phase. To avoid correlated samples, every 100th sample is retained. We then use the retained samples associated with chains with a temperature of one to approximate the posterior distribution. From the posterior distribution, we compute the pointwise averaged phase velocities and pointwise standard deviations, which we refer to as the posterior mean and standard deviation.

Figure 3.12 presents the recovered shear wave velocity section and its corresponding uncertainty using the proposed 2D transdimensional method. A clear "layer-cake structure" can be observed (Figure 3.12a). The shear wave velocity profiles from the well logs are also compared with the posterior mean (Figure 3.12c and d): compared to the shear wave velocity logs, the inverted shear wave velocity is relatively smooth. A clear interface is located at a depth of approximately 20 m, and results in a high uncertainty at that depth (Figure 3.12b). This is in agreement with the well log data presented in Figure 3.9. However, the algorithm fails to recover the velocity variation within the top 20 meters. This is due to the high uncertainty of the MOPA-derived phase velocities and also the high inferred noise hyper-parameter a. In particular, we attribute this to phase velocities at higher frequencies not being recovered very well due to the interference of higher modes. Moreover, the MOPA algorithm uses a spatial window while retrieving distance dependent phase velocities, which leads to a smooth phase velocity map, see for example Figure 3.3c. In addition, the MOPA-derived phase velocities (Figure 3.10c) at the sides of the model have fewer frequency components and are therefore associated with higher uncertainties. Finally, we note that at the lower end of the frequency spectrum, the MOPA-derived phase velocities exhibit relatively large uncertainties due to the limited excitation of lower frequencies by the vibroseis (see Figure 3.10d).

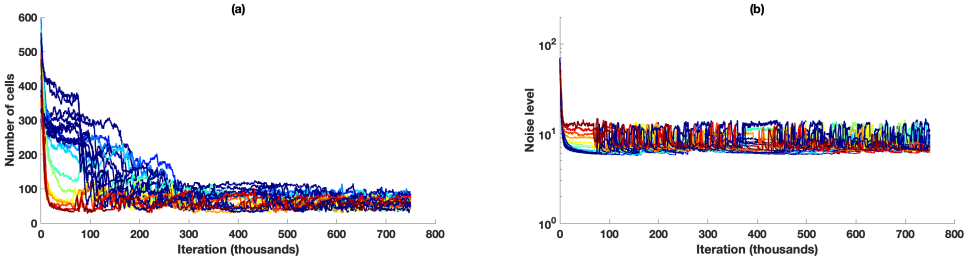

Figure 3.11. *Chain statistics of the 2D transdimensional algorithm with (field-data-derived) phase velocities serving as input data (see Figure 3.10c). (a) Number of cells as a function of sample number for all 20 chains. The color of each solid line indicates the initial temperature of the corresponding chain with red corresponding to the highest temperature (i.e., $T = 100$) and blue to the coldest chain (i.e., $T = 1$). (b) The variation of inferred noise level (standard deviation) as a function of sample number for all chains. The vertical axis is plotted using a log scale to visualize the variations more clearly. Similar to (a), the color of each line corresponds to the initial temperature of that chain.*

3.5 Discussion

A number of points need to be discussed. First, the transdimensional derived shear wave velocity profiles at the location of the two boreholes are a very smooth version of the shear wave velocity logs. At the location of the first borehole, few

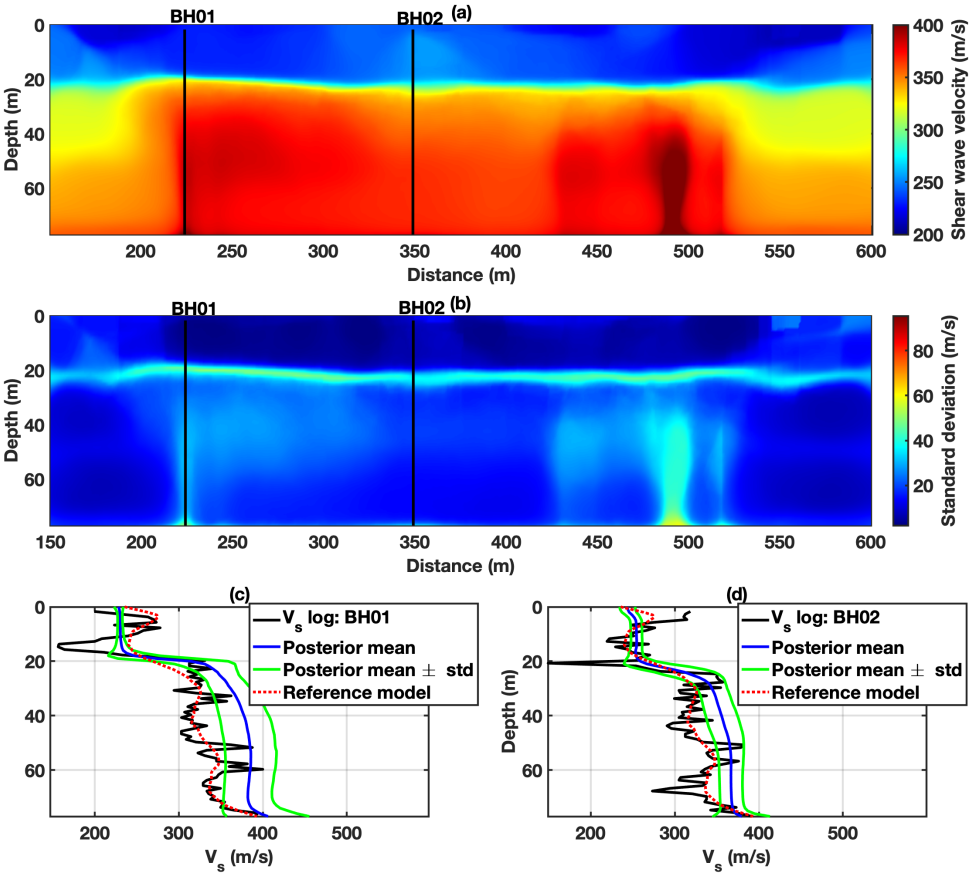

Figure 3.12. *Result of the application of the 2D transdimensional algorithm to the DAS-derived phase velocities. (a) Recovered 2D shear wave velocity section (i.e., posterior mean), (b) recovered model uncertainty (i.e., posterior standard deviation; std), and comparison with the shear wave velocity profile along the first (c) and second (d) borehole.*

(local) phase velocities have been estimated; none in fact at lower frequencies (see Figure 3.10). This leads to higher uncertainties and may well explain the fact the pointwise mean shear wave velocity deviates from the more reliable and locally measured shear wave velocity log along the first borehole. The limited sampling toward the end of the line is inherent to the MOPA algorithm we use in this study. The quality of the dispersion curves at these locations might be improved by the tomography-derived phase velocity retrieval algorithm (Barone et al., 2021). Additionally, the MOPA-derived phase velocity estimates are affected by higher modes, especially at higher frequencies. The windowing also laterally smooths the retrieved phase velocities, prohibiting the recovery of a lateral high-resolution shear wave velocity structure. This might be improved by using the common midpoint cross-correlation algorithm (CMPCC; Hayashi & Suzuki, 2004) for the recovery of

the distance-dependent phase velocities, but is beyond the scope of this study.

Second, data uncertainty (σ in Equation 3.6) plays a crucial role in the convergence of our Bayesian algorithm (Bodin et al., 2012). As we explained above, the MOPA algorithm provides us with an estimate of the data uncertainty (Figure 3.3f). In this study, we used this MOPA-derived uncertainty in combination with a hyper-parameter during the McMC sampling of the posterior. We assumed one hyperparameter for all frequencies. In case the true uncertainty varies with frequency, a (smooth) frequency-dependent hyper-parameter may improve the inversion result by allowing the uncertainty to vary with frequency.

Third, in terms of computation time, the proposed 2D transdimensional algorithm is comparable to independent 1D inversion of the dispersion curves. This is because in the proposed 2D transdimensional algorithm, at each step of the McMC, we perturb a small portion of the model space. Then, we compute the forward function (i.e., the primary source of the computational demand) only at the updated part of the model space. This reduces the computational time significantly. The added values of the proposed 2D transdimensional scheme are the enhanced lateral correlation and the reduced solution non-uniqueness.

3.6 Conclusion

We investigated the potential of (straight fiber) DAS-derived Rayleigh waves, in combination with a 2D transdimensional inversion algorithm, to recover a 2D shear wave velocity section down to a depth of approximately 60 meters. To that end, We first recover the laterally varying phase velocities using multi-offset phase analysis. Then, we adopt the 2D transdimensional algorithm to invert all available laterally varying dispersion curves simultaneously. Inherent to our approach, we find the recovered shear wave velocity to vary smoothly as a function of lateral position along the acquisition line. The (posterior) mean shear wave velocity section shows a clear layer interface at around 20 meters (abrupt change in shear wave velocity), whose presence is supported by a high uncertainty at that depth. This is consistent with (borehole) log-derived rapidly increasing shear wave velocities at the same depth.

4

One-step 3D transdimensional surface wave tomography: synthetic data

Abstract: Seismic travel time tomography using surface waves is an effective tool for three-dimensional crustal imaging. Historically, these surface waves are the result of active seismic sources or earthquakes. More recently, however, surface waves retrieved through the application of seismic interferometry have also been exploited. Conventionally, two-step inversion algorithms are employed to solve the tomographic inverse problem. That is, a first inversion results in frequency-dependent, two-dimensional maps of phase velocity, which then serve as input for a series of independent, one-dimensional frequency-to-depth inversions. As such, a set of localized depth-dependent velocity profiles are obtained at the surface points. Stitching these separate profiles together subsequently yields a three-dimensional velocity model. Relatively recently, a one-step three-dimensional non-linear tomographic algorithm has been proposed. The algorithm is rooted in a Bayesian framework using Markov chains with reversible jumps, and is referred to as transdimensional tomography. Specifically, the three-dimensional velocity field is parameterized by means of a polyhedral Voronoi tessellation. In this study, we investigate the potential of this algorithm for the purpose of recovering the three-dimensional surface-wave-velocity structure from ambient noise recorded on and around the Reykjanes Peninsula, southwest Iceland. To that end, we design a number of synthetic tests that take into account the station configuration of the Reykjanes seismic network. We find that the algorithm is able to recover the 3D velocity structure at various scales in areas where station density is high. In addition, we find that the standard deviation of the recovered velocities is low in those

This chapter is published as:
Rahimi Dalkhani, A., Zhang, X., & Weemstra, C. (2021). On the potential of 3D transdimensional surface wave tomography for geothermal prospecting of the Reykjanes Peninsula. Remote Sensing, 13(23), 4929, https://doi.org/10.3390/rs13234929.
Minor modifications have been applied to keep consistency within this thesis.

regions. At the same time, the velocity structure is less well recovered in parts of the peninsula sampled by fewer stations. This implies that the algorithm successfully adapts model resolution to the density of rays. It also adapts model resolution to the amount of noise in the travel times. Because the algorithm is computationally demanding, we modify the algorithm such that computational costs are reduced while sufficiently preserving non-linearity. We conclude that the algorithm can now be applied adequately to travel times extracted from station–station cross correlations by the Reykjanes seismic network.

4.1 Introduction

The Reykjanes high temperature geothermal system is located at the tip of the Reykjanes peninsula, southwest Iceland. The Reykjanes peninsula can be considered a landward extension of the Reykjanes Ridge, making it an active volcanic zone. The heat from the Reykjanes geothermal system is currently harvested by two 50 MWe steam turbines, which draw from numerous wells. Most of these wells produce from depths of 2 to 2.5 km, where temperatures are estimated to be around 280° (Friðleifsson et al., 2011). Relatively recently, the 4.5 km deep exploratory IDDP-2 well was drilled to examine the economic potential of the production of super critical fluids (Friðleifsson et al., 2020).

Although the subsurface below the Reykjanes peninsula has been the subject of various geophysical surveys (e.g., Martins et al., 2020; Darnet et al., 2020), resolution remains an issue. In addition, the uncertainty of the recovered (best) models is often not estimated. In this study, we therefore investigate the potential of three-dimensional probabilistic surface wave inversion for the purpose of imaging the Reykjanes peninsula in general, and the Reykjanes geothermal system in particular. It should be understood that this is a feasibility study: we limit ourselves to probabilistic inversions of synthetic travel times. In chapter 5 we will draw from the experience obtained in this chapter. Chapter 5 will hence involve probabilistic inversion of travel times extracted from field-data-derived surface wave responses.

Surface wave responses can be retrieved from recordings of ambient seismic noise (e.g., Weemstra et al., 2013). This process is often referred to as seismic interferometry, and hence the retrieved responses are usually referred to as 'interferometric responses' (Wapenaar & Fokkema, 2006). Specifically, seismic interferometry dictates that, by averaging cross correlations of ambient seismic noise over a sufficient amount of time, receivers can be turned into so-called virtual sources. This is a pairwise process: the Earth's response to one of the two receivers (the virtual source) is recorded by the other receiver. By applying this procedure, pairwise, to all stations constituting an array of seismic surface stations, surface wave responses between all seismic stations will be retrieved. In practice, not all station couples yield interferometric surface wave responses of sufficient quality (for details regarding interferometric surface wave retrieval from recordings of ambient seismic noise see, for example, Kästle et al., 2016).

Interferometric techniques may well play an important role in the future of geothermal exploration (e.g., Sánchez-Pastor et al., 2019). In particular, this applies to tomographic travel time inversions: contrary to travel time tomography exploiting

earthquake signals, the spatial sampling by the interferometric ray paths does not suffer from either a limited number of earthquakes or an irregular distribution of these earthquakes (Martins et al., 2020). In addition, Rayleigh (and Love) waves have a depth-dependent sensitivity to subsurface velocity. This sensitivity varies as a function of frequency, with lower frequencies being more sensitive to the deeper subsurface and higher frequencies more sensitive to the shallower structure (Zhou et al., 2004; Herrmann, 2013). It is this frequency-dependent depth dependence that enables the three-dimensional approach proposed in this study.

The interferometric travel times between the different stations of a seismic array can serve as input to a tomographic inverse problem (e.g., Bodin & Sambridge, 2009; Korostelev et al., 2015). Surface wave tomography is a well-known and popular method to obtain the Earth's seismic velocity distribution. Many of the existing tomographic algorithms and inversion methods rely on first-arrival travel times (Rawlinson et al., 2003; Nolet, 2008; Rawlinson et al., 2010). Martins et al. (2020) use a two-step linearized tomographic inversion method to recover the 3D surface wave velocity of the Reykjanes Peninsula. The first step involves recovering frequency-dependent 2D maps of phase velocities using a linearized tomographic inversion method assuming straight rays. In the second step, they run separate frequency-to-depth inversions (Zhou et al., 2004; Herrmann, 2013).

Conventional linearized or gradient-based iterative tomographic inversion schemes (e.g., Bensen et al., 2009; Martins et al., 2019, 2020) usually do not include a detailed assessment of the uncertainty (Young et al., 2013). In addition, such schemes require an (a-priori) prescribed cell size, which does not account for spatial variations in sampling (i.e., a non-uniform ray coverage). Moreover, these methods require a proper regularization to account for the ill-conditioned nature of the inverse problem (Tikhonov, 1963; Martins et al., 2019). The transdimensional hierarchical Bayesian method introduced by Bodin et al. (2012) overcomes these two limitations. The transdimensional method is a Bayesian inference method that relies on reversible jump Markov chains (rjMcMC; Green & Hastie, 2009), in combination with a Voronoi partitioning. The number of Voronoi cells is allowed to vary between steps of the Markov chain, and is in fact one of the parameters that is estimated. It is this specific feature of the algorithm that causes the solution to be "transdimensional". The ensemble of velocity models visited by the transdimensional Markov chain asymptotically approaches the posterior probability density function (henceforth simply 'posterior'). The method is purely data-driven and requires minimal assumptions regarding the model. Compared to the aforementioned linearized and iterative inversion schemes (which keep the spatial model parameterization fixed), the method is particularly flexible: it dynamically adapts to a non-uniform data coverage without requiring the use of any arbitrary regularization (e.g., damping or smoothing).

The transdimensional method was used successfully by Bodin & Sambridge (2009) to obtain 2D Rayleigh-wave velocity maps of Australia. Galetti et al. (2015) further generalized the method by making it fully non-linear; that is, ray paths are updated at each step of the Markov chain in their case. The method has recently been applied successfully to the British Isles (Galetti et al., 2017). Similar to the

aforementioned study by Martins et al. (2020), Young et al. (2013) and Galetti et al. (2017) use a two-step scheme to recover the 3D surface wave velocity structure. In the latter studies, however, the frequency-dependent 2D maps of phase velocity are obtained using a 2D transdimensional approach. Additionally, the obtained (laterally varying) dispersion curves are inverted using a 1D transdimensional approach. Still, however, the two-step procedure results in a collection of spatially varying 1D velocity models. These velocity models are subsequently interpolated to build a 3D velocity structure of the subsurface.

More recently, Zhang et al. (2018) showed that the two-step transdimensional inversion scheme is not optimal in the sense that information is lost. Consequently, they proposed a one-step 3D transdimensional approach that uses a 3D discretization of the subsurface using a Voronoi polyhedral parameterization. The approach has a computational cost comparable to the two-step transdimensional approach, but preserves valuable information and results in a more accurate velocity structure and a better interpretive uncertainty estimation (Zhang et al., 2018).

In this study, we investigate the potential of the one-step 3D probabilistic inversion method (Zhang et al., 2018, 2020) to recover the 3D velocity structure beneath the Reykjanes peninsula, southwest Iceland. Specifically, we focus on the ability to use interferometric surface wave responses retrieved from ambient noise recorded by an array of stations on and around this Peninsula (the array is hereafter referred to as the RARR; Weemstra et al., 2021). The RARR was a dense seismic deployment consisting of 83 continuously recording stations (Figure 4.1). As can be seen in Figure 4.1, the station distribution of the RARR is non-uniform, that is, the station coverage is dense in one area while it is sparse in other areas. A non-uniform distribution of stations implies that the achievable velocity resolution can be expected to vary significantly across the region covered by the seismic array, that is, higher in the regions that are more densely covered by stations and lower where station density is low. The transdimensional method uses a model parameterization using Voronoi cells in conjunction with a reversible-jump Markov chain Monte Carlo algorithm to account for the variable station coverage. As such, the method dynamically adapts itself to both data density and underlying velocity structure (Bodin & Sambridge, 2009).

Surface wave dispersion curves (i.e., phase velocities or frequency-dependent travel times) have been extracted from surface wave responses retrieved using seismic interferometry by cross-correlation (e.g., Weemstra et al., 2016, 2021). Although our final objective is to apply the 3D probabilistic inversion scheme to these dispersion curves, this study is limited to the synthetic dispersion curves. That is, we specifically aim to understand and showcase the potential of the proposed inversion scheme for the RARR's station configuration in combination with the frequencies for which surface wave responses could be retrieved (0.1–0.5 Hz). The dispersion curves extracted from the field data will be inverted in chapter 5, and we will benefit from the findings presented in this chapter.

As shown in Figure 4.1, the station's elevation varies between approximately −0.2 km and 0.2 km. Based on a previous study by Martins et al. (2020), we can assume a minimum velocity of 2 km/s. For the range of frequencies considered (0.1–0.5

Hz), the minimum wavelength would then be 4 km. This implies that the minimum wavelength is more than ten times larger than the elevation variation. We therefore ignore the station's elevation in the rest of this study.

To investigate the potential of this one-step 3D transdimensional method, we generate synthetic frequency-dependent travel times between the station locations of the RARR. Specifically, we prescribe various 3D block model velocity distributions. The frequency-dependent travel times, derived from phase velocity data, are then used as input for the one-step 3D transdimensional algorithm. We find that the algorithm recovers the velocity structure reasonably well for the RARR configuration within the desired frequency range. However, the method is computationally demanding. Therefore, we modify the algorithm by updating ray paths occasionally, instead of doing this at each step of the Markov chain. A simple test is designed to decide on the update level efficiently. The effect of (the computational) grid size on forward modeling errors and how to choose an appropriate size are also discussed.

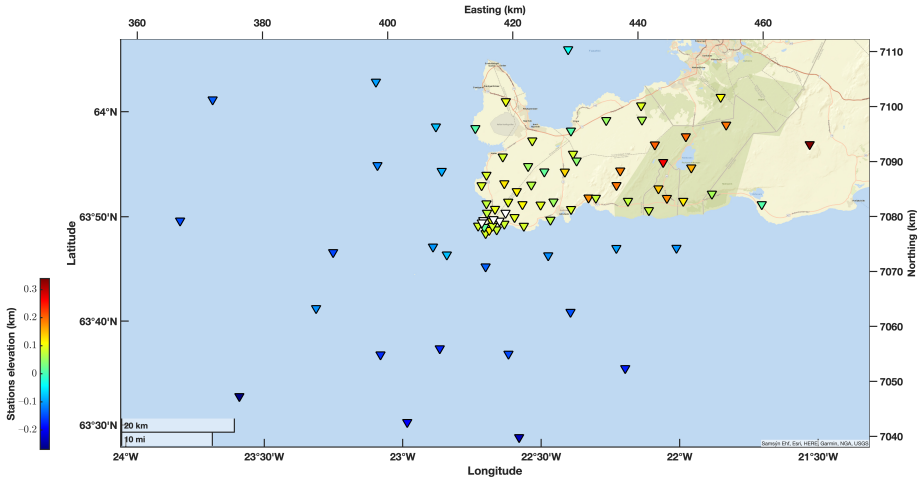

Figure 4.1. *Geographical locations of 83 seismic stations of the RARR. The left and bottom axes indicate spherical coordinates, whereas the right and the top axes display UTM coordinates. Stations locations are depicted as colored triangles. Colors indicate the elevation of the corresponding station. Elevation information was lacking for five stations that are depicted with white triangles.*

4.2 Transdimensional surface wave tomography

Transdimensional tomography is a Bayesian inference method that uses Voronoi cells in conjunction with a rjMcMC algorithm to allow a variable parameterization of the model space. The objective of Bayesian inversion is to recover the posterior probability density of the model parameters given the observed data, $p(\mathbf{m}|\mathbf{d})$. Based on Bayes' rule (Bayes, 1958):

$$p(\mathbf{m}|\mathbf{d}) = \frac{p(\mathbf{d}|\mathbf{m})\,p(\mathbf{m})}{p(\mathbf{d})}, \tag{4.1}$$

where the vector $\mathbf{d}$ contains the frequency-dependent travel times. The vector $\mathbf{m}$ contains the model parameters and depends on the parameterization of the region of interest; we discuss this vector in more detail later. The likelihood function $p(\mathbf{d}|\mathbf{m})$ plays a fundamental role in the inference of the model space as it provides the probability of the observed travel times given a specific velocity model. The prior probability distribution, $p(\mathbf{m})$, depends on the (a priori) known information about the model space. Finally, $p(\mathbf{d})$ is the so-called evidence, which here can be considered a constant because it is not a function of any particular model $\mathbf{m}$. Consequently, we have:

$$p(\mathbf{m}|\mathbf{d}) \propto p(\mathbf{d}|\mathbf{m})\,p(\mathbf{m}). \tag{4.2}$$

4.2.1 Model parameterization

In conventional linearized or gradient-based seismic tomography methods, the region of interest is usually parameterized using fixed cells or a grid of points with predefined shapes and sizes (usually regular rectangular grids). Determining the shape and size of the grid is always a challenge and, ideally, is a function of the data uncertainty (i.e., level of noise available in data) and data resolution (i.e., the ability of the data to resolve different scales or features in the model). Data uncertainty is usually not known and should therefore be estimated before the inversion. In addition to unknown data uncertainty, differences in data resolution due to nonuniform spatial sampling render a uniform grid size undesirable. Consequently, irregular grids or meshes have been proposed by some authors (Sambridge et al., 2005; Bodin & Sambridge, 2009; Bodin et al., 2009; Belhadj et al., 2018; Hawkins et al., 2019).

Because of the challenge in defining cell geometries, Bodin et al. (2009) and Bodin & Sambridge (2009) proposed to invert for cell geometries and seismic properties (e.g., velocities) simultaneously. This means that the data directly determine the parameterization. To allow the size and shape of cells to be variable and unknown in the tomographic algorithm, different kinds of methods have been proposed, including Voronoi cells in 2D (Bodin et al., 2009; Bodin & Sambridge, 2009; Bodin et al., 2012; Galetti et al., 2017), Voronoi polyhedra (or simply also cells) in 3D (Zhang et al., 2018, 2020), Delaunay triangulation in 2D (Ryberg & Haberland, 2017; Hawkins et al., 2019), Johnson–Mehl tessellation in 2D (Belhadj et al., 2018), and Gaussian kernels for a 2D model (Belhadj et al., 2018). Despite the abilities of Voronoi cells to accommodate sharp changes and discontinuities, some authors questioned their ability in the case of smooth velocity models or models with a gradient in velocity changes (e.g., Zhang et al., 2020; Hawkins et al., 2019; Ryberg & Haberland, 2017).

In this study, we parameterize the 3D velocity field using polyhedral Voronoi cells to recover the 3D shear wave velocity structure of the subsurface (Zhang et al., 2020). By assigning a constant shear wave velocity (v_s) to each Voronoi cell, the Voronoi

tessellation turns into a shear wave velocity model. Figure 4.2 shows the region of interest with a coarse parameterization using 33 cells and a finer one with 704 cells; both generated randomly. The number of Voronoi cells, their position, and the shear wave velocity in each cell are treated as unknowns in the tomographic inversion. Importantly, compressional wave velocity (v_p) is considered to be a linear function of v_s, using the relation $v_p = 1.73 v_s$ (Zhang et al., 2018). Density (ρ) is considered to be a function of compressional wave velocity as $\rho = 2.35 + 0.036(v_p - 3)^2$, where v_p and v_s are in km/s and ρ is in g/cm^3 (Zhang et al., 2018; Kurita, 1973). It is useful to note that the parameterization and relations in this section imply that the medium is assumed to be isotropic.

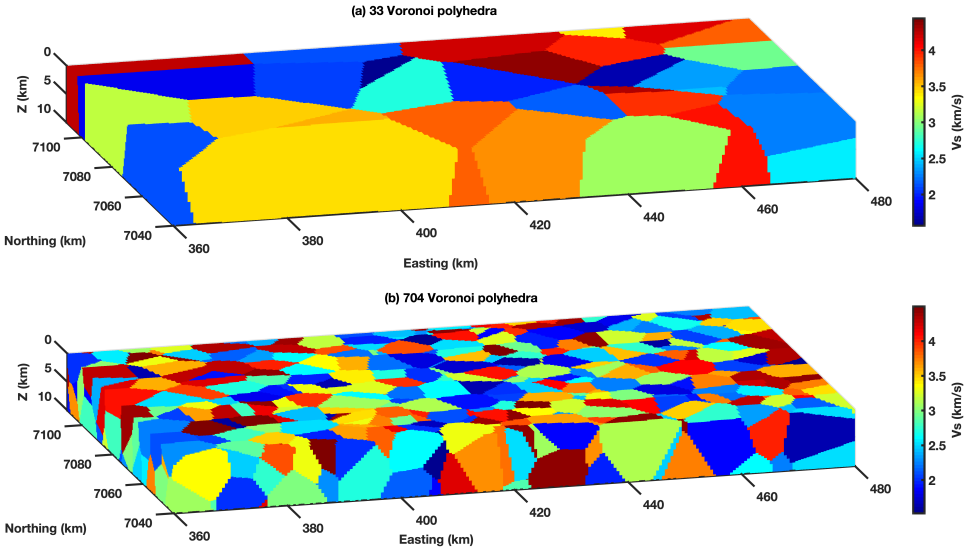

Figure 4.2. *Two random Voronoi parameterizations. The first uses 33 Voronoi cells (**a**), and the second uses 704 Voronoi cells (**b**). Both cell locations and the assigned velocities are generated randomly.*

4.2.2 The likelihood

The dependence of the posterior on the input data is encoded in the likelihood function $p(\mathbf{d}|\mathbf{m})$. The likelihood function can be considered as a measure of misfit between observed and predicted data. The normalized Gaussian likelihood function reads:

$$p(\mathbf{d}|\mathbf{m}) = \left(\prod_{l=1}^{n_f} \prod_{k=1}^{n_r} \frac{1}{\sqrt{2\pi}\sigma_{kl}} \right) \exp\left(- \sum_{j=1}^{n_f} \sum_{i=1}^{n_r} \frac{\left(g_{ij}(\mathbf{m}) - d_{ij}\right)^2}{2\sigma_{ij}^2} \right), \tag{4.3}$$

where n_f and n_r are the number of discrete frequencies and ray paths, respectively. d_{ij} is the travel time along ray path i at discrete frequency j. The vector $\mathbf{m}$ contains

the parameters describing the proposed subsurface model. g_{ij} is the computed travel time along ray path i at discrete frequency j in that subsurface model. σ_{ij} is the data uncertainty or noise level for the travel time associated with discrete frequency j and ray path i (and hence σ_{kl} is associated with discrete frequency l and ray path k) . This data uncertainty includes both observational errors and modeling errors (Bodin et al., 2012). The data uncertainty controls the level of fit and directly affects the complexity of the models in the posterior distribution. That is, the number of Voronoi cells needed to explain the data is highly dependent on the estimated data noise (Bodin et al., 2012). Consequently, σ_{ij} plays an important role in the transdimensional algorithm. Here, we consider it to be a linear, frequency-dependent function:

$$\sigma_{ij} = a_j t_{ij} + b_j, \tag{4.4}$$

where t_{ij} is the computed travel time along ray path i at discrete frequency j. a_j and b_j are noise hyper-parameters for the discrete frequency j. It is worth noting that this linear relation for the noise parameters is a common assumption and is demonstrated in several previous studies (e.g., Bodin et al., 2012; Galetti et al., 2017; Zhang et al., 2020). Moreover, it is straightforward to implement it in the context of the transdimensional algorithm.

4.2.3 Forward modeling

To evaluate the likelihood of a proposed model given the observed data and to compare this likelihood with the likelihood of the current model in the chain, we need to compute the frequency-dependent travel times in the proposed model ($g_{ij}(\mathbf{m})$ in Equation 4.3). This is achieved by employing a two-step approach detailed in Zhang et al. (2018). First, at each point on the Earth's surface, the local frequency-dependent dispersion curves are computed using a modal approximation method (Herrmann, 2013) in the 1D vertical depth profile of surface wave velocity beneath each of the surface points. As such, we obtain frequency-dependent 2D maps of surface wave phase velocity. Figure 4.3 depicts this first step. Figure 4.3a depicts a randomly generated 3D surface wave velocity model using Voronoi polyhedra. Figure 4.3b depicts the corresponding surface wave phase velocity as a function of frequency (vertical axis). We refer to this first step as the depth to frequency step.

In the second step, we use the frequency-dependent phase velocities to compute frequency-dependent travel times by solving the Eikonal equation in two dimensions:

$$|\nabla T(\mathbf{x},\omega)| = \frac{1}{c(\mathbf{x},\omega)}, \tag{4.5}$$

where $T(\mathbf{x},\omega)$ is the frequency-dependent travel time of the wave-front at surface location $\mathbf{x}$ and angular frequency ω, and $c(\mathbf{x},\omega)$ is the phase velocity of the model at that surface location and frequency. By solving this equation for each source at each frequency, the travel time field corresponding to first arrivals is obtained at all points of the (2D) model, including the receiver locations. A variety of methods has been proposed for the solution of this equation, including finite-difference (Vidale, 1990;

Qin et al., 1992) and the fast marching method (FMM) (Sethian, 1996; Rawlinson & Sambridge, 2004). The fast-marching method is unconditionally stable, meaning that we can use relatively coarse grids to solve Equation 4.5. A coarser grid, however, does introduce additional travel time errors, which we refer to as modeling errors.

We use the FMM to solve Equation 4.5 to obtain frequency-dependent travel times at the location of each receiver. As one can see, the relation between the model parameters, $c(\mathbf{x},\omega)$, and travel time, $T(\mathbf{x},\omega)$, in Equation 4.5 is nonlinear, implying the solution of the forward function involves relatively high computational costs (compared to other computational steps in the rjMcMC algorithm). In order to reduce overall computational costs, it is common practice to linearize the problem using a fixed ray path geometry (e.g., straight ray; Martins et al., 2020) or update the ray geometry only occasionally to account for the non-linearity of the problem (Gorbatov et al., 2001; Bodin & Sambridge, 2009). Ray paths are perpendicular to the travel time field. Hence, after computing the travel time field with the fast-marching method, the ray path geometry can be calculated by starting at each receiver location in the travel time field and following the travel time gradient (∇T) back to the source location (Rawlinson & Sambridge, 2004). Once the ray paths are determined, integration of the slowness along each ray path is straightforward and travel times can be computed at relatively little computational expense.

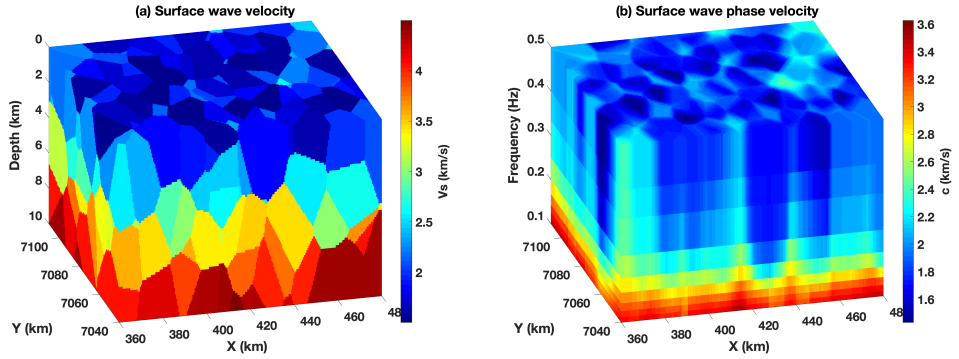

Figure 4.3. *Depth to frequency conversion of surface wave velocities using the modal approximation method. (**a**) Surface wave velocity model generated randomly using Voronoi cells. (**b**) Computed phase velocities corresponding to each depth profile using the modal approximation method.*

4.2.4 The prior

Since all inferences on the posterior are relative to the prior distribution, priors have great importance in Bayesian inversion schemes. The final result may suffer heavily from an incorrect prior. In order to prevent the introduction of prior-related biases into the solution, we choose uniform prior distributions with wide bounds for all model parameters. Assuming independent model parameters, the prior can be written as:

$$p(\mathbf{m}) = p(n)p(\mathbf{c}|n)p(\mathbf{v}|n)p(h), \tag{4.6}$$

where n is the number of Voronoi cells, $p(n)$ is the prior on the number of cells, $p(\mathbf{c}|n)$ is the prior on cell nuclei location, $p(\mathbf{v}|n)$ is the prior on cell velocity, and $p(h)$ is the prior on noise hyper-parameters or data uncertainty (see Bodin & Sambridge, 2009; Bodin et al., 2012, for details). The modal approximation method for computing phase velocities fails to compute the right surface wave mode when the model contains a layer whose velocity is lower than the velocity of the top layer (Galetti et al., 2017; Zhang et al., 2020). Hence, this issue has to be taken into account in the prior by discarding models for which the top layer does not have the lowest velocity value.

4

4.2.5 Reversible jump McMC

The reversible jump Markov chain draws samples from the posterior distribution employing an iterative stochastic process (such as the Metropolis–Hasting algorithm). The reverse jumps allow for a variable number of Voronoi cells, hence a variable number of parameters. Jumping between different model dimensions allows the rjMcMC algorithm to perform a global search (Andrieu et al., 1999). The algorithm proposes different types of model perturbations. Specifically, we use four different perturbation types to sample the posterior distribution efficiently (Bodin & Sambridge, 2009): a velocity update, Voronoi cell move, cell death and cell birth. In addition, we perturb the amplitude of the noise to infer the posterior probability of the errors on the measured surface wave travel times (this is introduced by Bodin et al., 2012). These perturbation types allow the model to dynamically adapt itself to data density, underlying velocity structure, and travel time noise.

The flowchart for the algorithm of the transdimensional McMC inversion is depicted in Figure 4.4. The process starts with a random initial model $\mathbf{m}$. Then, the algorithm draws the next sample of the chain by proposing a new model, $\mathbf{m}'$, based on a known proposal probability function, $q(\mathbf{m}'|\mathbf{m})$, which only depends on the previous state of the model $\mathbf{m}$. To propose a new model in a velocity update step and a Voronoi cell move, a Voronoi cell is selected randomly, then the velocity or the location of that cell is perturbed using a Gaussian proposal distribution. In a noise perturbation step, one of the two noise parameters at one frequency (i.e., a_j or b_j) is chosen randomly, then it is perturbed using a Gaussian proposal distribution. The proposed sample, then, will be accepted or rejected based on an acceptance probability for the proposed model, $\mathbf{m}'$ (Bodin et al., 2009). A new sample is drawn at each step of the Markov chain by perturbing the 3D velocity structure or the noise hyper-parameters (using one of the five perturbation types). The surface wave dispersion data (i.e., the frequency-dependent travel times) are then calculated to evaluate the following acceptance probability (Bodin & Sambridge, 2009):

$$\alpha(\mathbf{m}'|\mathbf{m}) = min\left[1, \frac{p(\mathbf{m}')}{p(\mathbf{m})}\frac{p(\mathbf{d}|\mathbf{m}')}{p(\mathbf{d}|\mathbf{m})}\frac{q(\mathbf{m}|\mathbf{m}')}{q(\mathbf{m}'|\mathbf{m})} \times |\mathbf{J}|\right], \tag{4.7}$$

where $\alpha(\mathbf{m}'|\mathbf{m})$ is the probability of accepting the proposed model $\mathbf{m}'$ given the

current model $\mathbf{m}$, $\frac{p(\mathbf{m}')}{p(\mathbf{m})}$ the prior probability ratio of two models, $\mathbf{d}$ the observed data (here these are the frequency-dependent travel times), $\frac{p(\mathbf{d}|\mathbf{m}')}{p(\mathbf{d}|\mathbf{m})}$ the likelihood ratio of the two models, $\frac{q(\mathbf{m}|\mathbf{m}')}{q(\mathbf{m}'|\mathbf{m})}$ the proposal ratio, and $\mathbf{J}$ is the Jacobian matrix, which accounts for (potential) differences in dimensionality between $\mathbf{m}$ and $\mathbf{m}'$ (resulting from a different number of Voronoi cells in $\mathbf{m}$ and $\mathbf{m}'$). For the birth and death steps used here, the determinant of the Jacobian matrix is unity (Bodin & Sambridge, 2009; Zhang et al., 2018).

When sufficient samples are drawn from the posterior, we can compute the mean, standard deviation, and other statistical measures of the posterior. The samples from a certain initial period of the chain are discarded. This initial sampling period is usually referred to as the burn-in period, which is the period that the algorithm needs to remove the effects of the initial model and reach sufficient mixing of the posterior samples. Since each sample is drawn based on a small perturbation of the previous model, adjacent samples are correlated or similar. To ensure that drawn samples are uncorrelated, we retain a sample every so many iterations; for example, every 200th model is retained. This process is usually referred to as 'thinning' of the chain.

4.3 Experiment setup and computational performance tests

To investigate the potential of the transdimensional algorithm for the interferometric surface wave responses of the RARR, we design three distinct 3D (block model) tests. With these tests, we evaluate the ability of the algorithm to recover subsurface models with different resolutions. In this section we introduce the three block models, but additionally conduct a number of experiments to determine acceptable values for the different numerical parameters (e.g., grid size). The results obtained by applying the transdimensional algorithm to travel times in the three block models are presented in the next section.

4.3.1 Ray path update and computational cost

The described transdimensional Markov chain naturally adapts model resolution to data resolution, implying it is self-regularized and self-smooth and hence does not require the regularization and/or smoothing needed in deterministic inversions (e.g., Martins et al., 2020). In addition, model uncertainty is naturally captured in the posterior. Despite these benefits, the high computational cost is still a drawback of the method. To sample the posterior sufficiently well, we need to run multiple chains for at least a million iterations.

As we mentioned earlier, computing frequency-dependent travel times using the fast-marching method contributes most to the computational cost. To make the algorithm computationally less demanding, Bodin et al. (2012) used fixed ray paths to compute travel times and updated the ray paths only occasionally (three times for three million samples). In this way, they linearized the algorithm partially. Galetti

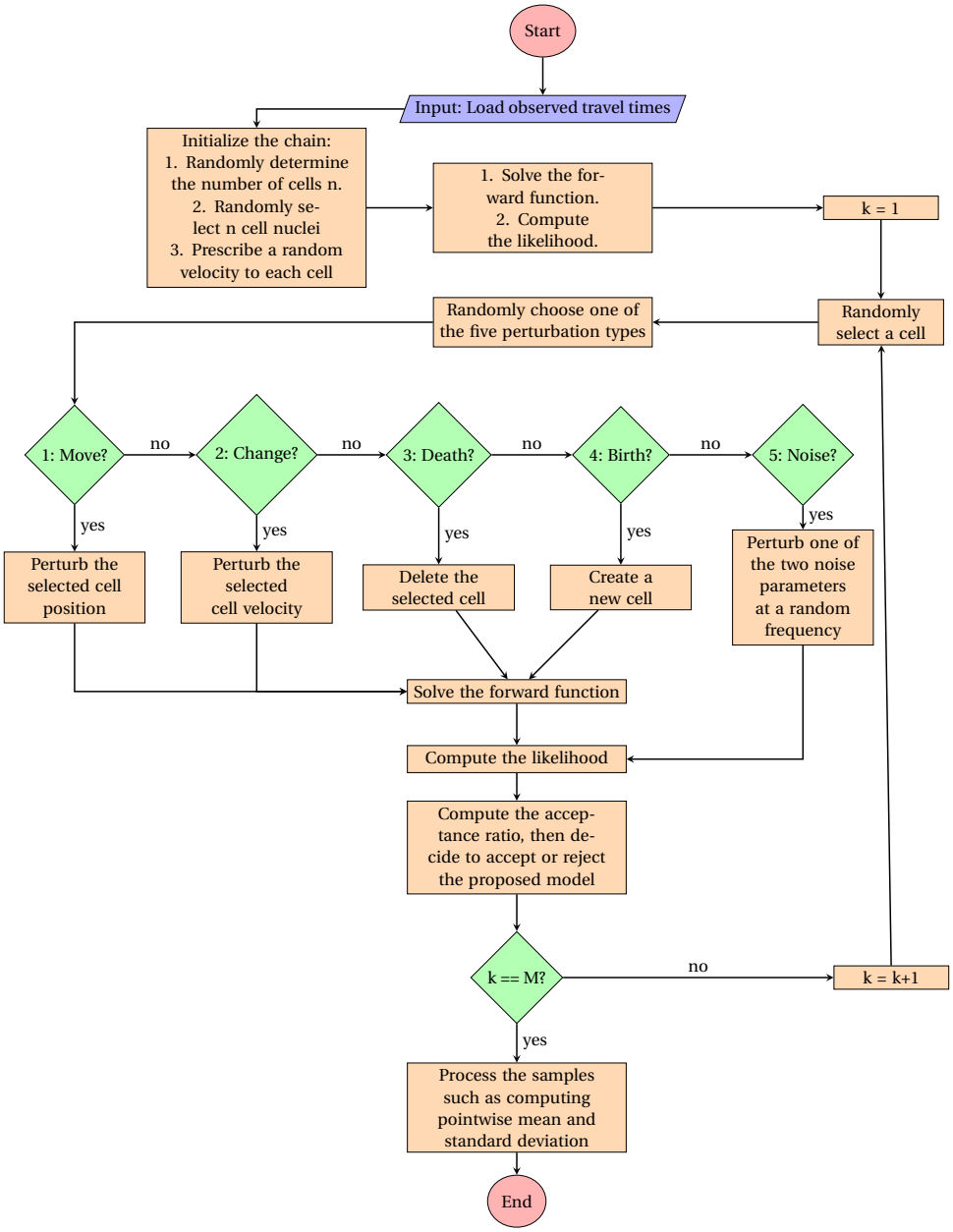

Figure 4.4. *Flowchart of the transdimensional Markov chain Monte Carlo algorithm used in this work. Here, a total of M samples is drawn from the posterior.*

et al. (2017) argued that this might introduce artifacts and bias into the solution. Therefore, Galetti et al. (2017) and Zhang et al. (2020) updated the ray paths at each step of the Markov chain.

At the same time, we know that each new sample involves only a small perturbation of the model. Consequently, ray paths do not change too much in one thinning "period" (in our case, every 200 iterations). Hence, we update ray paths every 200 iterations based on the average velocity of the previous 200 samples. In this way, we reduce the computational cost significantly while still retaining most of the non-linearity. Figure 4.5 shows the speed-up associated with different ray path update steps (with respect to updating ray paths at every chain step). The dimension of our assumed model is 120 km by 70 km. We used a constant grid spacing of 0.5 km in the depth direction (used for the modal approximation method; Herrmann, 2013). Then, we compared the time needed to take three million Markov chain steps using grid spacing of 0.5 km, 1 km, and 2 km in the two horizontal directions. Figure 4.5 demonstrates that updating ray paths every 200 iterations significantly decreases computational costs. Updating the ray paths less frequently (i.e., using higher update step), however, does not reduce computational cost much more. Hence, we consider updating ray paths every 200 iterations optimal in terms of both computational cost and honoring the non-linearity of the problem.

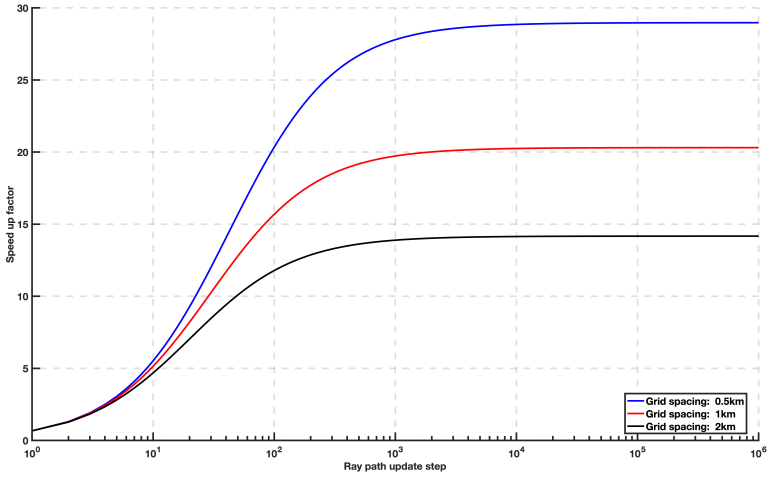

Figure 4.5. *Computation time speed-up as a function of the frequency at which ray paths are updated. The speed up is depicted for three different FMM resolutions.*

4.3.2 Block models

The three considered synthetic models are depicted in Figure 4.6. Figure 4.6a depicts a block model with blocks of size 20 km × 20 km × 10 km in the northing, easting, and depth directions, respectively. We will henceforth refer to this subsurface model as the coarse block model. Figure 4.6b depicts a block model with blocks of size 10 km × 10 km × 5 km in the northing, easting, and depth directions, respectively.

We will henceforth refer to this subsurface model as the intermediate block model. Figure 4.6c depicts a block model with blocks of size 5 km × 5 km × 2.5 km in the northing, easting, and depth directions, respectively. We will henceforth refer to this subsurface model as the fine block model. In addition to these resolution tests, we study the impact of additive noise on the ability of the algorithm to adapt the model to (and to estimate) the noise level.

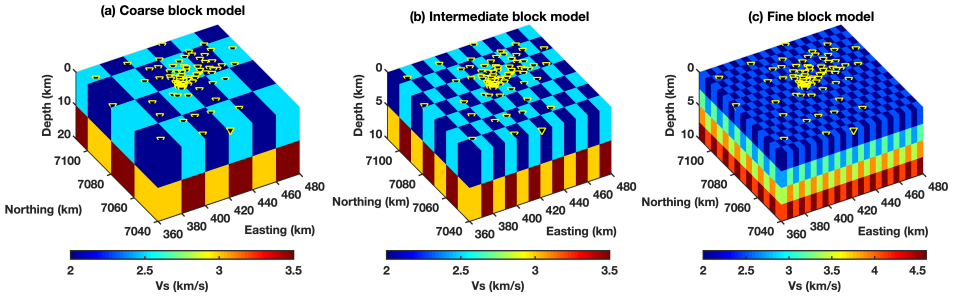

Figure 4.6. *Three different synthetic block models to test the 3D transdimensional algorithm. (**a**) Coarse block model, (**b**) Intermediate block model, (**c**) Fine block model. Inverted yellow triangles indicate the locations of the stations of the RARR (See also Figure 4.1).*

4.3.3 Sensitivity kernels

Each of the three block models in Figure 4.6 has only two distinct velocity profiles, of which one is shown in the left panel of Figure 4.7a,d,g. The other velocity profiles (not shown) have coinciding step sizes and depths, but their velocities are simply 500 m/s higher for each layer. The middle panel of this figure (b, e, h) depicts the associated sensitivity kernels of the Rayleigh waves computed using the modal approximation method (Herrmann, 2013). For different frequencies, these kernels give the Rayleigh waves' sensitivity to the shear wave velocity as a function of depth.

Figure 4.7b shows that Rayleigh waves in the frequency range of 0.1–0.5 Hz are predominantly sensitive to the shear wave velocities of the shallowest 10 km. Hence, we do not expect the algorithm to recover the shear wave velocity below that depth very well in the coarse block model. Figure 4.7e,h show that Rayleigh waves in the frequency range 0.1–0.5 Hz are sensitive to the shear wave velocities of all blocks of the intermediate and fine block models down to 10 km, and should, in principle, be able to recover these blocks. We, therefore, expect to recover the velocity structure in areas traversed by sufficient ray paths. A decrease in resolution with increasing depth is expected. The right panel of Figure 4.7 is the phase velocity for the corresponding depth profile of shear wave velocity at ten different discrete frequencies in the frequency range of 0.1–0.5 Hz using the modal approximation method (Herrmann, 2013).

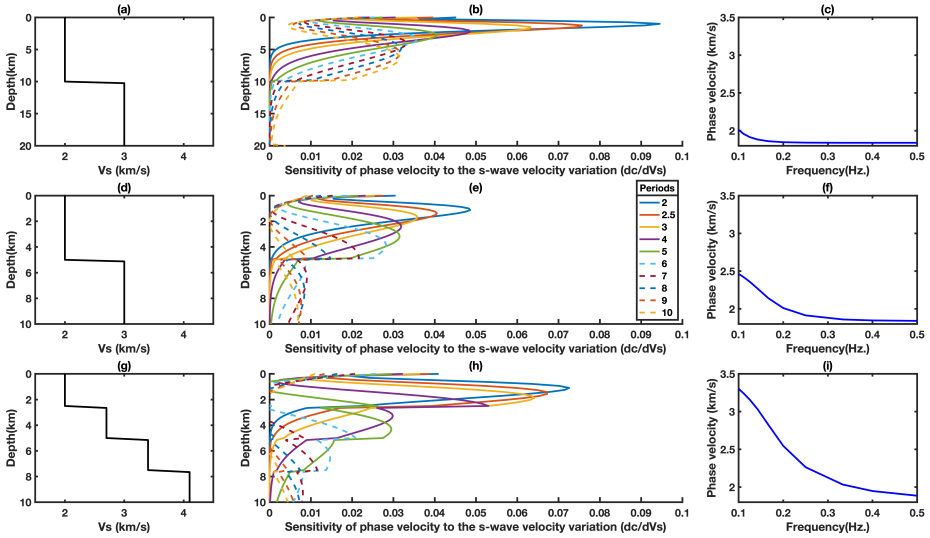

Figure 4.7. *Surface wave sensitivity analysis of one of the depth profiles of each block model. The left column displays shear wave velocity as a function of depth for (**a**) the coarse block model, (**d**) the intermediate block model, and (**g**) the fine block model. The middle column (**b**,**e**,**h**) displays the corresponding sensitivity of the Rayleigh waves for different periods (1/f) as a function of depth. On the right (**c**,**f**,**i**), the corresponding phase velocity dispersion is shown as a function of frequency.*

4.3.4 Additive noise and modeling errors

As we mentioned before, noise parameters are assumed to be unknown and are estimated by the transdimensional algorithm. To evaluate the ability of the algorithm to recover the noise level, we designed a noise-free experiment and an experiment with additive Gaussian random noise. A noise-free experiment means that we did not add any additive noise to the modeled synthetic data. Modeling errors (effectively resulting in noise) are, however, still present. These are relatively small, and we therefore nevertheless refer to this experiment as a noise-free experiment. In the second experiment, after computing frequency-dependent travel times through the true synthetic block models of Figure 4.6, we have added random Gaussian noise with a variance based on Equation 4.4 with $a_j = 0.04$ and $b_j = 0.1$.

To determine the number of computational grid points while solving the forward function of the transdimensional algorithm and a reasonable level of additive noise, we designed two tests. First, we considered the fine block model of Figure 4.6c. Then, we computed the travel times between the RARR stations at a frequency of 0.1 Hz, which implies, on average, a wavelength of 20 km. Travel times were computed for four different grid sizes (61 × 36 × 21, 121 × 71 × 41, 241 × 141 × 81, and 481 × 281 × 161). The corresponding grid separations are 2 km × 2 km × 0.5 km, 1 km × 1 km × 0.25 km, 0.5 km × 0.5 km × 0.125 km, and 0.25 km × 0.25 km × 0.0625 km, respectively. Assuming the obtained travel times with the finer grid points (481 × 281 × 161) as a reference, we calculated the other three grids' relative errors. Errors

are then sorted based on interstation distances and are presented in Figure 4.8a. As such, we get an impression of the modeling errors associated with different grid sizes. In the second test, we used the randomly generated model of Figure 4.3a and followed the same procedure as the first test. Relative errors are presented in Figure 4.8b. The relative error due to a random Gaussian noise based on Equation 4.4 with $a_j = 0.04$ and $b_j = 0.1$ is also presented in this figure by the green solid line. The relative error is around 5% at longer distances and reaches more than 30% at shorter distances. We believe this represents the available noise in a real case study. Additionally, it seems that the modeling error is compatible with the assumed linear relation for the noise variance, Equation 4.4.

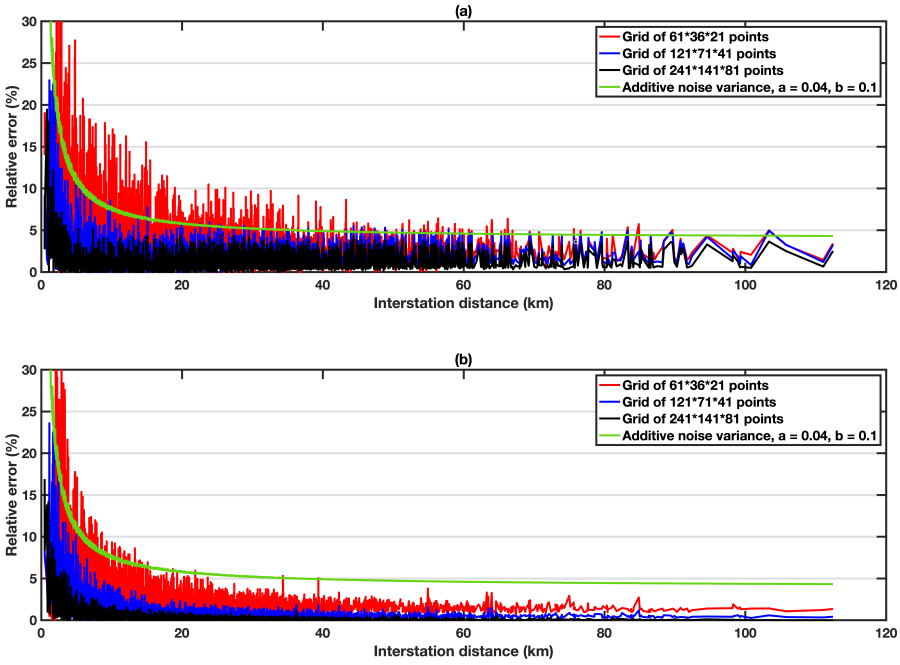

Figure 4.8. *Two tests to analyze modeling errors. (**a**) Relative modeling errors while computing travel times through the fine block model of Figure 4.6c using three different grid resolutions. (**b**) Modeling errors for computing travel times through the randomly generated model of Figure 4.3a using three different grid resolutions. Relative error due to the additive random Gaussian noise based on Equation 4.4 with $a_j = 0.04$ and $b_j = 0.1$ is also included in green line on both (**a**,**b**).*

We deduce from Figure 4.8 that the modeling errors at short distances are much higher than at long distances. In particular, we consider the modeling errors using a grid of $61 \times 36 \times 21$ unacceptably high at short distances. We consider modeling errors using a grid of $121 \times 71 \times 41$ and $241 \times 141 \times 81$ points acceptable. They are low enough to be used in our modeling and inversion. That is why we select the grid of $241 \times 141 \times 81$ points to compute the synthetic travel times (i.e., observed travel

times). Solving the forward problem using a grid of $241 \times 141 \times 81$ points, however, renders the transdimensional Markov chain computationally very expensive (given the size of our computational cluster). Consequently, we use a grid of $121 \times 71 \times 41$ points while running the Markov chain.

It is useful to note that, in application to field data, we will discard travel times associated with interstation distances shorter than 1.5 wavelength. In practice, given (i) a maximum frequency of 0.5 Hz for which reliable interferometric surface wave responses can be retrieved and (ii) an average phase velocity of about 2 km/s at that frequency, no travel times associated with interstation distances shorter than approximately 6 km will serve as input.

4.3.5 Modeling and inversion parameters

The modeling and inversion parameters used in the synthetic experiments are presented in Table 4.1. We used the same inversion parameters for the noise-free experiments and the experiments with additive noise. We started the transdimensional sampling of the posterior with a random initial model in all experiments, implying that the number of Voronoi cells, their position and their velocities were chosen randomly. However, to take into account the necessity of having the lowest velocity at the surface, the initial model was generated, increasing in depth, yet randomly. As can be seen in Table 4.1, we generated synthetic frequency-dependent travel times ("observed" data) on a relatively fine grid for all three block models. While computing the frequency-dependent travel times (forward modeling) during McMC sampling, however, we used a coarse grid. Finally, we used a finer grid for calculating the post-burn-in pointwise average and standard deviation of the sampled models.

For drawing new velocity values as well as new nuclei locations, we used Gaussian proposal probability distributions. The width of the proposal distributions controls the chance of a proposed model being accepted and, consequently, the transdimensional algorithm's convergence rate. On the one hand, narrow proposal distributions lead to higher acceptance ratios, more correlated samples, and a lower convergence rate. On the other hand, wide proposal distributions lead to lower acceptance ratios and consequently lower convergence rates. Previous studies suggest that an efficient proposal distribution width results in an acceptance ratio of 25%–50% (Bodin et al., 2009; Gelman et al., 1996). These values were determined, a priori, from the data. We determined the efficient proposal distribution width through a pilot run of the algorithm and looked at samples' acceptance ratios of different perturbation types. This means that one does (of course) not need to know the true velocity model to define the proposal widths. The obtained proposal widths for the velocity update, moving a cell and noise perturbation are presented in Table 4.1. The valid range of parameters presented in the table defines the bounds of the uniform prior on each parameter. To reduce computational cost while still preserving the non-linearity of the problem, we updated ray paths at every 200 iterations as we discussed earlier. Thinning was also achieved by retaining every 200th model.

Table 4.1. *Modeling and inversion parameters. Parameters are the same for the noise-free experiment and the experiment with synthetic additive noise.*

Modeling and Inversion Parameters	Coarse Block Model	Intermediate Block Model	Fine Block Model
Model dimension (km)	120 × 70 × 20	120 × 70 × 10	120 × 70 × 10
Number of grid points in generating synthetic data	241 × 141 × 81	241 × 141 × 81	241 × 141 × 81
Number of grid points in McMC sampling	121 × 71 × 41	121 × 71 × 41	121 × 71 × 41
Number of grid points for calculating post-burn-in pointwise average	241 × 141 × 41	241 × 141 × 41	241 × 141 × 41
Valid range of shear wave velocity (km/s)	1.5–6	1.5–6	1.5–6
Valid range of noise hyper parameter a	10^{-5}–1	10^{-5}–1	10^{-5}–1
Valid range of noise hyper parameter b	0-2	0–2	0–2
Proposal width for a move step. Md is the model dimension.	$0.07Md$	$0.06Md$	$0.05Md$
Velocity proposal width (km/s)	0.4	0.4	0.3
Proposal width for a	10^{-3}	10^{-3}	10^{-3}
Proposal width for b	10^{-2}	10^{-2}	10^{-2}
Thinning level	200	200	200
Ray path update step	200	200	200

4.4 Results and discussion

In this section, we present the results obtained by applying the transdimensional Markov sampler to the synthetic travel times through the block models introduced in Figure 4.6. That is, the travel times between the RARR stations (computed using a grid of $241 \times 141 \times 81$ points) serve as input, that is, as the observed data.

4.4.1 Coarse block model

Figure 4.9 shows the results of the one-step 3D transdimensional method for the coarse block model of Figure 4.6a in the noise-free experiment. A horizontal slice at the surface of the model and two vertical cross-sections of the true velocity model are depicted in Figure 4.9a–c. Figures 4.9d–f depict the (pointwise) average of all post-burn-in models (after thinning). The bottom row of this figure (Figure 4.9g–i) provides an estimate of the model uncertainty, that is, the post-burn-in (pointwise) standard deviation. Retained models are obtained by thinning ten separate transdimensional Markov chains, each with 1×10^6 iterations of which 4×10^5 are considered burn-in steps. Since thinning involves retaining one in every 200 iterations in our case, 30,000 samples are used for the computation of the pointwise average and standard deviation.

Figure 4.9 shows that the algorithm recovered the velocity distribution at the

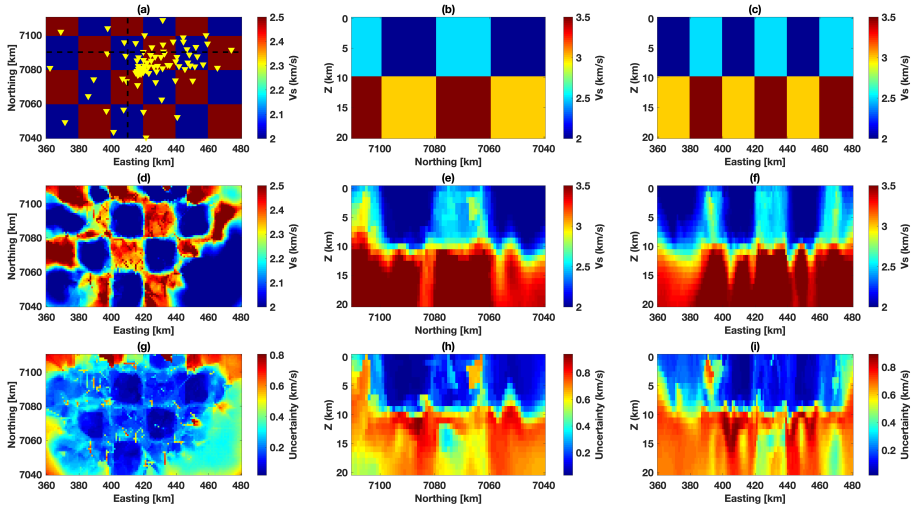

Figure 4.9. *Transdimensional tomographic models estimated from noise-free synthetic travel times through the coarse block model in Figure 4.6a. The true block model: (**a**) horizontal slice at the surface of the model including station locations, (**b**) vertical cross-section at easting of 410 km, and (**c**) vertical cross-section at northing of 7090 km. The vertical cross-sections are indicated with black dashed lines in (**a**). (**d–f**) Pointwise averaged velocities calculated from post-burn-in retained samples. (**g–i**) Standard deviation (model uncertainty) calculated from post-burn-in retained samples.*

surface very well. In line with the low sensitivity of the sensitivity kernels to greater depth (Figure 4.7b), the velocity structure below 10 km is not recovered very well, and reveals a higher uncertainty than at shallower depth. Figure 4.10 is similar to Figure 4.9, but presents the results in the experiment with additive noise. Comparing Figure 4.9d–f and Figure 4.10d–f shows that the additive Gaussian noise results in a smoother (pointwise averaged) model. The block interfaces are clearly visible in the uncertainty maps of Figure 4.10g–i. Though the velocity models are not recovered very well in deeper parts of Figure 4.10d–f, the deeper subsurface structure is reflected in the uncertainty maps of Figure 4.10g–i. This exemplifies why the uncertainties aid the interpretation of the results.

Comparing the average maps and the uncertainty maps of Figures 4.9 and 4.10, we can conclude that the rjMcMC converges faster in case of higher noise levels. The results presented in Figure 4.9 suggest that more iterations are needed to sample the posterior sufficiently well (this will be discussed in more detail in Section 4.4.4). We explain this by the fact that stronger noise (σ in Equation 4.3, which we also estimate by means of the hyper-parameters) results in a flatter likelihood. This makes it easier to explore the posterior compared to a narrower likelihood associated with less noise (i.e., a smaller σ). Mathematically speaking, a higher σ simply increases the acceptance ratio of the Markov chain and hence results in more unique samples. Consequently, the pointwise average of all sampled models (after burn-in) is likely to be smoother and closer to the true posterior. In the case of

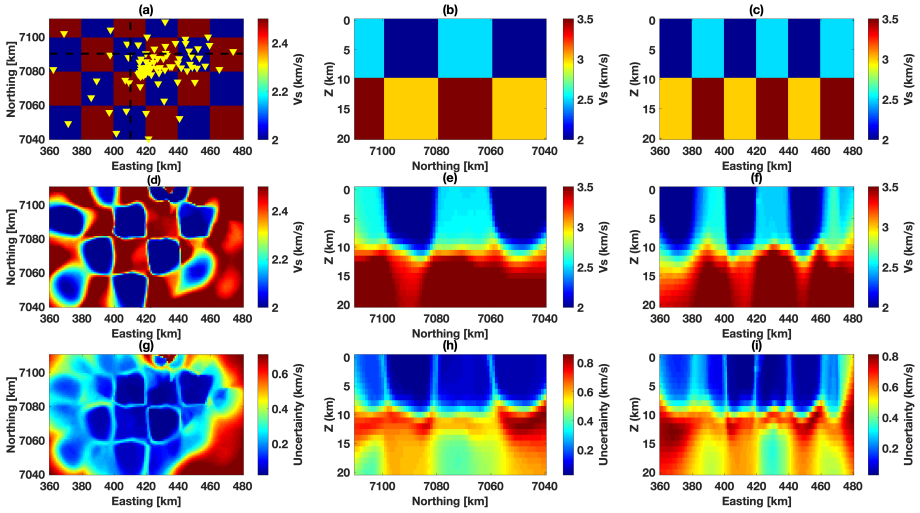

Figure 4.10. *As Figure 4.9 but estimated from synthetic travel times containing Gaussian random noise.*

a noise-free experiment, we could use a fixed (higher) noise estimate to achieve a smoother result. However, we would lose resolution unnecessarily by imposing such a higher value. Of course, were one to have ample computational power, one could simply run the Markov chains for the noise-free experiment for a longer time to better approach the posterior.

4.4.2 Intermediate block model

Figure 4.11 shows the results of the one-step 3D transdimensional method for the intermediate block model of Figure 4.6b in the noise-free experiment. Figure 4.11a–c depicts the horizontal slice at the surface of the model and two vertical cross-sections of the true velocity model. Figure 4.11d–f depicts the post-burn-in pointwise average of the retained velocity models. Figure 4.11g–i depicts the uncertainty, which is the post-burn-in standard deviation of the retained samples.

Figure 4.11 reveals that the algorithm recovered the true velocity model well in both horizontal and vertical directions in densely sampled regions. Regions that are not sampled that well by the data (i.e., regions traversed by few ray paths) are recovered less well; for example, the eastern part of the velocity model. These regions also exhibit larger uncertainties estimated from the pointwise averages. The fact that the algorithm results in smoother pointwise averages in regions sampled by fewer rays, is the reason that the transdimensional algorithm is often referred to as a self-smooth, self-regularized algorithm.

Figure 4.12 is similar to Figure 4.11 but presents the results in the case of additive noise. Similar to our findings for the coarse block model, the additive Gaussian noise results in a smoother (pointwise averaged) model. Block interfaces and areas traversed by no (or few) ray paths show higher uncertainties, as one would expect.

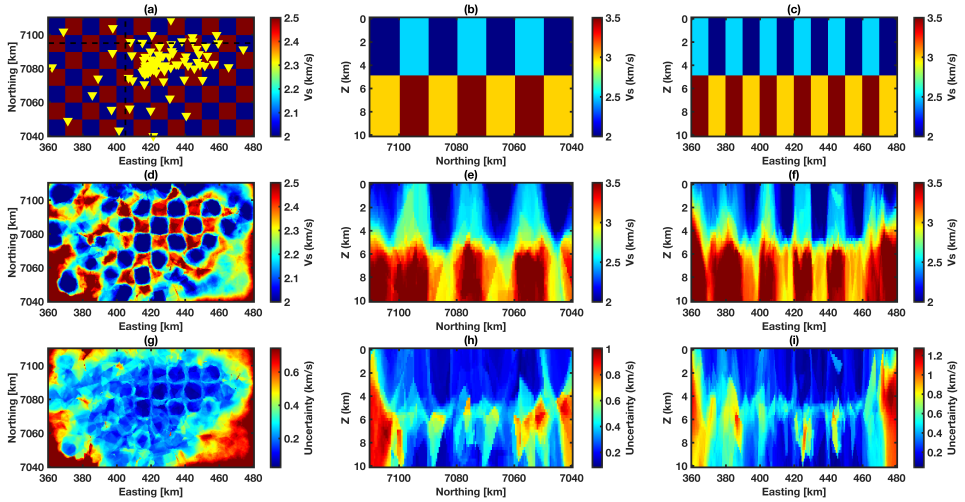

Figure 4.11. *As Figure 4.9 but for the noise-free synthetic travel times through the intermediate block model in Figure 4.6b.*

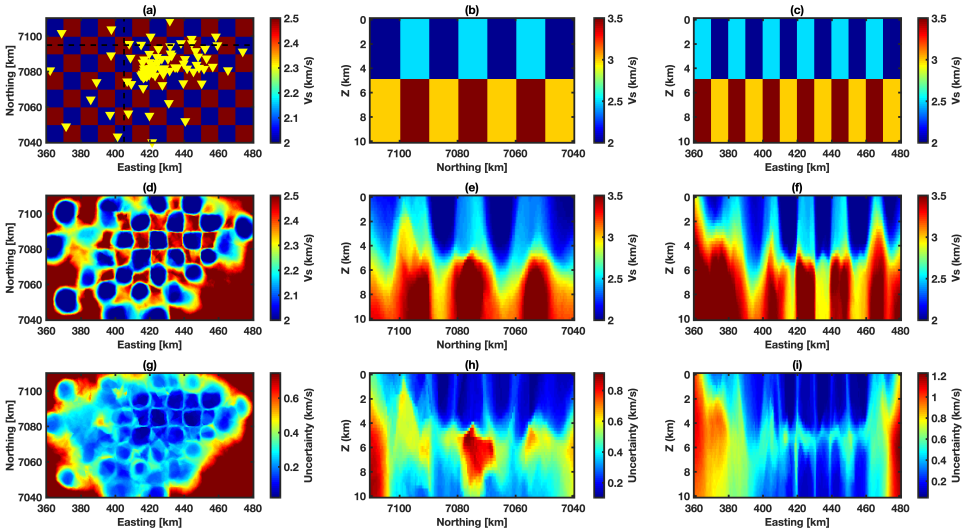

Figure 4.12. *As Figure 4.9 but for the synthetic travel times containing Gaussian random noise for the intermediate block model in Figure 4.6b.*

4.4.3 Fine block model

Figure 4.13 shows the results of the one-step 3D transdimensional method for the fine block model of Figure 4.6c with no additive noise on the travel times. Because of the greater complexity of the fine block model, we used 20 chains (instead of 10) to sample the posterior. Each chain generated 2×10^6 samples, of which 1×10^6 samples are considered part of the burn-in period. Figure 4.13a–c depicts the true

velocity model by means of a horizontal slice at the surface of the model and two vertical cross-sections. Figure 4.13d–f represent the recovered velocity models, which are the post-burn-in pointwise averages of the retained samples. Retaining again every 200 iterations, the pointwise averages and standard deviation are computed from a total of 100,000 samples. As one can see, the algorithm recovered the blocks fairly well in the densely sampled area of the model. Figure 4.13g–i estimates the model uncertainty through the computation of the post-burn-in standard deviation of the retained samples.

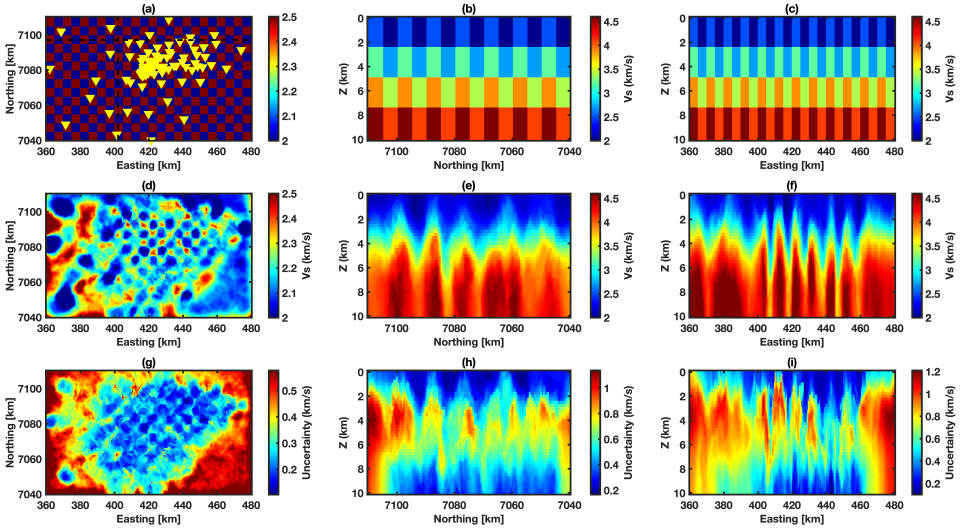

Figure 4.13. *As Figure 4.9 but for the noise-free synthetic travel times for the fine block model in Figure 4.6c.*

Figure 4.14 is the same as Figure 4.13 but presents the results in the case of noisy travel times. Similar to our observations for the other two block models, the additive Gaussian noise results in a smoother (pointwise averaged) model. Both the noise free and the noisy travel times result in pointwise averaged velocity models exhibiting large uncertainty compared to the velocity models recovered for the intermediate and coarse block models.

4.4.4 Chain statistics and convergence

To evaluate the ability of the algorithm to infer the noise level and complexity of the model space, we show here the chain statistics for the intermediate block model. Results are approximately the same for the other two block models (i.e., the coarse block model and the fine block model). Figure 4.15 shows how misfit, number of cells (model dimension), and noise hyper-parameters change during McMC sampling. Figures 4.15a–d are for the noise-free experiment, and Figures 4.15e–h are for the experiment with additive noise. Different colors represent different chains. Noise hyper-parameters are presented for a single frequency as they vary

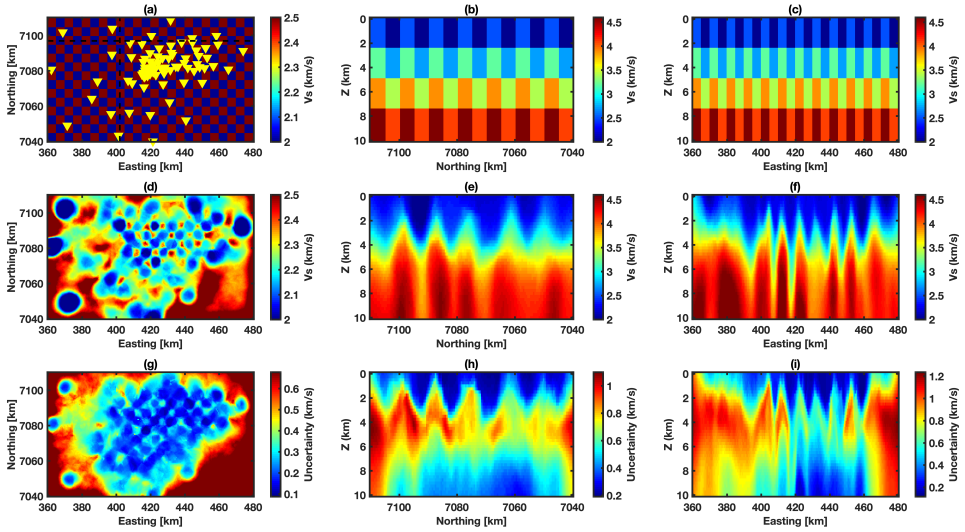

Figure 4.14. *As Figure 4.9 but for the synthetic travel times containing Gaussian random noise for the fine block model in Figure 4.6c.*

by frequency. Looking at this figure, the number of cells converged to a small number of cells (around 300) in the experiment with additive noise. In the noise-free experiment, however, the number of cells approaches higher values and also the variation between different chains is larger. For the inferred noise level, in the experiment with additive Gaussian random noise, the recovered hyper-parameter a is fairly close to the true value. However, the recovered hyper-parameter b slightly underestimates the true value.

The results presented in Figure 4.15 can also be used as a means to determine chain convergence and the length of the burn-in period. As one can see, for the experiment with additive Gaussian noise, all parameters at all chains stabilize around the same value. This stationarity and convergence can be interpreted as a fully mixed Markov chain. For the noise-free experiment, however, it seems as if the separate chains still need more time to stabilize entirely; the misfit and the noise hyper-parameter are still decreasing, and the number of cells is still increasing. It means that if we continue sampling from the posterior for the noise-free experiment, the quality of results will improve and the Markov chain will reach a steady state. In other words, the experiment with additive Gaussian noise converged faster and hence better explores the posterior distribution for the same number of samples.

4.5 Conclusions

In this chapter, we investigated the ability of 3D transdimensional Markov chain Monte Carlo algorithm to recover the 3D surface wave velocity structure of the Reykjanes peninsula. Anticipating the future application of this algorithm to interferometric travel times extracted from ambient seismic noise, we specifically

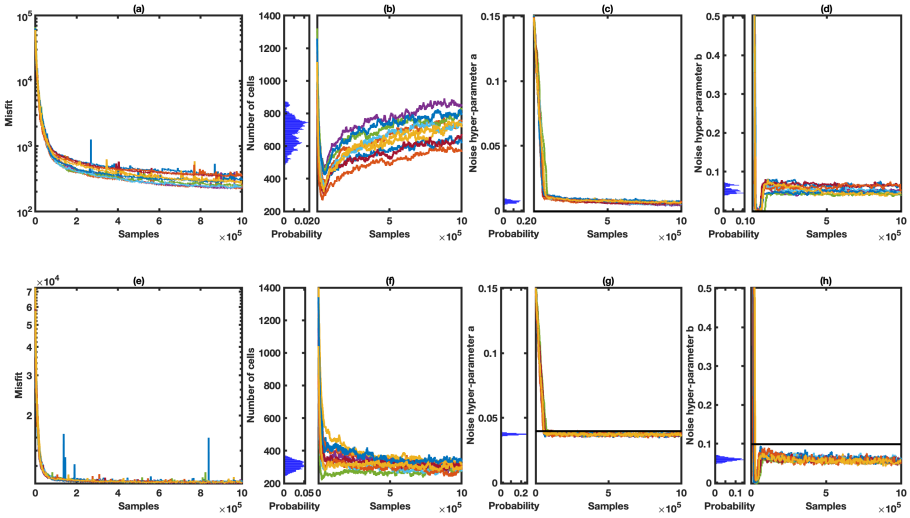

Figure 4.15. *Variation of the misfit, the number of cells (dimensionality of model space), and the noise hyper-parameters during ten chains of McMC sampling for the intermediate block model in the noise-free experiment (**a**–**d**) and the experiment with additive Gaussian noise (**e**–**h**). Each color represents a sampling chain. Noise hyper-parameters are plotted for a single frequency. The black lines in (**g**–**h**) represent the actual values. Histograms of the posterior distribution for the retained models for each parameter are shown as insets of each panel.*

considered travel times between stations of the Reykjanes seismic array. We find that updating ray paths every 200 iterations does not significantly affect the performance of the algorithm (i.e., it honors the non-linearity of the problem sufficiently), while at the same time significantly reducing computational costs. Our results show that the algorithm successfully adapts model resolution to ray density and hence yields a higher resolution and lower uncertainty in more densely sampled areas. Similarly, the uncertainty is larger in regions where the station density is lower. In addition, the algorithm successfully adapts to the noise level of the observed travel times; smoother models are obtained for higher levels of additive random noise. The algorithm converges (i.e., stabilizes) faster with a higher noise level because noise flattens the posterior and, consequently, the posterior is easier to explore. The uncertainty maps aid the interpretation of the results. The block interfaces are visible in uncertainty maps with higher uncertainties.

5

3D ambient-noise surface wave tomography of the Reykjanes Peninsula, SW Iceland

Abstract: Ambient noise seismic tomography has proven to be an effective tool for subsurface imaging, particularly in volcanic regions such as the Reykjanes Peninsula (RP), SW Iceland, where ambient seismic noise is ideal with isotropic illumination. The primary purpose of this study is to obtain a reliable shear wave velocity model of the RP, to get a better understanding of the subsurface structure of the RP and how it relates to other geoscientific results. This is the first tomographic model of the RP which is based on both on- and off-shore seismic stations. We use the ambient seismic noise data and apply a novel algorithm called one-step 3D transdimensional tomography. The main geological structures in the study area (i.e., covered by seismic stations) are the four NE-SW trending volcanic systems, oriented highly oblique to the plate spreading on the RP. These are from west to east; Reykjanes, Eldvörp-Svartsengi, Fagradalsfjall, and Krýsuvík, of which all except Fagradalsfjall host a known high-temperature geothermal field. Using surface waves retrieved from ambient noise recordings, we recovered a 3D model of shear wave velocity. We observe low-velocity anomalies below these known high-temperature fields. The observed low-velocity anomalies below Reykjanes and Eldvörp-Svartsengi are significant but relatively small. The low-velocity anomaly observed below Krýsuvík is both larger and stronger, oriented near-perpendicular to the volcanic

This chapter is published as:
Dalkhani, A. R., Ágústsdóttir, T., Gudnason, E. Á., Gylfi, P. H., Zhang, X., & Weemstra, C. (2023). Transdimensional ambient-noise surface wave tomography of the Reykjanes Peninsula, SW Iceland. *Geophysical Journal International*, https://doi.org/10.1093/gji/ggad435.
Minor modifications have been applied to keep consistency within this thesis.
The data underlying this chapter are also published as open access and are available at https://doi.org/10.4121/3c97b1c8-1736-495d-a2f9-bd26dc958575.

system, and coinciding well with a previously found low-resistivity anomaly. A low-velocity anomaly in the depth range of 5 to 8 km extends horizontally along the whole RP, but below the high-temperature fields, the onset of the velocity decrease is shallower, at around 3 km depth. This is in good agreement with the brittle-ductile transition zone on the RP. In considerably greater detail, our results confirm previous tomographic models obtained in the area. This study demonstrates the potential of the entirely data-driven, one-step 3D transdimensional ambient noise tomography as a routine tomography tool and a complementary seismological tool for geothermal exploration, providing an enhanced understanding of the upper crustal structure of the RP.

5.1 Introduction

The Reykjanes Peninsula (RP), southwest Iceland, is the onshore continuation of the Mid-Atlantic Ridge. As such, it is part of the divergent plate boundary of the North American and Eurasian plates. On the RP, this plate boundary strikes N70°E (Sigmundsson et al., 2020), and the divergence of the plates is expressed in six en-echelon rift segments, which accommodate the rifting (Sæmundsson et al., 2020). These rift segments, or volcanic systems, are areas with the highest density of eruptive fissures and tectonic faults and fractures. Currently, there are two geothermal power plants in production on the RP, i.e., in Reykjanes (100 MWe) and Svartsengi (76 MWe and 150 MWt), mainly producing from depths of 1 to 2.5 km (Figure 5.1) (Friðleifsson et al., 2020).

Further exploration of deep geothermal resources is currently underway. In 2016-2017, a deep exploratory well (IDDP-2) was drilled down to a depth of 4.6 km in Reykjanes to examine the economic potential of the production of supercritical fluids from greater depths than conventional production wells. The IDDP-2 well reached both supercritical conditions, evidenced by a temperature estimated to be around 600°C at the bottom of the well (Bali et al., 2020), and permeability at depths greater than 3 km, evidenced by a total loss of circulation below 3 km during drilling. In addition, seismicity was induced below 3 km, in a zone that was generally aseismic prior to drilling (Gudnason et al., 2020; Friðleifsson et al., 2020). For further geothermal utilization, more investigation is needed to better understand the crustal structure beneath the RP as a whole.

The RP has been the subject of several different geological (Clifton & Kattenhorn, 2006; Sæmundsson & Sigurgeirsson, 2013; Sæmundsson et al., 2020) and geophysical studies. See Jousset et al. (2020b) for an exhaustive list of recent geophysical studies. In particular, the recent volcano-tectonic unrest period at Fagradalsfjall and the subsequent eruptions in 2021, 2022, and 2023 (the first eruptions on the RP in roughly 780 years) have drawn Fagradalsfjall and the RP as a whole into the spotlight (Einarsson et al., 2023; Flóvenz et al., 2022; Halldórsson et al., 2022; Pedersen et al., 2022; Sigmundsson et al., 2022). Relatively high-resolution shear wave images have the potential to reveal more details of the RP's subsurface in general and the volcanic systems in particular. Ambient noise surface wave tomography (ANSWT) has great potential in this context (e.g., Lehujeur et al., 2016; Zhang et al., 2020). This is due to (i) the 3D shear wave images it can provide in the absence of active seismic sources,

(ii) its relatively low costs, supplementary to a local seismic network, and (iii) the considerable investigation depth it can reach, compared to many other geophysical methods (Cruz-Hernández et al., 2022).

Jousset et al. (2016) used recordings by 26 seismic stations on the RP to retrieve both surface and body waves. The seismic stations used by Jousset et al. (2016) constitute a subset of the IMAGE seismic network (for details regarding the IMAGE project we refer to Hersir et al., 2020b; Blanck et al., 2020). Martins et al. (2020) used the noise recorded by (almost) the same subset as Jousset et al. (2016) to image part of the RP by means of deterministic ANSWT. Even though their findings enhanced details compared to previous models, the resolution and lateral extent of the obtained images are limited. Both studies used a subset of the IMAGE stations because the recordings by the Ocean Bottom Seismometers (OBSs) (also deployed in the context of IMAGE) were subject to clock drift. In addition, the IMAGE seismic network was extended with stations from other existing seismic networks on the RP. We henceforth refer to the combined set of stations as the 'extended IMAGE seismic network' (i.e., the IMAGE stations complimented with additional stations from the existing seismic networks; see Section 5.3 for further details). The recordings by some of the additional stations of the existing networks also turned out to be subject to timing errors in the frequency band of interest. Weemstra et al. (2021) quantified both the average clock drift by most of the OBSs and the timing errors of most of the stations of the existing seismic networks. Removal of the recovered timing errors allows those recordings to be used for ANSWT. This significantly increases lateral extent and resolution compared to Jousset et al. (2016) and Martins et al. (2020). We finally highlight that what is referred to as the extended IMAGE seismic network in this study, is referred to as the Reykjanes array (RARR) in Weemstra et al. (2021) and chapter 4.

In this chapter, we use a recently developed probabilistic tomographic algorithm (Zhang et al., 2018, 2020, see chapter 4) to perform ANSWT of the RP. The shear wave velocities obtained in this chapter result from a 3D, one-step Bayesian tomographic inversion (Zhang et al., 2018), which has its roots in the transdimensional inversion algorithm introduced by Bodin & Sambridge (2009). In chapter 4, we modified the algorithm in the sense that they update the ray paths less frequently (i.e., not at every perturbation step), while at the same time still honoring the non-linear aspect of the tomographic problem. They tested the modified algorithm on synthetic station-station travel times generated for the configuration of the extended IMAGE seismic network and the surface wave frequencies of interest (i.e., 0.1-0.5 Hz). In this chapter, we apply the modified algorithm to the extended IMAGE data set. First, we retrieve station-station surface wave phase travel times from the time-corrected ambient noise recordings (Weemstra et al., 2021). Then, we use these surface waves' dispersion curves to generate 3D images of the RP subsurface' shear wave velocity. Finally, we interpret the recovered shear wave velocities, discuss how they compare to other recent geophysical studies, and list the most important conclusions.

5.2 Geological setting

The tectonic structure of the RP is characterized by six volcanic systems, arranged en-echelon along the divergent plate boundary of the North American and Eurasian plates. On the RP, this plate boundary is approximately 60 km long, from the SW tip of the Peninsula, until it joins the Western Volcanic Zone and the South Iceland Seismic Zone at the Hengill triple junction in the east. The RP oblique rift is expressed by a 5-10 km wide seismic and volcanic zone along the Peninsula, and is highly oblique with the spreading direction of N120°E in this region (Sigmundsson et al., 2020; Sæmundsson et al., 2020). Four of the six identified volcanic systems of the RP are within our area of study (all six are shown in Figure 5.1 as shaded light brown polygons).

The volcanic systems on the RP are grouped by the presence of eruptive fissures and the density of tectonic faults and fractures. Their outlines or boundaries are rough estimates, drawn according to Sæmundsson & Sigurgeirsson (2013). During the last RP rifting episode, ca. 1200 - 780 years before present, all the RP's volcanic systems were volcanically active in intervals, except Fagradalsfjall and Hengill (Sæmundsson & Sigurgeirsson, 2013). The extensional component of the rifting is accommodated by the intrusion of magma in NE-SW oriented dykes, oblique to the plate boundary. The remaining strike-slip component of the rifting is accommodated by N-S oriented strike-slip faults, which are known to be capable of producing earthquakes of moment magnitude as high as 6 (Einarsson, 1991; Björnsson et al., 2020). The volcanic systems (Figure 5.1) are from west to east: 1) Reykjanes, 2) Eldvörp-Svartsengi, 3) Fagradalsfjall, 4) Krýsuvík, 5) Brennisteinsfjöll and 6) Hengill. All, except Fagradalsfjall, comprise a known high-temperature (HT) geothermal field (black dashed polygons in Figure 5.1). The HT polygons show the extent of the geothermal fields, according to resistivity values at 1 km depth (Flóvenz et al., 2022, and references therein). Both the Eldvörp-Svartsengi and Reykjanes HT fields host an operating geothermal power plant. It is worth noting that Eldvörp is a subfield of Svartsengi, and as such, Eldvörp is included in the resistivity outline of Svartsengi.

The upper crustal structure of the RP is built of extrusive basaltic rocks with a downward-increasing alteration and a greater proportion of intrusive rocks. The upper crust is roughly 4.5 km thick on the RP (Pálmason, 1971; Flóvenz et al., 1980; Weir et al., 2001). It is believed that intrusive rocks build the lower crust down to Moho, which is located at a depth of around 15 km (Weir et al., 2001). The brittle-ductile transition (BDT) zone, with an estimated temperature of around 600 °C in basaltic rocks (Ágústsson & Flóvenz, 2005; Violay et al., 2012), is typically located at 6-7 km depth beneath the RP and rises up to 3-5 km depth below the HT fields (Blanck et al., 2020; Gudnason et al., 2020; Flóvenz et al., 2022). Crustal thickening along the RP from west to east is observed both by wide-angle reflection seismic (Weir et al., 2001) and local earthquake tomography (Tryggvason et al., 2002).

5.3 Acquisition & data

As a part of IMAGE (Integrated Methods for Advanced Geothermal Exploration; Hersir et al., 2020b), a dense seismic network was installed on and around the RP in

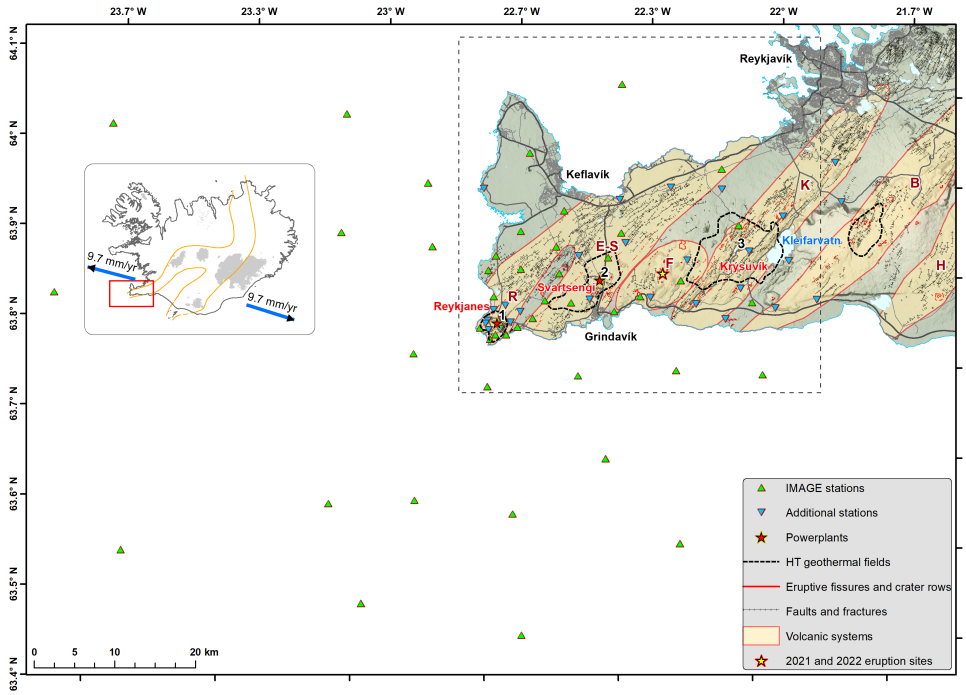

Figure 5.1. *The seismic network and the geological setting of the study area. Green triangles are IMAGE seismic stations (both on- and off-shore). Blue inverted triangles are additional seismic stations from other existing seismic networks in the area. Red and black fault lines denote postglacial volcanic eruptive and opening fissures, respectively; the volcanic systems are shaded light brown and marked with a bold letter, R: Reykjanes, E-S: Eldvörp-Svartsengi, F: Fagradalsfjall, K: Krýsuvík, B: Brennisteinsfjöll, H: Hengill (Sæmundsson & Sigurgeirsson, 2013); black dashed polygons show the extent of the high-temperature geothermal fields on the Peninsula according to resistivity measurements (summarized in Flóvenz et al., 2022) and the geothermal power plants of Svartsengi and Reykjanes are shown with red stars. The approximate location of the 2021 and 2022 Fagradalsfjall eruptions (Pedersen et al., 2022), as well as the 2023 eruption, is shown with a yellow star. The black-dashed rectangle shows the map extent of Figure 5.8. Main roads are in black, and main landmarks referenced in the text are shown on the map. The inset shows volcanic zones of Iceland (orange) with blue arrows indicating the plate spreading rate in Iceland (Sigmundsson et al., 2020). The red rectangle on the inset shows the location of the zoomed-in area.*

2014 (Jousset et al., 2020a; Blanck et al., 2020). It consisted of 30 on-land stations and 24 Ocean Bottom Seismometers (OBSs). In addition to this temporary IMAGE network, data from other existing seismic networks in the area were made available to the project. These were (i) a local monitoring network run by HS Orka/ÍSOR, (ii) REYKJANET (Horálek, 2013) run by the Czech Academy of Science (CAS) in co-operation with ÍSOR on the central and eastern part of the Peninsula, and (iii) permanent stations run by the Icelandic Meteorological Office (IMO) (Icelandic Meteorological Office, 1992; Jakobsdóttir, 2008). Results based on the seismic data

from the 30 onshore stations of the IMAGE network have been published by e.g., Jousset et al. (2016); Verdel et al. (2016); Weemstra et al. (2016); Martins et al. (2020). In this chapter, we use the recordings by all four seismic networks (i.e., blue and green triangles in Figure 5.1), whose combination we refer to as the 'extended IMAGE seismic network'.

The extended IMAGE seismic network sampled the seismic noise field between April 2014 and August 2015 using a total of 83 seismic stations. Weemstra et al. (2016) computed the surface wave responses (i.e., time-averaged cross-correlation functions) from the recorded ambient noise data. However, many of the stations turned out to be subject to timing errors. Consequently, Martins et al. (2020) used a subset of the stations (the ones without the timing errors: 30 onshore seismometers of the IMAGE seismic network) in a two-step linearized ANSWT algorithm. Then, Weemstra et al. (2021) recovered the timing errors for most of the additional stations, subsequently allowing them to also correct the computed cross-correlation functions. Time-averaged cross-correlations associated with four of the 83 stations had to be discarded after all. This was due to an unrecoverable timing error (one station; O20; see Weemstra et al., 2021), and insufficient noise recordings (three stations; VSV, O12, and O05; see Figure 1 of the supplementary materials of Weemstra et al., 2021). The active stations are depicted in Figure 5.1 by green triangles. See Weemstra et al. (2021) for more details regarding seismic instruments and network characteristics. We only used vertical component recordings, because these are best suited for recovering Rayleigh waves; in particular in such a heterogeneous area (e.g., Haney et al., 2012).

Figure 5.2 shows the interferometric responses of the extended IMAGE seismic network for the vertical components of the seismometers. The term interferometric is derived from 'seismic interferometry', which refers to the process of retrieving Green's function estimates from recordings of ambient seismic noise (Wapenaar & Fokkema, 2006). The interferometric responses are the result of time-averaged cross-correlations of the recorded noise between the station couples. For the processing steps applied to the raw (noise) data to retrieve the interferometric responses, we refer to Weemstra et al. (2021). Similar to Weemstra et al. (2021) and Martins et al. (2020), we focus on surface waves in the 0.1-0.5 Hz frequency range, which give the most reliable results.

We retrieve the frequency-dependent phase velocities from the interferometric responses computed and corrected by Weemstra et al. (2021) for each station couple, by calculating and picking the most sensible zero-crossings (e.g., Ekström et al., 2009; Kästle et al., 2016; Lindner et al., 2018). Details are provided in Appendix A.2. The picked phase velocities are then converted to the frequency-dependent phase travel times, which are inverted for shear wave velocities using the one-step transdimensional algorithm (Zhang et al., 2018).

5.4 Interferometric travel times

We extract phase velocity dispersion curves from the interferometric responses (station-station time-averaged cross-correlations; see Figure 5.2). The procedure, algorithm, and criteria are explained and exemplified in Appendix A.2. Figure 5.3a

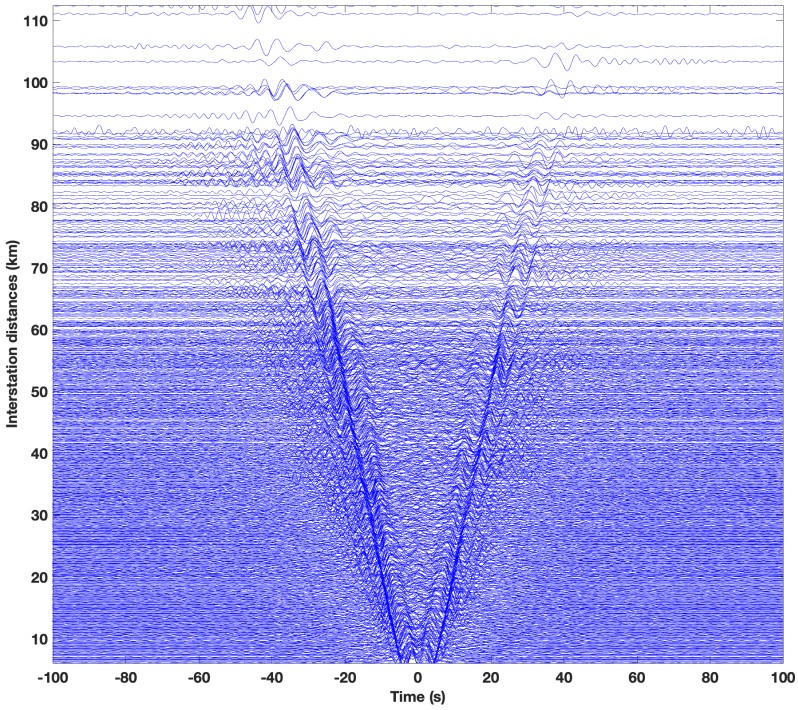

Figure 5.2. *Time-averaged cross-correlations of recordings of ambient seismic noise filtered between 0.1 - 0.5 Hz. Cross-correlations are sorted by station-station distance and individually amplitude normalized. Showing all 79 stations used in the analysis.*

shows all the picked dispersion curves as blue dotted lines. The mean phase velocity, and curves representing two, and three standard deviations (calculated separately at each frequency) are depicted as black, green, and red lines, respectively. After a careful analysis of these dispersion curves, we decided to discard dispersion curves whose velocity deviates more than three standard deviations from the mean. This analysis involved evaluating the spatial distribution of the station couples associated with dispersion curves whose velocity exceeded two standard deviations (following Schippkus et al., 2018). By simply displaying the corresponding rays (with the phase velocity color-coded; Figure 5.4), we find that the discarded station couples are concentrated in a specific area, which coincides with an area traversed by rays that exhibit (anomalously) low shear wave velocities (resulting from an inversion with the retained dispersion curves; i.e., within two standard deviations of the mean). In other words, there is no random pattern in the spatial distribution of the outliers. Also, Figure 5.4 reveals that it is not a single station that is a source of error. This suggests that the discarded dispersion curves are merely representative of the velocity structure in the area. It is therefore that we retain all dispersion curves that are within three standard deviations of the mean. We hence discard a limited number of station-station cross-correlations.

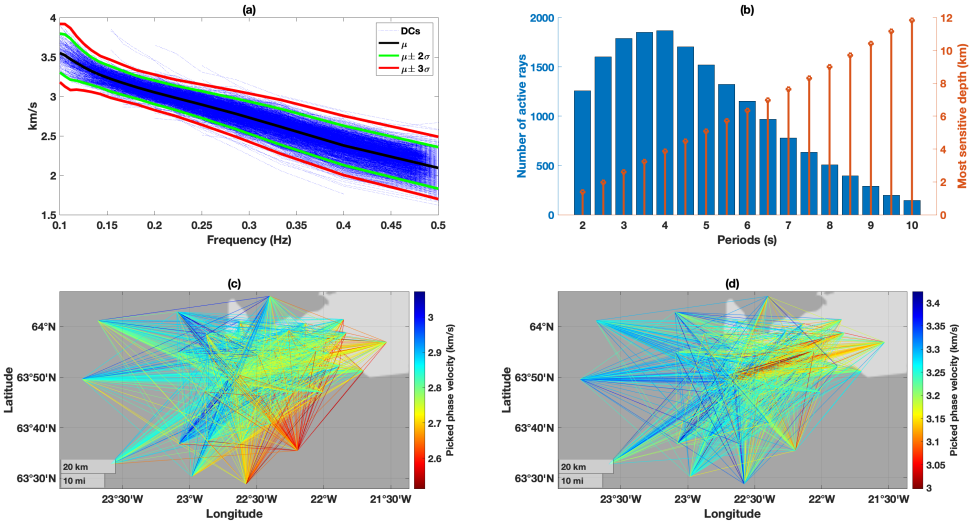

Figure 5.3. *Analysis of picked dispersion curves. (a) All picked dispersion curves (blue) and their mean (μ; black curve). The green curves show $\mu \pm 2\sigma$ and the red curves show $\mu \pm 3\sigma$, where σ is the standard deviation. Data outside of the two red curves are discarded as outliers. (b) The number of active rays per period used in the inversion (blue bars), and the most sensitive depth related to each period (red stem plot). Active rays at periods of (c) 3.5 s and (d) 7 s are depicted as straight rays with the color of each ray indicating the corresponding phase velocity.*

The number of retained phase velocity measurements per frequency is depicted in Figure 5.3b. Note the variation between different frequencies is predominantly to (i) the decreasing SNR with increasing frequency (and hence the picking being terminated by the picking algorithm) and (ii) the increasing number of station couples exceeding the aforementioned condition that the station-station distance needs to exceed one and a half wavelength. The most sensitive depth is also depicted for each period by means of a red stem plot in Figure 5.3b. As a rule of thumb, fundamental-mode Rayleigh waves are most sensitive to the shear wave speed at depths around one-third ($\frac{1}{3}$) of their corresponding wavelength (Fang et al., 2015), where the corresponding wavelength at each period is computed based on the mean dispersion curve (black curve in Figure 5.3a).

Figure 5.3b shows that the retrieved surface waves are most sensitive to structures with a depth of 2-8 km. This implies that (small-scale) structures near the surface (shallower than 2 km) are not expected to be resolved very well. To reveal more details of the near-surface, higher frequencies would need to be included in the inversion. Potential residual timing errors (Weemstra et al., 2021), lower SNRS, and interference of higher modes did not allow us to extract reliable fundamental-mode phase velocities at frequencies beyond 0.5 Hz (let alone potential cross-modal terms obscuring the time-averaged cross-correlations; Halliday & Curtis (2008)).

Figure 5.3c-d shows the eligible station couples as straight rays at two different

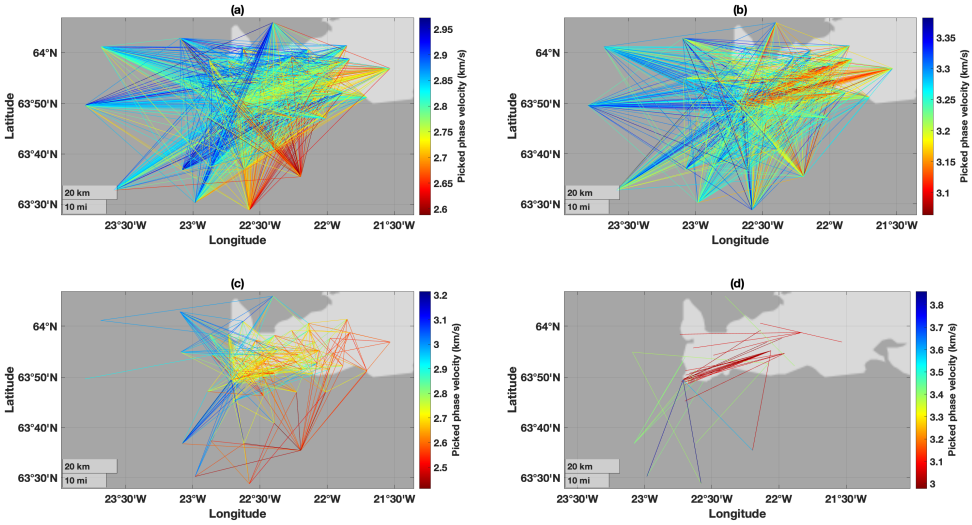

Figure 5.4. *Comparing ray path coverage of the data excluding outliers (a, b) and the ray path coverage of the outliers (c, d) at periods of 3.5 s (a, c) and 6.5 s (b, d). Rays outside of two standard deviations are considered outliers here.*

frequencies. The color of the rays indicates the picked phase velocity for that station couple at that frequency. Note that some structures (in terms of shear wave velocity) can already be inferred from Figure 5.3c-d. For the purpose of the 3D (McMC) tomographic inversion, frequency-dependent phase velocities are converted to frequency-dependent travel times by dividing station-station distances by the phase velocities.

5.5 Surface wave tomography

5.5.1 Two-step modeling and inversion

Once the frequency-dependent travel times are retrieved from all eligible interferometric responses and for all eligible discrete frequencies f_i, the data vector can be built. This data vector contains the frequency-dependent station-station travel times and serves as input to our probabilistic tomographic algorithm in order to recover the shear wave velocity structure of the subsurface. The core of every probabilistic algorithm is the forward function. In our context, this is a function that maps a known shear wave velocity distribution $v_s(x,y,z)$ to the data vector $\mathbf{d}$. Effectively, the forward process can be considered a two-step function:

$$v_s(x,y,z) \xrightarrow{F_1\left[v_s(x,y,z),f_i\right]} c_r(x,y,f_i) \xrightarrow{F_2\left[c_r(x,y,f_i),\mathbf{x}_k,\mathbf{x}_l\right]} \mathbf{d}\left(\mathbf{x}_k,\mathbf{x}_l,f_i\right), \tag{5.1}$$

where $v_s(x,y,z)$ is a known 3D shear wave velocity model as a function of geographical location (x and y) and depth (z), $c_r(x,y,f_i)$ the frequency-dependent phase velocity as a function of x and y, and $\mathbf{d}\left(\mathbf{x}_k,\mathbf{x}_l,f_i\right)$ the data vector containing

the station-station travel times for all station couples and eligible discrete frequencies f_i. Here, $\mathbf{x}_k$ and $\mathbf{x}_l$ are source and receiver locations ($k = l = 1, 2, ..., N$, where N is the number of seismic stations). Similar to $c_r(x, y, f_i)$, these locations depend on x and y only as we ignore topography. The latter is justified by the fact that elevation differences in the area of interest do not exceed a few hundred meters, whereas the shortest wavelengths are in the order of four kilometers (chapter 4). The data vector $\mathbf{d}(\mathbf{x}_k, \mathbf{x}_l, f_i)$ contains the frequency-dependent phase travel times depicted in Figure 5.3. It is useful to note that $v_s(x, y, z)$ is often also referred to as a model vector $\mathbf{m}$ (Bodin & Sambridge, 2009). Here, we should add that the compressional wave velocity $v_p(x, y, z)$ is assumed to be a linear function of $v_s(x, y, z)$ according to $v_p = 1.78 v_s$ (Allen et al., 2002) and that the mass density $\rho(x, y, z)$ is assumed to be related to the latter according to $\rho = 2.35 + 0.036(v_p - 3)^2$, where v_p and v_s are in km/s and ρ in g/cm^3 (Kurita, 1973; Zhang et al., 2020).

The function F_1 is the dispersion curve modeling algorithm (e.g., the modal approximation method of Herrmann, 2013), whereas F_2 uses the fast marching method to solve the 2D Eikonal equation (e.g., Rawlinson & Sambridge, 2004). This two-step forward function is the standard way to compute surface waves' frequency-dependent phase or group travel times. Similarly, a two-step process is commonly used to recover shear wave velocity structure from frequency-dependent travel times:

$$\mathbf{d}(\mathbf{x}_k, \mathbf{x}_l, f_i) \xrightarrow{F_2^{-1}\left[\mathbf{d}(\mathbf{x}_k, \mathbf{x}_l, f_i)\right]} c_r(x, y, f_i) \xrightarrow{F_1^{-1}\left[c_r(x, y, f_i)\right]} v_s(x, y, z). \tag{5.2}$$

First, a 2D phase velocity map is recovered from the inversion of travel times at each frequency, F_2^{-1}, (for different inversion methods see Rawlinson et al., 2003; Yao et al., 2006; Saygin & Kennett, 2012; Bodin et al., 2012; Cabrera-Pérez et al., 2021). Then, the phase velocity maps are used together in a second inversion step, F_1^{-1}, to recover the shear wave velocity structure (e.g., Yao et al., 2008; Haney & Tsai, 2015; Lehujeur et al., 2021). The two-step surface wave forward and inverse modeling are illustrated in Figure 5.5(a-e) using a synthetic block model.

5.5.2 One-step transdimensional approach

The two-step inversion approach suffers from two issues. First, the initial 2D inversion introduces (unknown) errors in the subsequent 1D inversions. This is because usually only the mean and the standard deviation serve as input to the second step of the inversion. That is, implicitly, a Gaussian distribution is assumed. Most likely, however, the posterior distribution associated with this first step is non-Gaussian, as such introducing the (unknown) errors. Second, as the subsequent step involves many independent 1D inversions, it fails to honor the lateral correlation of the shear wave velocity in the subsurface. To improve the lateral correlation in the second step, Lehujeur et al. (2021) suggested inverting all the local dispersion curves simultaneously using a linearized 3D inversion algorithm. In a similar vein, Fang et al. (2015) combined the two inversion problems into one. They proposed a one-step linearized 3D inversion algorithm to recover the 3D shear wave velocity directly from the frequency-dependent phase or group travel times. Recently, Zhang

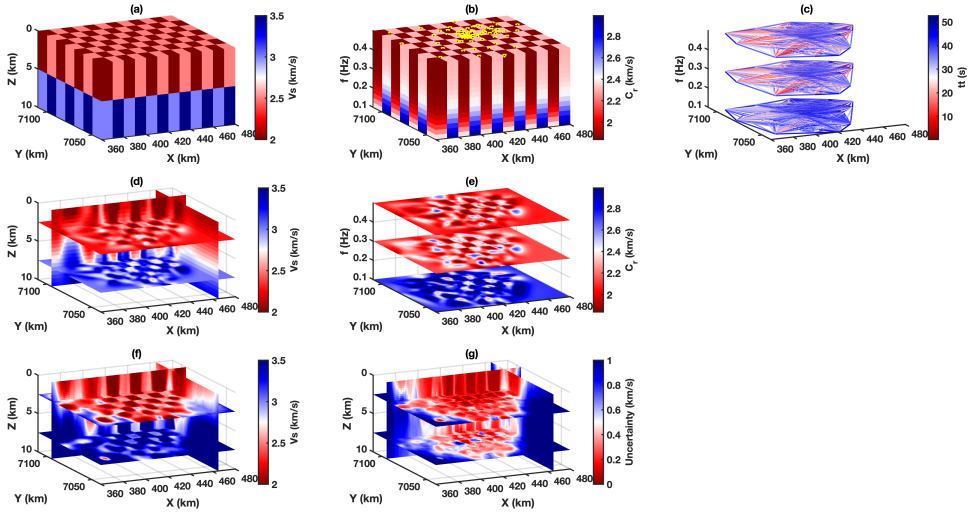

Figure 5.5. *Surface wave modeling and inversion applied to a synthetic 3D block model considering a rather non-uniform spatial sampling of seismic noise field, namely that of the Reykjanes seismic array. (a) A 3D synthetic shear wave velocity block model ($v_s(x,y,z)$). (b) Frequency-dependent Rayleigh wave phase velocity ($c_r(x,y,f)$) computed using the modal approximation method ($F_1\left[v_s(x,y,z),f\right]$). Station locations (the $\mathbf{x}_k$) are depicted as yellow triangles. (c) Frequency-dependent phase travel times ($\mathbf{d}(\mathbf{x}_k,\mathbf{x}_l,f_i)$) computed using the fast marching method ($F_2\left[c_r(x,y,f),\mathbf{x}_k,\mathbf{x}_l\right]$) at three different discrete frequencies. (e) 2D phase velocity maps at three discrete frequencies recovered from (c) using a 2D least-squares inversion algorithm (the first step of the inversion, F_2^{-1}). (d) 3D shear wave velocity model recovered from (e) using a 1D dispersion curve inversion algorithm (the second step of the inversion, F_1^{-1}). (f) Recovered shear wave velocity using the 3D one-step transdimensional inversion algorithm ($F^{-1}\left[\mathbf{d}(\mathbf{x}_k,\mathbf{x}_l,f_i)+\mathbf{noise}\right]$). (g) The uncertainty corresponding to the recovered shear wave velocity in (f).*

et al. (2018) proposed another one-step 3D surface wave tomography method using a reversible jump Markov chain Monte Carlo (rjMcMC) algorithm, which we refer to as the one-step transdimensional method. It recovers the shear wave velocity directly from the frequency-dependent travel times.

$$\mathbf{d}(\mathbf{x}_k,\mathbf{x}_l,f_i) \xrightarrow{F^{-1}\left[\mathbf{d}(\mathbf{x}_k,\mathbf{x}_l,f_i)\right]} v_s\left(x,y,z\right), \tag{5.3}$$

where F^{-1} represents the one-step transdimensional probabilistic algorithm (i.e., the rjMcMC approach). Importantly, this one-step transdimensional algorithm results in an estimate of the posterior probability density. This implies that it allows us to quantify the uncertainty. In this case, we use the pointwise standard deviation of the ensemble of models for this purpose. This is the standard deviation with respect to the pointwise average of the same ensemble (i.e., at each position (x,y,z), standard deviation and average of the shear wave velocities are computed using all retained models). The pointwise average has been shown to closely resemble the true velocity structure (Bodin & Sambridge, 2009; Zhang et al., 2018). This one-step algorithm is

illustrated in Figure 5.5.

One-step transdimensional tomography involves the use of the reversible jump Markov chain Monte Carlo method which deploys a variable model geometry, a variable number of cells partitioning the model space, and an unknown noise level in the input data. As such, the algorithm avoids the selection of fixed parameterizations and any regularization in the inversion process. This makes the algorithm less dependent on (often) subjective choices. Like many McMC algorithms, the one-step transdimensional algorithm starts with a random initial model, which is parameterized by Voronoi polyhedra with a randomly chosen number of Voronoi cells. The shear wave velocity is also assigned to each Voronoi cell randomly. The shape or geometry of each Voronoi cell is then defined by the surrounding cells. We refer to Zhang et al. (2018) and chapter 4 for a detailed description of the 3D Voronoi partitioning.

The next step of the algorithm (which yields the second sample of the Markov chain) is to perturb the initial velocity model using one of the five possible perturbation steps, including a move step, a velocity update step, a birth step, a death step, and a noise update step. After the perturbation, we compute the shear wave velocity on a fine rectangular grid so that the velocity can be used in the forward function to calculate the frequency-dependent travel times. For a detailed description of the workflow, we refer to chapter 4. These travel times are then compared with the measured surface wave phase travel times. The new velocity model is accepted or rejected based on the acceptance probability (see Bodin et al., 2009; Zhang et al., 2018, for more details). Continuously sampling the model space (i.e., proposing new $v_s(x, y, z)$), we asymptotically approach the posterior probability distribution of the model parameters. The pointwise average and standard deviation of these samples are subsequently computed, yielding the most probable velocity model and associated uncertainty, respectively. In order to remove the effects of the initial velocity model on the posterior distribution, an initial set of samples is discarded (usually referred to as the 'burn-in period'). In addition, to ensure the collected samples are uncorrelated, samples are retained at only a certain level (e.g., every 200 iterations); this process is usually referred to as 'thinning'.

5.5.3 Application to the extended IMAGE data

Prior to our probabilistic inversion, we recovered an average 1D shear wave velocity profile of the study area using a 1D least-squares inversion algorithm (Xia et al., 1999, see also chapter 2 of this thesis). We used the mean phase velocities (the black curve in Figure 5.3a) in this 1D least-squares iterative algorithm. See section 2.3 for more information about the nonlinear least-squares inversion applied to the average dispersion curve. We used a 1D velocity profile based on Tryggvason et al. (2002) as the initial model for this inversion. The recovered shear wave velocity profile is depicted in Figure 5.6a. The sensitivity kernels at different periods are also depicted in 5.6b-c. It shows that the sensitivity decreases significantly below 15 km depth. The recovered velocity is constant below 15 km depth, which is the most likely depth of the Moho discontinuity (e.g., Weir et al., 2001; Jacoby et al., 2007). To include this discontinuity, we sampled the subsurface down to 20 km depth (i.e., we populated it

with Voronoi cells down to this depth). The half space below 20 km depth is assigned the velocity of the bottom layer (i.e., the velocity of the deepest Voronoi at each grid point), meaning that it is also laterally variable. Based on several studies focusing on the study area (e.g., Weir et al., 2001; Du et al., 2002; Foulger et al., 2003), the upper crustal shear wave velocity can reach 3.7 km/s and the lower crustal shear wave velocity can reach 4.2 km/s. Consequently, we considered a uniform prior ranging from 1.5 to 4.5 km/s for the shear wave velocity. The upper bound of 4.5 km/s was chosen based on the fact that the shear wave velocity in the mantle has been shown to not exceed 4.5 km/s below the RP (e.g., Du et al., 2002; Foulger et al., 2003).

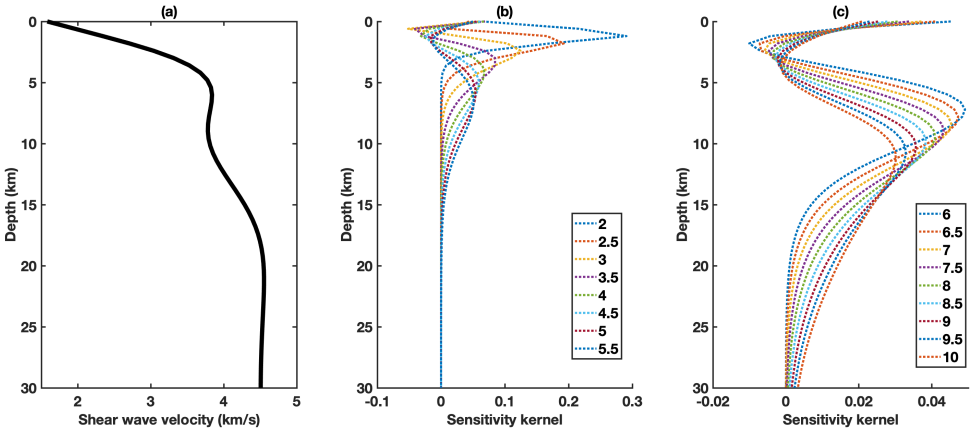

Figure 5.6. *Shear wave velocity profile obtained from a 1D least-squares inversion of the mean phase velocities (the black curve in Figure 5.3a). The initial velocity profile is chosen based on Tryggvason et al. (2002). (b-c) The sensitivity kernels at different periods are computed based on the velocity model in (a) using the package developed by Wu et al. (2019).*

Table 5.1 lists the modeling and inversion parameters used in the application of the one-step transdimensional inversion to the surface wave data retrieved from the RP ambient noise data. An arbitrary first model (the 'initial model') was chosen, meaning that the number of Voronoi cells, their positions, and their velocities were chosen randomly. We used a coarser grid to compute the frequency-dependent travel times (forward modeling) while sampling the model space, and a finer grid for calculating the post-burn-in pointwise average and standard deviation of the sampled models.

Gaussian proposal (probability) distributions are used for drawing new velocity values and new nuclei. The proposal width of these Gaussian distributions affects the chance of a proposed model being accepted and consequently the transdimensional algorithm's convergence rate. Too narrow or too wide proposal distributions both result in slower convergence rates. A narrow proposal distribution increases the acceptance ratio but explores the parameter space more locally. By contrast, a wide proposal distribution explores the space more widely but leads to lower acceptance

Table 5.1. *Modeling and sampling parameters used in the probabilistic one-step inversion of the interferometric travel times.*

Modeling and sampling Parameters	Value
Model dimension (km)	120 (east-west)× 70 (north-south) × 20
Number of grid points in McMC sampling	121 × 71 × 41
Number of grid points for calculating post-burn-in pointwise average	241 × 141 × 81
Valid range of shear wave velocity (km/s)	1.5–4.5
Valid range of noise hyper parameter a	10^{-5}–1
Valid range of noise hyperparameter b	0–2
Proposal width for a move step. Md is the model dimension.	$0.07 * Md$
Velocity proposal width (km/s)	0.3
Proposal width for a	10^{-3}
Proposal width for b	10^{-2}
Thinning level	200
Ray path update step	250
Number of sampling chains	20
Number of samples per chain	3×10^6
Number of burn-in samples per chain	1×10^6

ratios and as such also to a slower convergence rate (see chapter 4 of this thesis). According to previous research, an effective proposal width results in a 25%–50% acceptance rate (Bodin et al., 2009; Gelman et al., 1996). The width of the proposal distributions listed in Table 5.1 are determined in a previous, purely synthetic study, but using the same station configuration (chapter 4 of this thesis). This also applies to the proposal widths of the noise hyperparameters (detailed in the paragraph below).

We assumed a (non-informative) uniform prior probability distribution for the model parameters. What we refer to as the 'valid range' in Table 5.1 defines, for each parameter, the range for which the prior probability is non-zero. To reduce computational costs, while still preserving the nonlinearity of the problem we updated ray paths every 250 iterations. Thinning was achieved by retaining every 200th model. The noise was assumed to be uncorrelated and normally distributed, with the variance being a frequency-dependent, linear function of travel time, i.e., with d_i representing the i^{th} element of the data vector $\mathbf{d}$ (and hence travel time), $\sigma_i = ad_i + b$. This linear relationship between travel time and travel time error is usually assumed (e.g., Bodin et al., 2012; Galetti et al., 2017; Zhang et al., 2020). The a and b are assumed to be unknown and therefore also estimated by the Markov chain process (see, e.g., Bodin et al., 2012).

To sufficiently sample the posterior distribution, we used 20 independent McMC chains, each sampling 3×10^6 samples from the posterior probability density of model parameters given the frequency-dependent travel times. Figure 5.7 shows some statistical measures of these 20 McMC chains. Different colors represent different sampling chains. Noise hyper-parameters are presented for a single frequency as

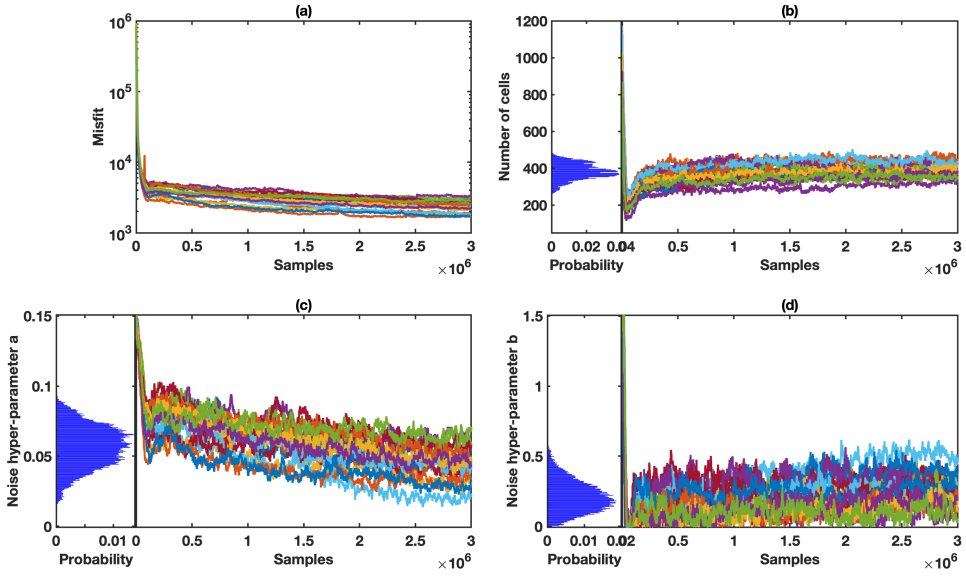

Figure 5.7. *Chain statistics of the 20 McMC chains. Each color represents a different chain. (a) Misfit, (b) number of cells, (c) the noise hyper-parameter a, and (d) the noise hyper-parameter b. Histograms of the posterior distribution for the retained models for each parameter are shown as insets on the left side of each panel in (b-d). These graphs are used to assess the convergence of the sampler.*

they vary by frequency. We observe that the misfit, the number of cells, and the noise hyper-parameters stabilize after generating approximately 0.5×10^6 samples. This suggests that the Markov chain has mixed sufficiently well and that the posterior probability density is properly sampled. To be on the safe side, however, we discarded the first million samples (usually referred to as the burn-in phase). The rest of the samples are retained at every 200th iteration. Consequently, combined the 20 chains lead to a total of 200,000 posterior samples to be retained. These are subsequently used to compute pointwise mean and variance.

5.6 Tomographic results

We present the pointwise average of the retained post-burn-in samples as our final tomographic solution and the pointwise standard deviation of retained samples as the uncertainty related to the solution model. Several horizontal and vertical slices of the posterior mean are presented in Figures 5.8-5.12. Only the most densely sampled region of the study area is presented, which has lower uncertainties; an area of approximately 38 km by 45 km (see the dashed black box in Figure 5.1 or Figure A.2). The model uncertainties are presented in Appendix A.3. The uncertainty for the whole area covered by the seismic stations (120 km by 70 km) is presented in Figure A.2. Figures A.3-A.6 are the posterior standard deviations (i.e., uncertainties)

associated with the posterior mean presented in Figures 5.9-5.12, respectively. As expected, the areas with more seismic stations show lower uncertainty due to the higher number of station-station paths in these areas. We have selected the most reliable area based on these uncertainties.

Figure 5.8 shows the pointwise mean of the shear wave velocity beneath the RP at six different depths (0.5, 3, 4, 6, 8, and 10 km). The coastline and the three known HT fields of Reykjanes, Eldvörp-Svartsengi, and Krýsuvík (black dashed polygons in Figure 5.1) are included in these figures for reference. It should be noted that the HT polygons show the extent of the geothermal fields, according to the resistivity values (the resistive core) at 1 km depth (as summarized in Flóvenz et al., 2022). Significant velocity anomalies are observable in Figure 5.8. At shallow depths (0.5 km; Figure 5.8a) the Eldvörp-Svartsengi and Krýsuvík HT geothermal fields show high-velocity anomalies, the same applies to the Fagradalsfjall volcanic system. The anomalies invert at depths of around 2 km. At a depth of 3-6 km (Figure 5.8b-d) the known HT fields appear as low-velocity anomalies, most pronounced at Eldvörp-Svartsengi, Krýsuvík and in the vicinity of the Fagradalsfjall's recent eruption site (yellow star in Figure 5.8). The low-velocity at Reykjanes is most pronounced from 6 to 8 km depth (Figure 5.8d-e). A striking NW-SE trending low-velocity anomaly, almost perpendicular to the Krýsuvík volcanic system, is apparent in Figure 5.8c-f. At the depth of 4 km (Figure 5.8c) the low-velocity anomalies are small and mainly limited to the HT fields of Eldvörp-Svartsengi and Krýsuvík. At 8 km depth (Figure 5.8e), however, the area is dominated by low shear wave velocities, where the NW-SE Krýsuvík anomaly is the strongest. A weak trend along the plate boundary (N70°E) is observable in both the high-velocity of Figure 5.8a and low-velocity of Figure 5.8b.

Differences are observed in the shape and size of the low-velocity patches with respect to the known HT fields constrained by resistivity data at 1 km depth (black dashed lines in Figure 5.8; Flóvenz et al., 2022). At depths of 6-8 km below the Reykjanes HT field (Figure 5.8d-e), the low-velocity anomaly is smaller than the HT field and placed slightly north of it. Within the Eldvörp-Svartsengi HT field, the low-velocity anomaly is located right below the corresponding HT field at a depth of 4 km (Figure 5.8c) with a comparable size. However, the size of the low-velocity anomaly is greater than the corresponding HT field at the depth of 6 km and stretching to the north. The Krýsuvík low-velocity anomaly is the most prominent, i.e., both the largest and the strongest anomaly we observe on the RP, while it is slightly smaller in size than the corresponding HT field. At 4-10 km depth it stretches from the center of the HT field towards the southeast, almost perpendicular to the volcanic system (Figure 5.8c-e).

In the vicinity of the Fagradalsfjall 2021-2023 eruption sites (yellow star in Figure 5.8), we observe low-velocity anomalies at 4-6 km depth at the boundaries of the Eldvörp-Svartsengi and Fagradalsfjall volcanic systems. The Fagradalsfjall anomalies, however, are all fairly weak. Finally, two significant low-velocity anomalies are observed at 10 km depth (Figure 5.8f) indicated by black rectangles. Due to the low density of ray paths at these two locations (see Figure 5.3c-d) we refrain from interpreting these anomalies. Furthermore, the uncertainties of both anomalies are

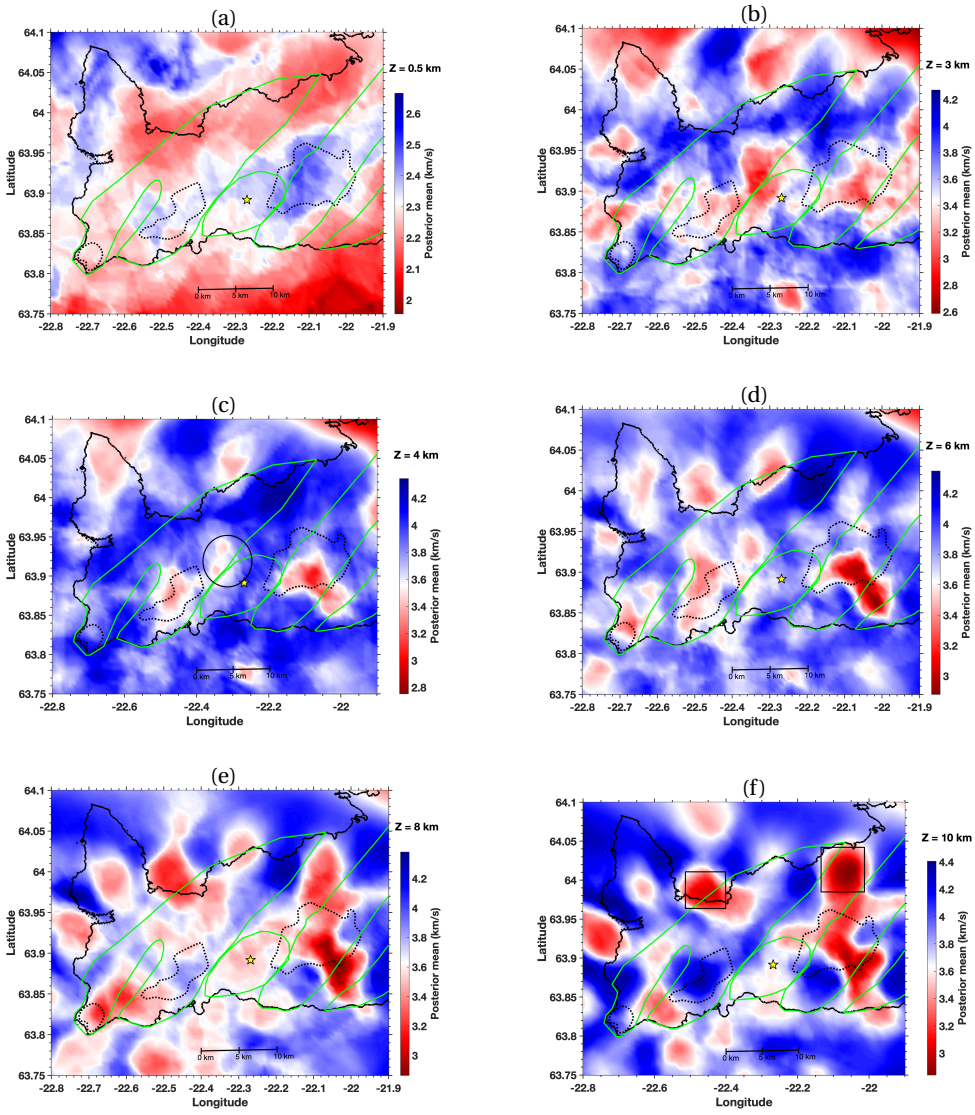

Figure 5.8. *Pointwise averaged shear wave velocities (from the retained post-burn-in samples) at six different depths: (a) 0.5 km, (b) 3 km, (c) 4 km, (d) 6 km, (e) 8 km, and (f) 10 km, of the area with the highest resolution and the lowest uncertainties (38 km by 45 km). The green polygons show the outlines of the volcanic systems. The dashed black polygons are the known high-temperature geothermal fields. The black circle in (c) indicates the low-velocity observed at the boundaries of the Eldvörp-Svartsengi and Fagradalsfjall volcanic systems. The yellow star inside the Fagradalsfjall volcanic system is the approximate location of the 2021, 2022, and 2023 eruptions. Note that the color scale is not the same on all slices. Uncertainties (posterior standard deviation associated with the posterior mean presented) are displayed in Figure A.2.*

very high in Figure A.2e-f and Figure A.4d.

To better visualize the velocity structure of the RP focusing on the HT geothermal fields, we present the recovered 3D velocity structure in three differently oriented vertical cross-sections centering at the Reykjanes, Eldvörp-Svartsengi and Krýsuvík HT fields, and the Fagradalsfjall eruption site, respectively, Figures 5.9-5.11. In each figure, the first vertical cross-section is oriented along an east-west profile (B-B'), the second along a profile striking N70°E (C-C'), approximately along the plate boundary, and the third cross-section is along a profile striking N20°W (D-D'), approximately perpendicular to the plate boundary. We observe, in general, across the whole survey area, that the shear wave velocity increases with depth from about 2 km/s at the surface to approximately 3.8 km/s at a depth of 5 km. A decrease in shear wave velocity with depth (due to a large number of low-velocity anomalies) is generally observed across the RP between depths of 4 and 8 km, but notably shallowest under the HT fields.

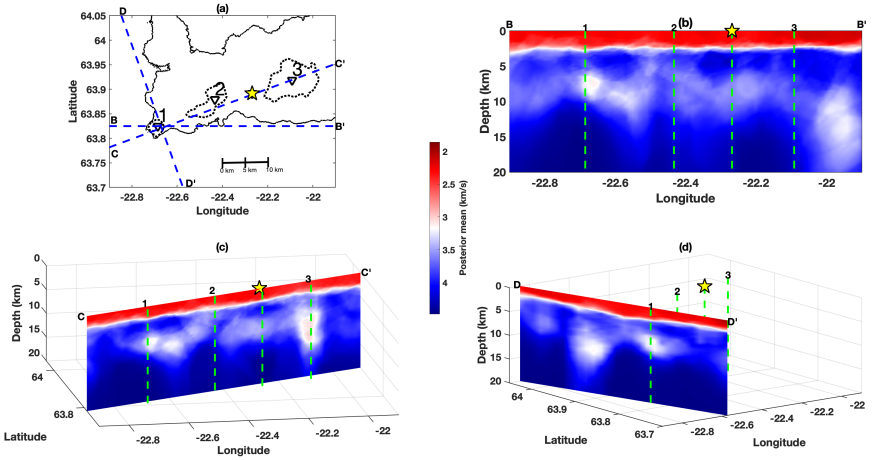

Figure 5.9. *Vertical cross-sections, centered at the location of the Reykjanes HT geothermal field, of the pointwise averaged shear wave velocities of the retained post-burn-in samples. (a) Map of the area showing the location of the three reference points, and the extent of the known high-temperature geothermal fields of Reykjanes, Svartsengi, and Krýsuvík (dashed black polygons), blue lines show the locations of the vertical cross-sections of the shear wave velocities along an east-west profile (b), N70°E oriented profile (c), and N20°W oriented profile (d). The yellow star is the approximate location of the 2021, 2022, and 2023 eruptions. Uncertainties (posterior standard deviation associated with the posterior mean presented) are displayed in Figure A.3.*

Figures 5.9b-d present the vertical cross-sections centered at the location of the Reykjanes power plant and hence centered at the Reykjanes HT geothermal field (labeled '1' in map view and on the cross-sections), The B-B' cross-section (Figure 5.9b) lies across the Reykjanes HT field and along the coast to the east. A low-velocity patch is observed directly below the Reykjanes HT field. Between 6 and 8 km depths, it extends laterally towards the east, passing the area below the

Eldvörp-Svartsengi HT field, the Fagradalsfjall volcanic system, and all the way east of the Krýsuvík HT field. The C-C' cross-section in Figure 5.9c transects all four volcanic systems of Reykjanes, Eldvörp-Svartsengi, Fagradalsfjall, and Krýsuvík along the plate boundary. It shows a similar low-velocity image as Figure 5.9b, but here the Reykjanes anomaly is clearer, and also the connection to Eldvörp-Svartsengi to the NE. A large low-velocity zone is visible below the Krýsuvík HT field (labeled '3'). Slightly lower velocities are also observed at 7-10 km depth at a longitude of -22.3°W, located between '2' and '3', where the Fagradalsfjall volcanic system lies. This anomaly seems weakly connected to the Krýsuvík low-velocity anomaly (Figure 5.9c). The low-velocities seem to highlight a more or less continuous zone along the plate boundary at ca. 6-10 km depth. The low-velocity patch below the Reykjanes HT field is also observable in Figure 5.9d, cross-section D-D', down to 8 km depth. Another significant low-velocity anomaly at 6-10 km depth can be seen to the north-northwest of the Reykjanes HT field in Figure 5.9b.

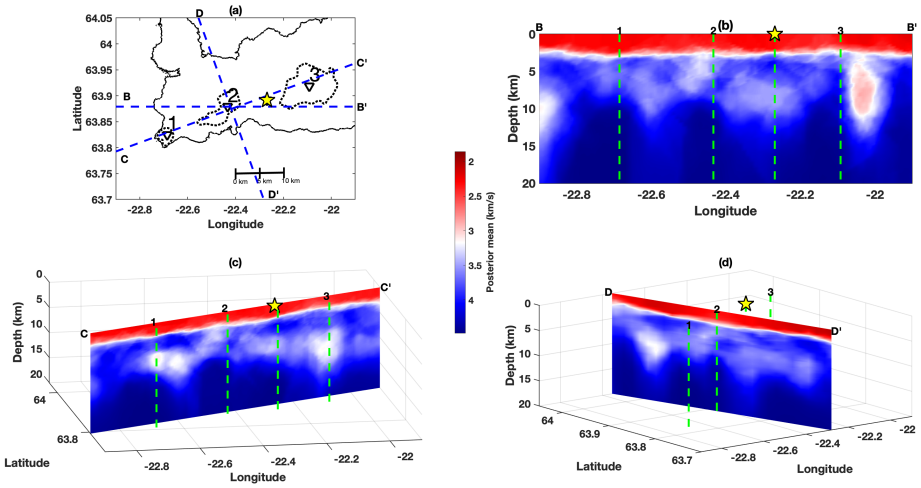

Figure 5.10. *As Figure 5.9, but centered at the location of the Eldvörp-Svartsengi HT geothermal field. Uncertainties are displayed in Figure A.4.*

Figure 5.10 presents the vertical cross-sections centered at the location of the Svartsengi power plant, labeled '2'. A low-velocity anomaly is observable below the Eldvörp-Svartsengi HT field on cross-section B-B'. This low-velocity zone appears at around 3 km depth and extends to approximately 7 km depth, dipping from E to W with an approximate lateral extent of 8 to 10 km (Figure 5.10b). This low-velocity patch is visible in Figure 5.10c as well. A horizontal low-velocity anomaly at around 6 km depth in Figure 5.10c is observed possibly linking the Reykjanes and Eldvörp-Svartsengi HT fields at depth. Below the Krýsuvík HT field, the pronounced low-velocity column (see Figure 5.9c) is again visible in Figures 5.10b-c. Below the Fagradalsfjall volcanic system, the low-velocity patch observed at around 8 km depth in Figure 5.9c is also visible in Figures 5.10b-c.

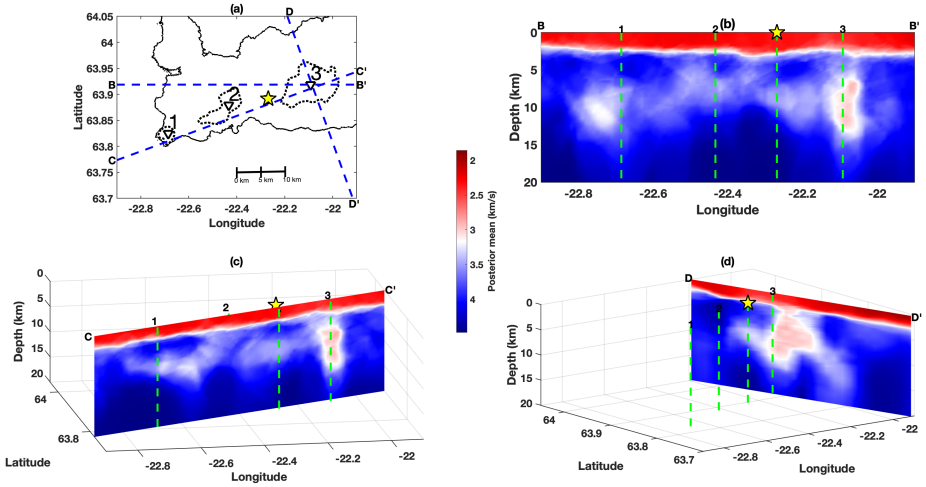

Figure 5.11. *As Figure 5.9, but centered at the location of the Krýsuvík HT geothermal field. Uncertainties are displayed in Figure A.5.*

Figure 5.11 presents the vertical cross-sections centered at the Krýsuvík HT field (labeled '3'). A large and prominent low-velocity column is clearly observable below the Krýsuvík HT field at roughly 5-12 km depth in all three vertical cross-sections. Figure 5.11d also shows clearly that the pronounced low-velocity anomaly is extending to the southeast and it is the shallowest of all three, reaching up to about 3 km depth, just southeast of '3'. Due to the 2021-2023 volcano-tectonic unrest on the RP, we also present the vertical cross-sections centered at the location of the recent eruption site in Figure 5.12. It should however be noted that the data used in this study are from 2014-2015.

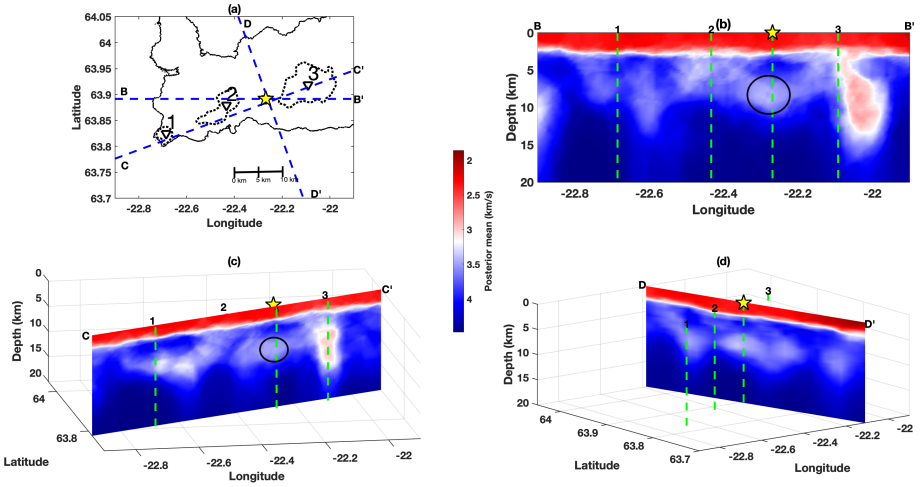

Figure 5.12. *As Figure 5.9, but centered at the location of the 2021-2023 eruptions site, within the Fagradalsfjall volcanic system. The yellow star is the approximate location of the 2021, 2022, and 2023 eruptions. The black circles in (b-c) indicate the low-velocity observed below the Fagradalsfjall volcanic system. Uncertainties are displayed in Figure A.6.*

To summarise the most important observations, which will be discussed in the next section:

- In general, from the top (Earth's surface) to the bottom (20 km) of the model, the pointwise average of the sampled shear wave velocity increases, but a decrease in velocity is observed within the depth range of 5 to 8 km.
- Close to the surface within and around the known HT geothermal fields, and somewhat NE-SW along the fissure swarms of the RP, relatively high-velocity patches are observed (Figure 5.8a). At depths greater than 3 km, these higher velocities invert (decrease) to relatively low-velocities (in comparison to shear wave velocities in the same horizontal plane).
- Low-velocities are dominant at depths of 6-8 km, but beneath the HT fields, the low-velocities rise up to 3-4 km depth.
- The size and location of these low-velocity bodies coincide overall fairly well with the extent of the HT geothermal fields derived from electrical resistivity studies, despite deviating somewhat.
- A large and strong low-velocity anomaly is observed below the Krýsuvík HT geothermal field, and extends down to around 15 km depth. This pronounced anomaly stretches from the center of the HT field towards the southeast from a depth of 3 km.
- A low-velocity zone is observed at the northwest border of the Fagradalsfjall volcanic system, at a depth of approximately 4-5 km (Figure 5.8c-d). This

low-velocity slopes down to below the recent eruption site at a depth of 7-9 km (Figure 5.12b-d).

- The shear wave velocity below 15 km depth is almost constant with velocities above 4.2 km/s.

5.7 Discussion

In this section, we provide an interpretation of the pointwise averaged shear wave velocities, qualitatively comparing our final model to other geophysical models, and relating it to the existing geological and geophysical literature and interpretation of the RP. Prior to interpreting the observed shear wave velocities, we consider our models' resolution. Resolution tests using synthetic surface wave responses for the RP and the extended IMAGE seismic network station configuration are presented in chapter 4. In that study, we concluded that for the area of interest (black box in Figure 5.1), the transdimensional algorithm is able to recover quite well a 3D velocity model with blocks of 5 by 5 by 2.5 km (in the north, east, and depth directions, respectively). This suggests that structures of that size (or larger) are well resolved.

5.7.1 High-velocity anomalies

The first observation is the relatively high shear wave velocities close to the surface around the location of the known HT geothermal fields (compared to the surrounding areas; Figure 5.8a). This is in particular valid for Eldvörp-Svartsengi and Krýsuvík, where the anomalies also show a weak trend along the fissure swarms; whereas the anomaly in Reykjanes is very small. It is worth noting that the Reykjanes HT field is much smaller in areal extent than the Eldvörp-Svartsengi and Krýsuvík HT fields based on the resistivity studies. Our findings are consistent with a high-velocity zone found by Adelinet et al. (2011) around the Krýsuvík HT field at a depth of 2 km. Similarly, Jousset et al. (2016) observed high shear wave velocities for the Reykjanes and Eldvörp-Svartsengi HT fields at a depth of 200 m. An explanation for the relatively high-velocity zones near the surface at the location of the HT geothermal fields could be the intense mineral alteration (caused by higher temperatures) in the uppermost 1-2 km, filling up pores and fractures which in turn increases the seismic velocities in those areas near the surface.

5.7.2 Brittle-ductile transition

The second notable observation is the horizontally extended velocity decrease between 5 and 8 km depth dominating the whole area (Figures 5.9-5.12b-c), in comparison to higher velocities at greater depth. This low-velocity anomaly domes up to a depth of 3 km below all the known HT fields. This kind of low shear wave velocity anomaly is commonly observed within volcanic systems (Takei, 2017), and commonly attributed to partial melt (e.g., Lees, 2007). However, some geochemical observations (e.g., McKenzie, 2000) suggest that the melt fraction is too small in an area with partial melt (~0.1%) to have the shear wave velocity drop significantly (Priestley & McKenzie, 2006; Takei, 2017). Additionally, the temperature at the

location of low-velocity anomalies within the volcanic systems is sometimes lower than the solidus temperature of the rocks. For example, the solidus temperature of basalt (i.e., the main composition of rocks in RP's crust) exceeds 1000 °C (Chen et al., 2017), whereas the temperature is estimated to be around 600°C at a depth of 6-7 km on the RP (Violay et al., 2012; Bali et al., 2020), representing the brittle-ductile transition (BDT) zone, evidenced by the IDDP-2 drilling.

Recent studies suggest that these low shear wave velocity anomalies are more likely due to the combination of high temperature and an-elasticity (Priestley & McKenzie, 2006, 2013; Karato, 2014; Takei, 2017). An-elasticity makes the effect of increasing temperature significant by decreasing the shear wave velocity rather abruptly (Takei, 2017). In our case, the an-elasticity is likely associated with the known BDT zone, between the upper crust and the lower crust, which is estimated to be at around 6-7 km depth on the RP, doming up to 3-5 km depth below the HT geothermal fields (Blanck et al., 2020; Gudnason et al., 2020; Flóvenz et al., 2022). The BDT depth range coincides well with our observation of a general velocity decrease within the depth range of 5 to 8 km, suggesting that an-elasticity and elevated temperatures also play a significant role in the shallow onset of the velocity-decrease at around 3 km depth below the HT fields.

5.7.3 Magma accumulation

Recently, Caracciolo et al. (2023) presented an interesting conceptual model for the magma plumbing architecture on the RP, based on petrochemical analysis of the lava flows of the 800-1240 AD Fires on the Peninsula. This was the last volcano-tectonic episode prior to the 2021-2023 Fagradalsfjall episode, with eruptions within all the volcanic systems of the RP, except Fagradalsfjall. Caracciolo et al. (2023) find that during the 800-1240 AD Fires, magma accumulation occurred at around 7-10 km depth below the Reykjanes, Eldvörp-Svartsengi, and Krýsuvík systems, a controlling factor for volcanic eruptions within these systems. However, deeper plumbing structure applies to the Fagradalsfjall system, where petrochemical analysis of the 2021 magma shows that it was tapped directly from near-Moho reservoirs at 15-20 km depth, with little or no stalling in the uppermost crust prior to eruptions (Halldórsson et al., 2022).

The depth extent of where the low-velocity anomalies are intensified in our model, at a depth of 7-10 km between the Reykjanes and Eldvörp-Svartsengi HT fields and at a depth of 5-12 km depth below the Krýsuvík HT field (vertical cross sections along the plate boundary in Figures 5.9-5.11c), is in good agreement with the magma plumping architecture suggested by Caracciolo et al. (2023).

5.7.4 HT geothermal fields

Krýsuvík volcanic system

The largest and most significant seismic feature we observe is related to the Krýsuvík volcanic system. Krýsuvík hosts an unharvested HT geothermal system, which heat source is considered to be dyke intrusions (Arnórsson et al., 1976; Arnórsson, 1987; Hersir et al., 2020a), perhaps also indicated by an indicative gravity high in the

area (Guðmundsson et al., 2004). The relatively wide vertical low-velocity column we observe seems to be centered 4 km west of Lake Kleifarvatn (Figure 5.1). This coincides well with the results of a recent electrical resistivity study in the area, which indicated a large conductive body at approximately 2 km depth in the same area (Hersir et al., 2020a). The center of this conductive body is labeled '3' in Figures 5.9 - 5.11, where it is also evident that the Krýsuvík HT field is the largest out of the three known HT fields, as determined by both resistivity studies and ANSWT.

The conductive body of Hersir et al. (2020a) is located near the central part of the Krýsuvík geothermal area, where its body concurs horizontally with the source of inflation and deflation observed in Krýsuvík since 2009 with both GPS and InSAR measurements, modeled at 4-5 km depth (Michalczewska et al., 2012; Flóvenz et al., 2022). Adelinet et al. (2011) suggest the presence of a gaseous or supercritical fluid at around 6 km depth, based on the analysis of P- and S-wave tomographic results. Hobé et al. (2021) also predict a large supercritical reservoir below 5 km depth.

The pronounced low-velocity anomaly extends from the Krýsuvík HT area to the southeast almost perpendicular to the Krýsuvík fissure swarm. Anomalies perpendicular to the main geological structures are not uncommon within HT fields in Iceland. This is observed in Reykjanes (e.g., Khodayar et al., 2018), Krafla (e.g., Árnason, 2020) and in Hengill (e.g., Hersir et al., 1990; Árnason et al., 2010; Obermann et al., 2022). In Hengill, a resistivity low, a zone of intense geothermal surface manifestations, and a magnetic low, all transect the Hengill volcanic system. In Krýsuvík, our observed low-velocity anomaly coincides fairly well with a vague zone of geothermal surface manifestations as well as trends of low resistivity structure caused by hydrothermal alteration (Hersir et al., 2020a).

Fagradalsfjall volcanic system

The Fagradalsfjall volcanic system is of enhanced interest due to the 2021-2023 volcano-tectonic rifting event (e.g., Fischer et al., 2022; Halldórsson et al., 2022; Pedersen et al., 2022; Sigmundsson et al., 2022). The Fagradalsfjall volcanic system differs in both size and in terms of eruption frequency compared to other volcanic systems on the RP (Sæmundsson et al., 2020). Most of the volcanic systems have experienced volcanism and rifting events every 800–1000 years for the last 4000 years, while Fagradalsfjall has not experienced volcanism for over 6000 years (Sæmundsson et al., 2020). According to the literature (e.g., Flóvenz et al., 2022), there is no known HT geothermal field within the Fagradalsfjall volcanic system (Figure 5.1), but notably, no resistivity survey has been carried out nor have exploratory wells been drilled in the area. At this point in time, there is not much published on the geophysics of the Fagradalsfjall volcanic system.

We observe a low-velocity anomaly at the depth of 4 km at the boundaries of the Eldvörp-Svartsengi and Fagradalsfjall volcanic systems, indicated by a black circle in Figure 5.8c. The anomaly extends to greater depths and towards the northwest in Figure 5.8d with a perpendicular direction to the plate boundary. At the depth of 4 km (Figure 5.8c), this low-velocity anomaly is located around 1 km northwest of the 2021, 2022, and 2023 Fagradalsfjall eruption sites indicated by the yellow star (Pedersen et al., 2022). Consequently, it is plausible that this low-velocity anomaly

might be related to the recent eruptions in the area, perhaps aided by the suggested crustal weakening under tension at this location (Fischer et al., 2022). It should, however, be noted that the seismic data used in our ANSWT are from 2014-2015.

The vertical cross sections at the location of the recent eruptions sites (Figure 5.12), display a rather high-velocity patch between 3 and 6 km depth, while the velocity decreases between 7 and 11 km depth. The seismicity within the brittle part of the RP crust between 2017 and 2022, is mostly confined to 2-6 km depth (Fischer et al., 2022; Ágústsdóttir et al., 2023) and, therefore, lies within the same depth range as the high shear wave velocity patch below Fagradalsfjall. The deep long-period earthquakes below Fagradalsfjall at 8-12 km depth observed by Greenfield et al. (2022) lie within the ductile part of the crust and are likely due to higher strain rates (fluid or gas movements). These deep earthquakes coincide with the low shear wave anomaly we observe between longitudes -22.3°W to -22.2°W at a depth of 7-11 km indicated by the black circles in Figure 5.12b-c.

Are there links between the HT fields on the RP?

In a number of our figures, there are hints of potential links between the HT fields on the RP (Figures 5.8-5.11). However, these could also reflect variations of the BDT zone, and the way cross-sections are plotted. In some cases, we are likely imaging the BDT zone and how it coincides in a location with the low shear wave anomalies below the HT fields, as in Figure 5.9b, but in other cases, we are likely imaging potential links, e.g., between Krýsuvík and Fagradalsfjall in Figures 5.10c and 5.11c. At the depth of 8 km (Figure 5.8e), the low-velocity (< 3.6 km/s) can be observed to connect all the volcanic systems, and, therefore, the HT fields too.

It is not unreasonable that all or many of the volcanic systems on the RP may be interconnected, as they have all erupted during the same rifting episodes over the last 4000 years, except Fagradalsfjall (Sæmundsson et al., 2020). The Sæmundsson et al. (2020) dating of Holocene lava flows has shown that during rifting episodes over the last 4000 years, the volcanic activity has affected each system individually, with the activity jumping successively from east to west. Furthermore, Flóvenz et al. (2022) suggest that geothermal fluids can move along the BDT zone between HT fields, and elevated seismicity in one RP volcanic system also affects the other systems (Sigmundsson et al., 2022).

5.7.5 The Moho discontinuity

The Moho is the boundary between the crust and the mantle of the Earth. It is estimated to be at a depth of around 8-20 km below the RP, most likely at 15 km depth (e.g., Weir et al., 2001; Jacoby et al., 2007). Below the Moho depth, the shear wave velocity is almost constant and estimated to be around 4.3-4.5 km/s. Looking at the vertical cross sections of Figures 5.9-5.12, we see an almost constant velocity below 15 km depth. Assuming a velocity of 4.3 km/s around the depth of the Moho, the Moho depth appears to vary a bit in the study area but can approximately be considered to be at a depth of 15 km.

5.7.6 Qualitative comparison of shear wave and electrical resistivity images

Finally, we compare our shear wave images below the Krýsuvík and the Reykjanes HT geothermal fields with electrical resistivity images obtained in two recent studies (Hersir et al., 2020a; Karlsdóttir et al., 2020). A clear (qualitative) correlation between low shear wave velocities and low resistivities in the uppermost 2-3 km can be observed (Figures 5.13a-d, Figures 5.14a-b). Interestingly, a similar structure can be inferred from both the resistivity and seismic images, i.e., some sort of up-doming from 4-6 km depth to 1-2 km depth (Figures 5.13a,c, Figures 5.14a-b). Both methods likely reflect a heat up-flow, although they map different physical parameters.

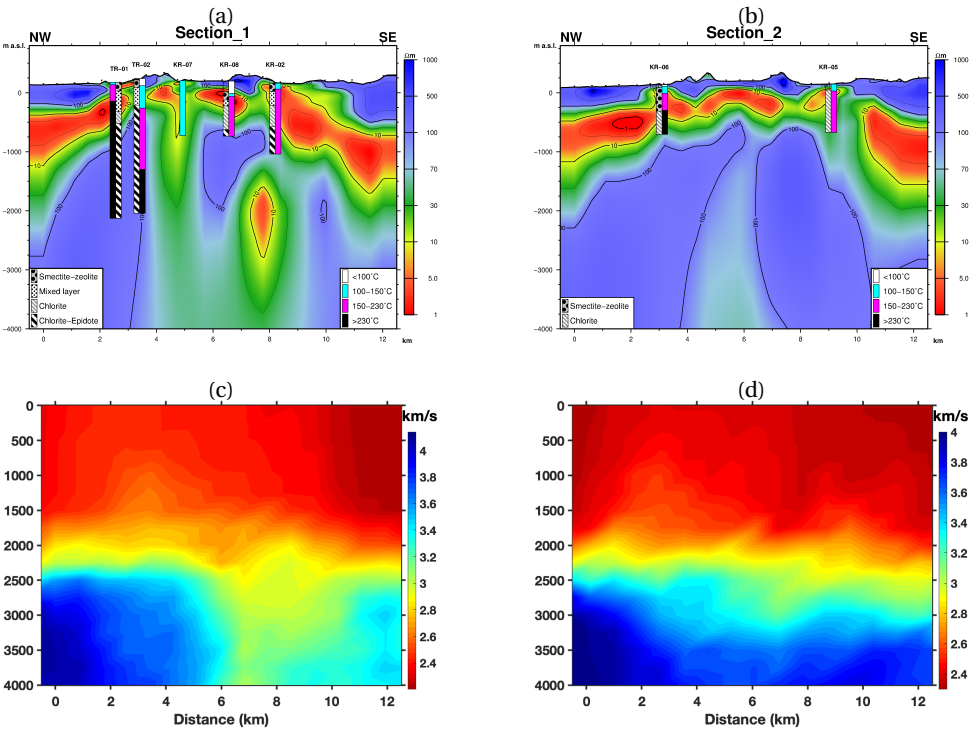

Figure 5.13. *Vertical cross-sections transecting the Krýsuvík volcanic system; comparing the electrical resistivity (a, b) and the recovered shear wave velocity (c, d). The two electrical resistivity profiles (a, b) show hydrothermal alteration and measured temperature in wells close to the cross-sections (taken from Hersir et al., 2020a).*

Our seismic results are smoother and provide less detail, particularly in the top 2 km. This is inherent to the adopted probabilistic method, the chosen ray-based travel time approach, and the frequencies of the surface waves we used in this study, which are limited to 0.1-0.5 Hz. Still, the shear wave velocities are low and show a weak up-doming in agreement with the up-doming shallow low resistivity. As we discussed in Figure 5.3, our data are mostly sensitive to shear wave velocities

at depths between 3 and 8 km. For a higher resolution and hence more details of the top 2 km of the subsurface, higher frequency surface waves would need to be included in our probabilistic inversion. At higher frequencies, residual timing errors and interference from higher modes prevented us from identifying reliable phase velocities for the fundamental mode. Nevertheless, the electrical resistivity cross-sections and the corresponding shear wave velocity cross-sections appear to be roughly consistent with each other, showing similar broad features.

Figure 5.13a shows well the up-doming of the low resistivity at 6-9 km along the cross-section well with the up-doming of low-velocities on Figure 5.13c, as well as the high resistivity captured by higher shear wave speeds. Figure 5.13b is simpler, here it is more clear that the central up-doming of low resistivity (at 5-7 km distance along the cross-section) can be associated with up-doming of lower-velocities in Figure 5.13d at the same location. It should be noted that the 3D resistivity models are somewhat non-unique. It is, however, encouraging that the two different geophysical approaches give comparable results. Sánchez-Pastor et al. (2021) also observed a correlation between resistivity and shear wave velocity within the Hengill HT geothermal field. The added benefit of this study is that it covers a large area, the entire RP, and has a larger depth of investigation. It can, therefore, give good first indications on where to find geothermal heat up-flow.

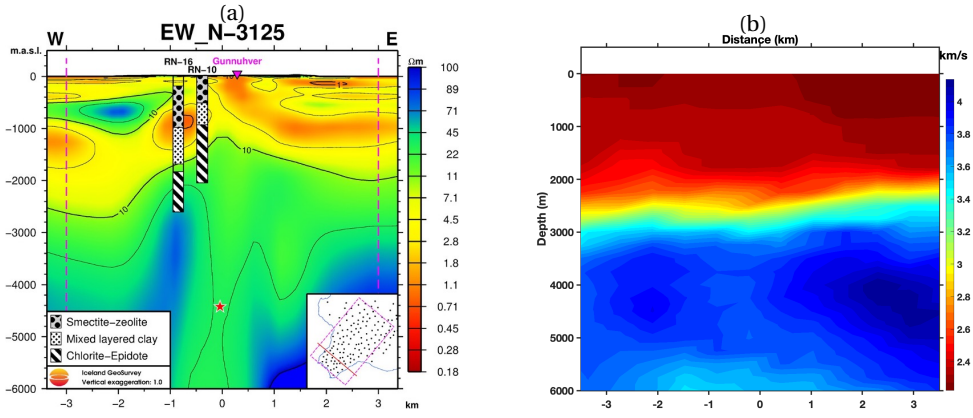

Figure 5.14. *Cross-section transecting the Reykjanes volcanic system; comparing the electrical resistivity (a) and the recovered shear wave velocity (b). The electrical resistivity profile (a) shows hydrothermal alteration in wells close to the cross-section, the inset figure shows the location of the cross-section (taken from Karlsdóttir et al., 2020).*

Figure 5.14a shows a resistivity profile transecting the Reykjanes volcanic system, taken from Karlsdóttir et al. (2020). The corresponding shear wave velocity profile is shown in Figure 5.14b. A good (qualitative) correlation between the low-velocities and the resistivity structure is observed. Similar to Figure 5.13, the shear wave velocity profiles are smoother than the resistivity profiles but still capture the up-doming of the low shear wave velocity, with higher resistivity and higher shear

wave velocities on either side.

5.8 Conclusion

We used ambient noise cross-correlations between 79 seismic stations from the extended IMAGE seismic network on- and off-shore the Reykjanes Peninsula (RP) to obtain a (relatively) high-resolution shear wave velocity model of the RP. Actually, this is the first tomographic model of the whole RP which is based on both on- and off-shore seismic stations. We first extracted fundamental mode phase velocity dispersion curves using (frequency-dependent) phase travel times in the frequency range of 0.1 to 0.5 Hz, resulting in the best-resolved depths at 2-8 km depth. Subsequently, we used a recently developed one-step transdimensional McMC algorithm to recover the posterior probability distribution of the possible 3D shear wave velocity models. In general, we observe that the velocity increases from the Earth's surface down to 20 km depth of the pointwise averaged shear wave velocity model. At 5 to 8 km depth, a decrease in velocity is observed, consistent with the brittle-ductile transition (BDT) on the RP. Moreover, at 7 km depth, all the volcanic systems are on some level connected by a relatively low-velocity anomaly.

Interestingly, the velocity reduction domes up to 3 km depth below all known HT geothermal fields on the RP, i.e., Reykjanes, Svartsengi, and Krýsuvík (Figure 5.1). This correlates well with previously recorded up-doming of the BDT below the same HT fields. We suggest that the observed low-velocity anomalies are due to the an-elasticity of the BDT zone, combined with the high temperatures of the HT fields, although some amount of partial melt can not be excluded. The observed low-velocity anomalies below Reykjanes and Eldvörp-Svartsengi are relatively small but still significant, while the low-velocity anomaly below Krýsuvík is much larger. The Krýsuvík low-velocity anomaly extends almost perpendicular to the volcanic system towards the southeast, coinciding with geothermal surface manifestations and the resistivity structure. More interestingly, a low-velocity anomaly is observed at 3-6 km depth about 1 km northwest of the recent Fagradalsfjall eruption site.

The (qualitative) correlation of our recovered shear wave velocities with resistivity studies conducted on the RP, suggests that the one-step transdimensional algorithm has successfully recovered the shear wave velocity structure below the RP. Our shear wave velocity model is smoother and contains fewer details than the recent resistivity studies, especially near the surface (< 2 km depth), due to the limited frequency range of the fundamental mode surface waves used, but it captures well the same broad features of the heat up-flow. Considering that this algorithm needs less user-defined (and hence somewhat subjective) parameters, it has great potential to become a routine tool for surface wave seismic tomography.

6

Conclusions

In this thesis, we investigate surface wave inversion utilizing a Bayesian inference algorithm usually referred to as Transdimensional Markov chain Monte Carlo (McMC). Progressing from 1D to 3D applications, our findings underscore the adaptability, efficiency gains, and interpretability inherent in the transdimensional McMC surface wave inversion approach.

In Chapter 2, we look into the application of the transdimensional McMC in a nonlinear 1D problem setup, specifically focusing on dispersion curve inversion. We provide a comprehensive comparison with both the conventional McMC approach (utilizing fixed parametrization) and a nonlinear iterative least-squares approach. The conventional McMC method reveals inefficiencies, sensitivities to parameters, and limitations in exploring expansive model spaces. The least-squares method requires meticulous parametrization of the model space, appropriate and sometimes slightly arbitrary regularization to address non-uniqueness, and a sufficiently accurate initial guess to avoid local minima. In contrast, the transdimensional McMC algorithm demonstrates self-parametrization, adaptability in terms of cell density, and inherent estimation of uncertainty. Application to local, noise-derived interferometric surface wave dispersion curves on the Reykjanes Peninsula shows automatic and localized smoothing, demonstrating superior adaptability compared to the uniform smoothing inherent in regularized least-squares inversions.

In chapter 3, we explore the potential of straight fiber Distributed Acoustic Sensing (DAS) data in conjunction with a 2D transdimensional McMC algorithm to recover a reliable 2D shear wave velocity section. Successful implementation involves obtaining laterally varying, local phase velocities through multi-offset phase analysis and applying the transdimensional algorithm to simultaneously invert all available dispersion curves. Notably, an interface at approximately 20 meters depth exhibits high uncertainty, consistent with observed abrupt changes in borehole-log derived shear wave velocities at that depth. The resulting shear wave velocity section displays smooth lateral variations, influenced by the smoothing behavior inherent in the employed multi-offset phase analysis. To enhance the resolution in the shallow

near-surface, we recommend retrieving higher surface wave modes for inversion and employing advanced techniques like common midpoint cross-correlation (CMPCC) to improve the quality of phase velocity versus offset and extend it to higher frequencies.

Chapters 4 and 5 focus on the application of the one-step transdimensional algorithm to noise-derived interferometric Rayleigh waves to recover the 3D shear wave velocity of the Reykjanes Peninsula (RP). We modify an existing one-step tomographic approach to directly recover shear wave velocity from dispersion curves and successfully apply the algorithm to synthetic and field data from the RP (Chapters 4 and 5, respectively). The resulting high-resolution shear wave velocity model is the first tomographic model covering the entire RP, and is based on ambient noise recordings of both on- and off-shore seismic stations. While our model is smoother than electrical resistivity models and contains fewer details than recent resistivity studies, especially near the surface (< 2 km depth), due to the limited frequency range of the fundamental mode surface waves used, it captures the same features in terms of geology and thermal structure. The added benefit of our 3D shear wave velocity model is its extensive coverage of the entire RP, providing valuable initial indications for locating geothermal heat flow near the surface.

The transdimensional algorithm presented in this study is promising for advancing surface wave inversion applications. Nevertheless, there is always room for improvement. Firstly, despite the flexibility and adaptability of the transdimensional McMC, there is room for improvement in terms of computational cost. The integration of the transdimensional McMC with the Hamiltonian Monte Carlo has the potential to significantly reduce computational time. Further progress is also possible through the use of variational inference. Secondly, defining the proposal width of a move can pose challenges, requiring a deep understanding of the algorithm. The incorporation of adaptive McMC could alleviate this difficulty, enhancing the algorithm's user-friendliness. Moreover, the performance of the McMC may improve through the use of variational inference. Lastly, the current, rather qualitative assessment of algorithm convergence can benefit from a quantitative approach.

A

Appendices

A.1 Noise hyperparameter conditional posterior probability

We need to derive the noise hyperparameter conditional posterior distribution. Applying Bayes' theorem, the posterior distribution ($p(a|\mathbf{d},\mathbf{m})$) is proportional to the product of the likelihood ($p(\mathbf{d}|a,\mathbf{m})$) and the prior (Gelman et al., 2014):

$$p(a|\mathbf{d},\mathbf{m}) \propto p(\mathbf{d}|a,\mathbf{m})p(a), \tag{A.1}$$

where the prior on a, $p(a)$, is assumed to be uniform (within bounds). Here, $p(\mathbf{d}|a,\mathbf{m})$ can be replaced by the likelihood function 3.6 for a specific a and the known model $\mathbf{m}$. It is worth mentioning that, $\mathbf{m}$ is treated as a known constant in Equation A.1, not a parameter that varies. The likelihood and the prior depend on a, and the hyperparameter posterior distribution is updated based on the observed data $\mathbf{d}$ and the known model $\mathbf{m}$.

Inserting the likelihood function (conditional on $\mathbf{m}$ in Equation A.1 gives:

$$p(a|\mathbf{d},\mathbf{m}) \propto \prod_{i=1}^{N_f}\prod_{j=1}^{N_x}\left(\frac{1}{\sigma_{ij}\sqrt{2\pi}}\exp\left(-\frac{\left(g_{ij}(\mathbf{m})-d_{ij}\right)^2}{2\sigma_{ij}^2}\right)\right)p(a). \tag{A.2}$$

By substituting $\sigma_{ij} = a\sigma'_{ij}$ from Equation 3.19 and some algebraic manipulation, Equation A.2 can be rewritten as:

$$p(a|\mathbf{d},\mathbf{m}) = \left(\prod_{i=1}^{N_f}\prod_{j=1}^{N_x}\frac{1}{\sigma'_{ij}\sqrt{2\pi}}\right)\left(\frac{1}{a^2}\right)^{\frac{N_xN_f}{2}}\exp\left(-\frac{1}{a^2}\sum_{i=1}^{N_f}\sum_{j=1}^{N_x}\frac{\left(g_{ij}(\mathbf{m})-d_{ij}\right)^2}{2{\sigma'_{ij}}^2}\right)p(a). \tag{A.3}$$

This equation can be rewritten as:

$$p(a|\mathbf{d},\mathbf{m}) = L\tau^{\alpha-1}\exp(-\beta\tau), \tag{A.4}$$

A

where,

$$\tau = \frac{1}{a^2},$$
$$\alpha = \frac{N_x N_f}{2} + 1,$$
$$\beta = \sum_{i=1}^{N_f} \sum_{j=1}^{N_x} \frac{\left(g_{ij}(\mathbf{m}) - d_{ij}\right)^2}{2{\sigma'_{ij}}^2},$$
$$L = p(a)\left(\prod_{i=1}^{N_f} \prod_{j=1}^{N_x} \frac{1}{\sqrt{2\pi}\sigma'_{ij}}\right).$$

A.2 Rayleigh wave phase velocity retrieval

Rayleigh waves are interface waves that travel along the free surface of a solid medium. They become dispersive if the medium's shear wave velocity varies (usually increases) with depth. This dispersive behavior means that at different frequencies, Rayleigh waves propagate along the Earth's surface at different velocities. In other words, their wave speed is frequency-dependent in a vertically heterogeneous medium. Consequently, each phase reaches the receiver at a different time. Extracting frequency-dependent travel times from a set of interferometric surface waves traversing a region, therefore allows one to estimate the shear wave velocity structure of that region.

The theory underlying seismic interferometry predicts that time-averaged cross-correlations of long recordings of ambient seismic noise may coincide with the surface wave part of the medium's Green's function (Wapenaar & Fokkema, 2006). This implies that these cross-correlation functions can be used to extract frequency-dependent phase or group travel times. These travel times may subsequently be used to solve a tomographic inverse problem, resulting in 3D shear wave velocity images of the subsurface. This has been demonstrated at various scales and in different contexts (Shapiro & Campillo, 2004; Weemstra et al., 2013). At the same time, the limitations have also been pointed out by various authors (e.g., Weaver et al., 2009; Tsai, 2009). For a detailed derivation of the relation between the surface wave Green's function and the time-averaged cross-correlation, including underlying assumptions and limitations, we, therefore, refer to Halliday & Curtis (2008).

Assuming a lossless, laterally invariant subsurface, and ignoring higher order modes (i.e., only considering the fundamental mode), the real part of the surface wave Green's function (frequency-domain representation) coincides with a zeroth order Bessel function of the first kind ($J_0(\alpha)$; e.g. Boschi et al., 2013). Here,

$$\alpha = \frac{2\pi f r}{cp(f)}, \tag{A.5}$$

where f is frequency, r the station-station distance, and $cp(f)$ the (Rayleigh wave) phase velocity at frequency f. The latter function is the sought-for phase velocity dispersion curve. The above implies that the dispersive character of the medium

between two specific stations, which are separated by a distance r, can be estimated by equating the zeros of the real part of the time-averaged cross-correlation to the zeros of $J_0(\alpha)$. Because the amplitudes of interferometric surface wave responses may suffer from both processing artifacts and violated conditions, equating the zeros is preferred over equating the real part in its entirety (Ekström et al., 2009; Weemstra et al., 2014, 2015).

For a specific station couple separated by distance r, the (average) phase velocity along the ray connecting the two stations is estimated as follows. At each frequency f for which the real part of the cross-spectrum coincides with zero, a set of candidate phase velocities $cp_j(f)$ $(j = 1,2,...)$ exists. These cp_j are obtained by equating the zeros of $J_0(2\pi f r/cp(f))$, for all $cp(f)$, to the cross-spectrum's zeros. This is done for each zero separately. Figure A.1 illustrates this process for three different station couples. The top row depicts the computed time-averaged cross-correlations. The middle row presents the real part of the cross-spectrum, which is interpolated using cubic splines, where the zeros are represented as solid red dots. For each zero, the different candidate phase velocities cp_j are shown as open blue circles in the bottom row.

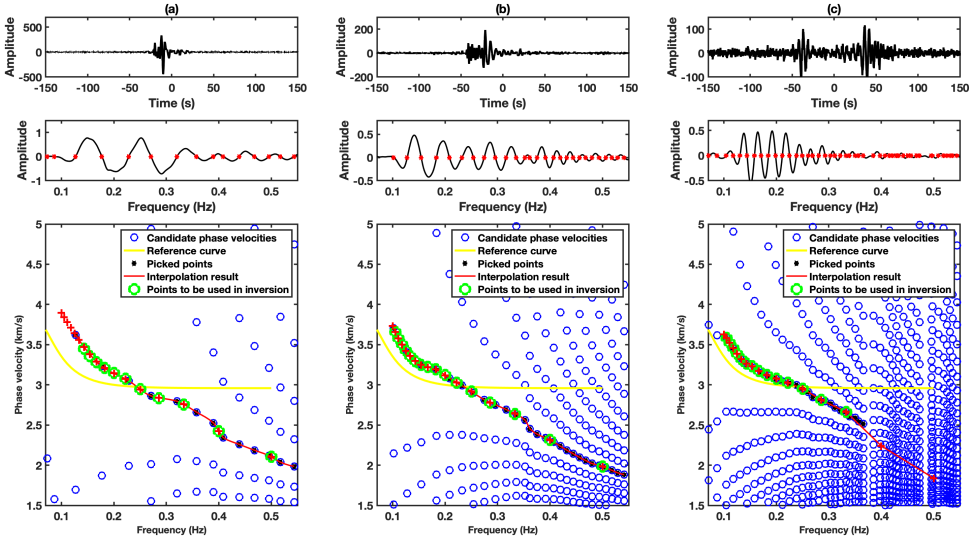

Figure A.1. *Examples of picked phase velocities for three station couples with station-station distances of (a) 25.1 km, (b) 50 km, and (c) 99 km. The top row shows the time-averaged cross-correlation of the corresponding station couple filtered between 0.1 and 0.5 Hz. The middle row shows the real part of the cross-spectrum, interpolated using cubic splines. The bottom row shows candidate phase velocities cp_j for each zero (open blue dots). The picked, and subsequently interpolated dispersion curve, is depicted as a red line. The red plus signs depict phase velocities at an a-priori defined set of frequencies. The corresponding data and codes are accessible on* https://doi.org/10.4121/3c97b1c8-1736-495d-a2f9-bd26dc958575.

A

After calculating the candidate phase velocities for each station couple and zero, the next step is to determine the set of phase velocities (i.e., the non-interpolated dispersion curve) that best represents the true phase velocities. To that end, surface wave dispersion associated with a reference model is often used (for example the preliminary reference Earth model PREM; Dziewonski & Anderson, 1981). This curve (yellow line in Figure A.1) is used to identify the start of the dispersion curve at the lower end of the spectrum, such as 0.05 to 0.2 Hz. At higher frequencies, the reference curve flattens out because the PREM does not account for (small-scale) near-surface structure. By imposing a constraint that our picked curve should be continuous, we stop the picking process at the frequency where there is a jump or discontinuity in phase velocity between adjacent frequencies. (For details regarding the picking algorithm we refer to Kästle et al., 2016). The rationale behind this is the following: the signal-to-noise ratio (SNR) of the interferometric surface waves decreases with increasing frequency, which may result in such jumps. This decrease in SNR with increasing frequency can be due to (i) stronger attenuation at higher frequencies, (ii) stronger scattering at higher frequencies (and hence a less pronounced ballistic surface wave), (iii) cross-modal terms (Halliday & Curtis, 2008), or (iv) a combination of these.

The solid blue circles in the bottom row of Figure A.1 are the picked phase velocities. By means of a cubic spline algorithm, we interpolate those points to obtain phase velocities at an a-priori defined set of discrete frequencies f_i ($i = 1, 2, ...$). The latter is the same for each station couple and hence facilitates a tomographic inversion. The interpolation result is the red line; red plus signs indicate the selected phase velocities at the a-priori defined frequencies. Importantly, however, not all of these selected phase velocities are deemed reliable. They need to fulfill the criteria that the associated station-station distances exceed one and half a wavelength (at the a-priori defined frequency). This wavelength is computed using the reference phase velocity curve. For closely separated stations, in particular, this implies that several selected phase velocities at the lower end of the frequency spectrum are discarded. The reason to discard phase velocities associated with closely separated stations (in terms of wavelengths) is that these phase velocities are highly sensitive to deviations from a uniform noise illumination pattern (Weaver et al., 2009; Froment et al., 2010). Green circles in Figure A.1 show the phase velocities that are deemed reliable and used in the inversion.

A.3 Model uncertainties corresponding to the Reykjanes Peninsula shear wave velocity model

As we discussed in the text, quantifying solution uncertainties is an advantage of probabilistic inversion algorithms. Here, we present the posterior standard deviation (i.e., a measure of uncertainty) with respect to the posterior means (pointwise average of the retained post-burn-in samples) provided in chapter 5. Figures A.2-A.6 present the posterior standard deviation with respect to the posterior means presented in Figures 5.8-5.12. Figure A.2 shows horizontal slices of the posterior standard deviation at the same depths as Figure 5.8, but for the (greater) area that

was covered by all stations. Clearly, the uncertainties are lower in the areas that have a high station density (indicated by the black dashed box in Figure A.2). It is the (pointwise) average of the ensemble of shear wave velocities inside this black box that is discussed and (geologically) interpreted in Section 5.7.

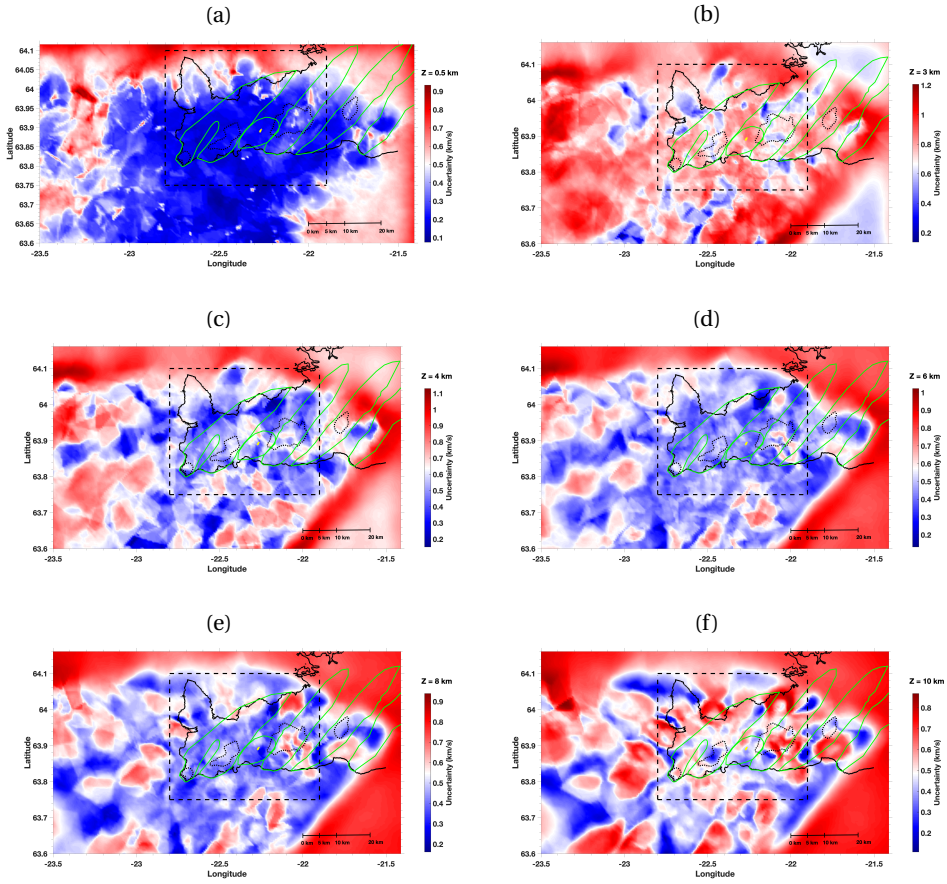

Figure A.2. *Pointwise standard deviation (from the retained post-burn-in samples) at six different depths: (a) 0.5 km, (b) 3 km, (c) 4 km, (d) 6 km, (e) 8 km, and (f) 10 km. The area with the highest resolution and the lowest uncertainties (40 km by 45 km) is indicated by the dashed black box.*

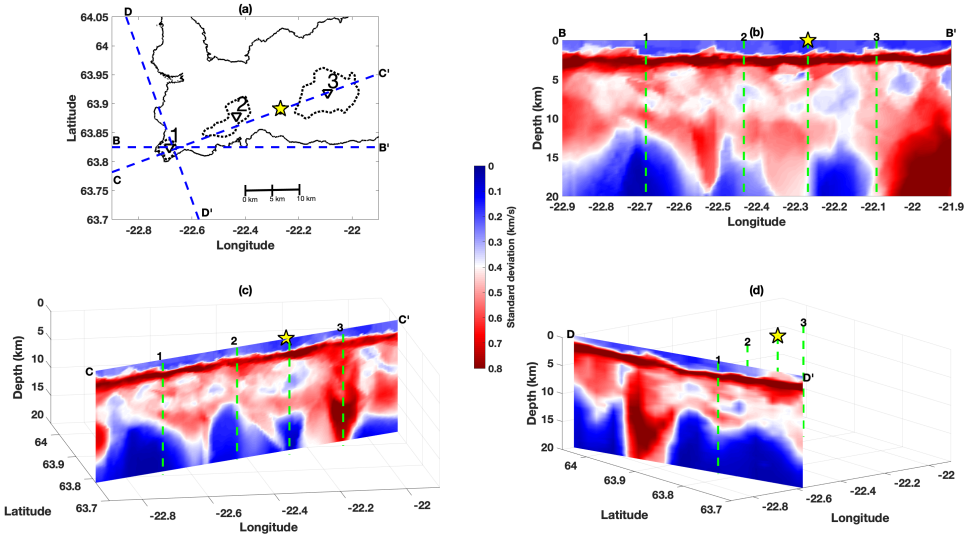

Figure A.3. *Vertical cross-sections, centered at the location of the Reykjanes HT geothermal field, of the pointwise standard deviation of the retained post-burn-in samples, corresponding to Figure 5.9. (a) Map of the area showing the location of three reference points, known high-temperature geothermal fields of Reykjanes, Svartsengi, and Krýsuvík (dashed black polygons), blue lines show the locations of the vertical cross-sections of the shear wave velocities along an east-west profile (b), N70°E oriented profile (c), and N20°W oriented profile (d).*

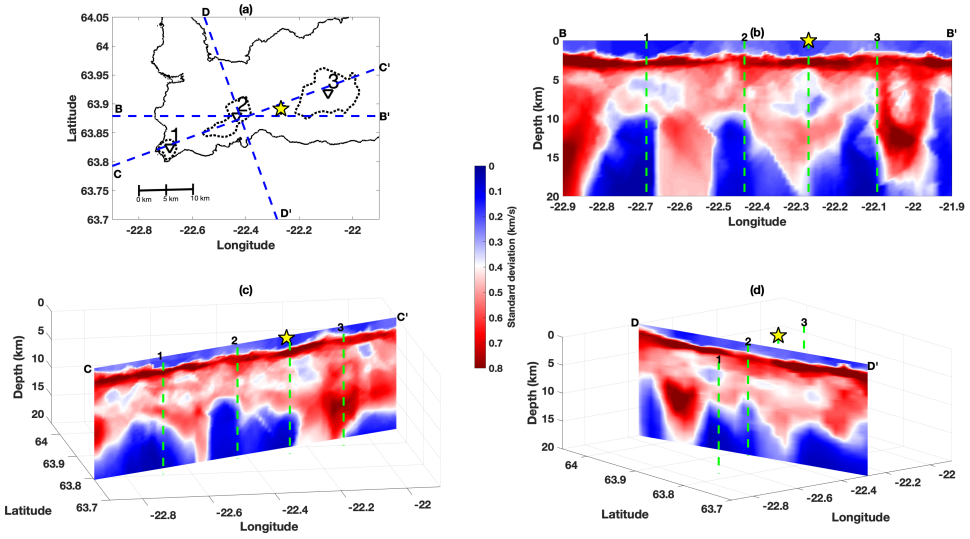

Figure A.4. *As Figure A.3, but centered at the location of the Eldvörp-Svartsengi HT geothermal field, corresponding to Figure 5.10.*

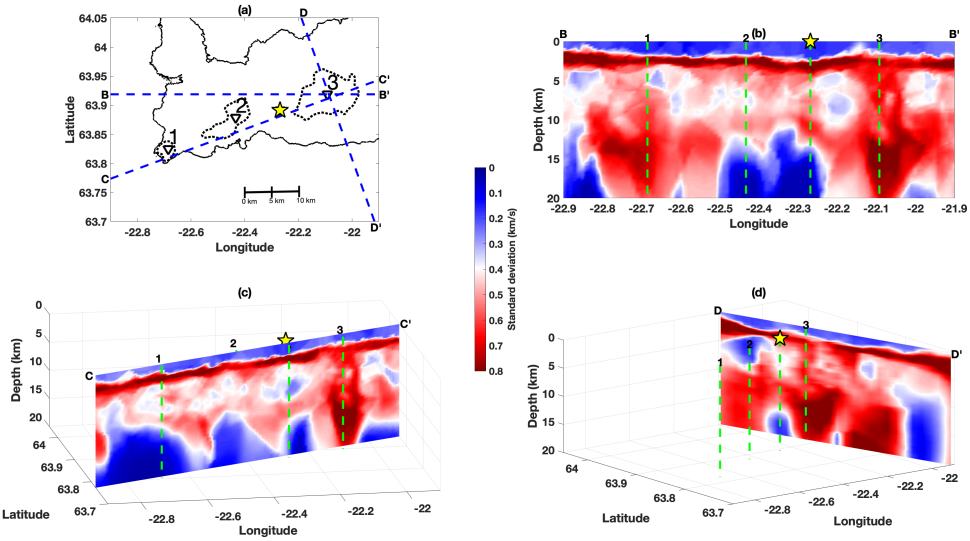

Figure A.5. *As Figure A.3, but centered at the location of the Krýsuvík HT geothermal field, corresponding to Figure 5.11.*

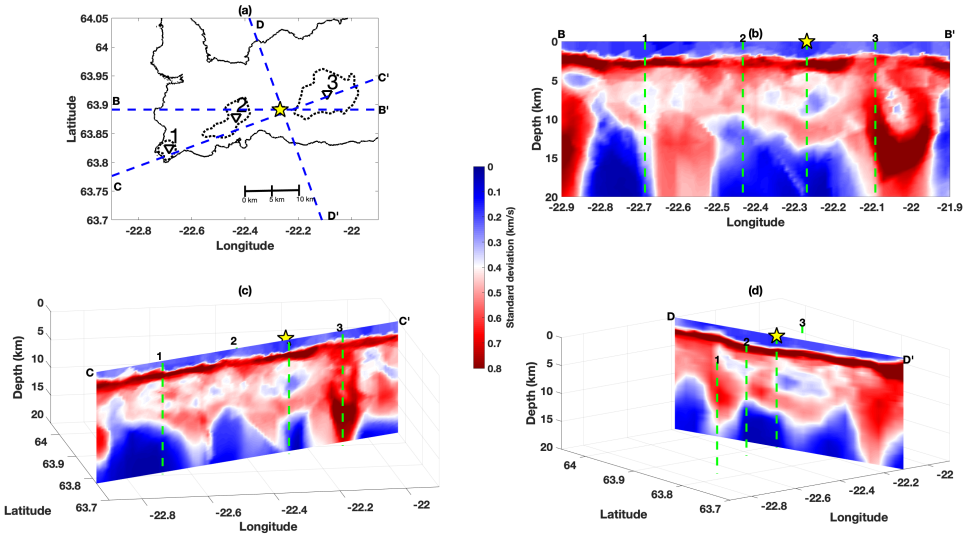

Figure A.6. *As Figure A.3, but centered at the location of the 2021-2023 eruptions site, on the Fagradalsfjall volcanic system, corresponding to Figure 5.12.*

Bibliography

Adelinet, M., Dorbath, C., Le Ravalec, M., Fortin, J., & Guéguen, Y., 2011. Deriving microstructure and fluid state within the Icelandic crust from the inversion of tomography data, *Geophysical Research Letters.*, **38**(3), https://www.doi.org/10.1029/2010GL046304.

Ágústsdóttir, T., Gudnason, E. Á., Magnússon, R. L., Fischer, T., Winder, T., Eibl, E. P., Glastonbury-Southern, E., Hersir, G. P., Horálek, J., Doubravová, J., et al., 2023. Relative earthquake relocations and detailed evolution of failed and successful lateral dyke intrusions during the 2021-2022 Fagradalsfjall volcano-tectonic rifting event, in *EGU General Assembly Conference Abstracts*, pp. EGU–13310, https://doi.org/10.5194/egusphere-egu23-13310.

Ágústsson, K. & Flóvenz, Ó. G., 2005. The thickness of the seismogenic crust in Iceland and its implications for geothermal systems, in *Proceedings of the World Geothermal Congress*, pp. 24–29.

Ajo-Franklin, J. B., Dou, S., Lindsey, N. J., Monga, I., Tracy, C., Robertson, M., Rodriguez Tribaldos, V., Ulrich, C., Freifeld, B., Daley, T., et al., 2019. Distributed acoustic sensing using dark fiber for near-surface characterization and broadband seismic event detection, *Scientific reports*, **9**(1), 1328, https://www.doi.org/10.1038/s41598-018-36675-8.

Aki, K. & Richards, P. G., 2002. *Quantitative Seismology*, University Science Books, Sausalito, California.

Al Hasani, M. & Drijkoningen, G., 2023. Experiences with Distributed Acoustic Sensing using both straight and helically wound fibers in surface-deployed cables–a case history in Groningen, The Netherlands, *Geophysics*, **88**(6), B369–B380, https://www.doi.org/10.1190/geo2022-0769.1.

Allen, R. M., Nolet, G., Morgan, W. J., Vogfjörd, K., Nettles, M., Ekström, G., Bergsson, B. H., Erlendsson, P., Foulger, G., Jakobsdóttir, S., et al., 2002. Plume-driven plumbing and crustal formation in Iceland, *Journal of Geophysical Research: Solid Earth*, **107**(B8), ESE–4, https://www.doi.org/10.1029/2001JB000584.

Andrieu, C., de Freitas, N., & Doucet, A., 1999. Robust full Bayesian learning for neural networks, *Advances in neural information processing systems*, **12**.

Árnason, K., 2020. New conceptual model for the magma-hydrothermal-tectonic system of Krafla, NE Iceland, *Geosciences*, **10**(1), 34, https://www.doi.org/10.3390/geosciences10010034.

Árnason, K., Eysteinsson, H., & Hersir, G. P., 2010. Joint 1D inversion of TEM and MT data and 3D inversion of MT data in the Hengill area, SW Iceland, *Geothermics*, **39**(1), 13–34, https://www.doi.org/10.1016/j.geothermics.2010.01.002.

Arnórsson, S., 1987. Gas chemistry of the Krísuvík geothermal field, Iceland, with special reference to evaluation of steam condensation in upflow zones, *Jökull*, (37), 31–48, https://www.doi.org/10.33799/jokull1987.37.031.

Arnórsson, S., Björnsson, A., Gíslason, G., & Gudmundsson, G., 1976. Systematic exploration of the Krísuvík high-temperature area, Reykjanes Peninsula, Iceland, in *Second UN Geothermal Symposium Proceedings*, pp. 853–864.

Aster, R. C., Borchers, B., & Thurber, C. H., 2018. *Parameter estimation and inverse problems*, Elsevier, https://doi.org/10.1016/C2015-0-02458-3.

Bali, E., Aradi, L. E., Zierenberg, R., Diamond, L. W., Pettke, T., Szabó, Á., Guðfinnsson, G. H., Friðleifsson, G. Ó., & Szabó, C., 2020. Geothermal energy and ore-forming potential of 600 °C mid-ocean-ridge hydrothermal fluids, *Geology*, **48**(12), 1221–1225, https://www.doi.org/10.1130/G47791.1.

Barone, I., Boaga, J., Carrera, A., Flores-Orozco, A., & Cassiani, G., 2021. Tackling lateral variability using surface waves: A tomography-like approach, *Surveys in Geophysics*, **42**, 317–338, https://www.doi.org/10.1007/s10712-021-09631-x.

Bayes, T., 1958. Essay towards solving a problem in the doctrine of chances, *Biometrika*, **45**, 293–315, https://www.doi.org/10.1093/biomet/45.3-4.293.

Beaty, K. S., Schmitt, D. R., & Sacchi, M., 2002. Simulated annealing inversion of multimode Rayleigh wave dispersion curves for geological structure, *Geophysical Journal International*, **151**(2), 622–631, https://www.doi.org/10.1046/j.1365-246X.2002.01809.x.

Belhadj, J., Romary, T., Gesret, A., Noble, M., & Figliuzzi, B., 2018. New parameterizations for Bayesian seismic tomography, *Inverse Problems*, **34**(6), 065007, https://www.doi.org/10.1088/1361-6420/aabce7.

Bensen, G., Ritzwoller, M., & Yang, Y., 2009. A 3-D shear velocity model of the crust and uppermost mantle beneath the United States from ambient seismic noise, *Geophysical Journal International*, **177**(3), 1177–1196, https://www.doi.org/10.1111/j.1365-246X.2009.04125.x.

Björnsson, S., Einarsson, P., Tulinius, H., & Hjartardóttir, Á. R., 2020. Seismicity of the Reykjanes Peninsula 1971–1976, *Journal of Volcanology and Geothermal Research*, **391**, 106369, https://www.doi.org/10.1016/j.jvolgeores.2018.04.026.

Blanck, H., Jousset, P., Hersir, G. P., Ágústsson, K., & Flóvenz, Ó. G., 2020. Analysis of 2014–2015 on-and off-shore passive seismic data on the Reykjanes Peninsula, SW Iceland, *Journal of Volcanology and Geothermal Research*, **391**, 106548, https://www.doi.org/10.1016/j.jvolgeores.2019.02.001.

Bodin, T. & Sambridge, M., 2009. Seismic tomography with the reversible jump algorithm, *Geophysical Journal International*, **178**(3), 1411–1436, https://www.doi.org/10.1111/j.1365-246X.2009.04226.x.

Bodin, T., Sambridge, M., & Gallagher, K., 2009. A self-parametrizing partition model approach to tomographic inverse problems, *Inverse Problems*, **25**(5), 055009, https://www.doi.org/10.1088/0266-5611/25/5/055009.

Bodin, T., Sambridge, M., Rawlinson, N., & Arroucau, P., 2012. Transdimensional tomography with unknown data noise, *Geophysical Journal International*, **189**(3), 1536–1556, https://www.doi.org/10.1111/j.1365-246X.2012.05414.x.

Bohlen, T., Kugler, S., Klein, G., & Theilen, F., 2004. 1.5 D inversion of lateral variation of Scholte-wave dispersion, *Geophysics*, **69**(2), 330–344, https://www.doi.org/10.1190/1.1707052.

Bohlen, T., De Nil, D., Köhn, D., & Jetschny, S., 2016. SOFI2D seismic modeling with finite differences: 2D—elastic and viscoelastic version, *user guide*.

Boiero, D. & Socco, L. V., 2010. Retrieving lateral variations from surface wave dispersion curves, *Geophysical prospecting*, **58**(6), 977–996, https://www.doi.org/10.1111/j.1365-2478.2010.00877.x.

Boschi, L., Weemstra, C., Verbeke, J., Ekstrom, G., Zunino, A., & Giardini, D., 2013. On measuring surface wave phase velocity from station-station cross-correlation of ambient signal, *Geophysical Journal International*, **192**, 346–358, https://www.doi.org/10.1093/gji/ggs023.

Bostick III, F., 2000. Field experimental results of three-component fiber-optic seismic sensors, in *SEG Technical Program Expanded Abstracts 2000*, pp. 21–24, Society of Exploration Geophysicists, https://www.doi.org/10.1190/1.1815889.

Buchen, P. & Ben-Hador, R., 1996. Free-mode surface-wave computations, *Geophysical Journal International*, **124**(3), 869–887, https://www.doi.org/10.1111/j.1365-246X.1996.tb05642.x.

Cabrera-Pérez, I., D'Auria, L., Soubestre, J., Barrancos, J., Padilla, G. D., & Pérez, N. M., 2021. A nonlinear multiscale inversion approach for ambient noise tomography, *Geophysical Journal International*, **225**(2), 1158–1173, https://www.doi.org/10.1093/gji/ggaa574.

Caracciolo, A., Bali, E., Halldórsson, S., Guðfinnsson, G., Kahl, M., Þórðardóttir, I., Pálmadóttir, G., & Silvestri, V., 2023. Magma plumbing architectures and timescales of magmatic processes during historical magmatism on the

Reykjanes Peninsula, Iceland, *Earth and Planetary Science Letters*, **621**, 118378, https://www.doi.org/10.1016/j.epsl.2023.118378.

Chen, X., Zhang, Y., Hui, D., Chen, M., & Wu, Z., 2017. Study of melting properties of basalt based on their mineral components, *Compos. B. Eng.*, **116**, 53–60, https://www.doi.org/10.1016/j.compositesb.2017.02.014.

Clifton, A. E. & Kattenhorn, S. A., 2006. Structural architecture of a highly oblique divergent plate boundary segment, *Tectonophysics*, **419**(1-4), 27–40, https://www.doi.org/10.1016/j.tecto.2006.03.016.

Cruz-Hernández, F., Gallardo, L. A., Calò, M., Castro, R. R., & Romo-Jones, J. M., 2022. Ambient noise tomography in the Cerro Prieto Basin, Baja California, Mexico from laterally constrained surface wave inversion, *Geophysical Journal International*, **229**(3), 1586–1603, https://www.doi.org/10.1093/gji/ggac017.

Daley, T. M., Freifeld, B. M., Ajo-Franklin, J., Dou, S., Pevzner, R., Shulakova, V., Kashikar, S., Miller, D. E., Goetz, J., Henninges, J., et al., 2013. Field testing of fiber-optic distributed acoustic sensing (DAS) for subsurface seismic monitoring, *The Leading Edge*, **32**(6), 699–706, https://www.doi.org/10.1111/1365-2478.12324.

Daley, T. M., Miller, D. E., Dodds, K., Cook, P., & Freifeld, B. M., 2016. Field testing of modular borehole monitoring with simultaneous distributed acoustic sensing and geophone vertical seismic profiles at Citronelle, Alabama, *Geophysical Prospecting*, **64**, 1318–1334, https://www.doi.org/10.1111/1365-2478.12324.

Darnet, M., Wawrzyniak, P., Coppo, N., Nielsson, S., Schill, E., & Fridleifsson, G., 2020. Monitoring geothermal reservoir developments with the Controlled-Source Electro-Magnetic method — A calibration study on the Reykjanes geothermal field, *Journal of Volcanology and Geothermal Research*, **391**, 106437, https://www.doi.org/10.1016/j.jvolgeores.2018.08.015.

Dettmer, J., Molnar, S., Steininger, G., Dosso, S. E., & Cassidy, J. F., 2012. Trans-dimensional inversion of microtremor array dispersion data with hierarchical autoregressive error models, *Geophysical Journal International*, **188**(2), 719–734, https://www.doi.org/10.1111/j.1365-246X.2011.05302.x.

Dosso, S. E., Dettmer, J., Steininger, G., & Holland, C. W., 2014. Efficient trans-dimensional Bayesian inversion for geoacoustic profile estimation, *Inverse Problems*, **30**(11), 114018, https://www.doi.org/10.1088/0266-5611/30/11/114018.

Du, Z., Foulger, G., Julian, B., Allen, R., Nolet, G., Morgan, W., Bergsson, B., Erlendsson, P., Jakobsdottir, S., Ragnarsson, S., et al., 2002. Crustal structure beneath western and eastern Iceland from surface waves and receiver functions, *Geophysical Journal International*, **149**(2), 349–363, https://www.doi.org/10.1046/j.1365-246X.2002.01642.x.

Dziewonski, A. M. & Anderson, D. L., 1981. Preliminary reference Earth model, *Physics of the earth and planetary interiors*, **25**(4), 297–356, https://www.doi.org/10.1016/0031-9201(81)90046-7.

Einarsson, P., 1991. Earthquakes and present-day tectonism in Iceland, *Tectonophysics*, **189**(1-4), 261–279, https://www.doi.org/10.1016/0040-1951(91)90501-I.

Einarsson, P., Eyjólfsson, V., & Hjartardóttir, Á. R., 2023. Tectonic framework and fault structures in the Fagradalsfjall segment of the Reykjanes Peninsula Oblique Rift, Iceland, *Bulletin of Volcanology*, **85**(2), 9, https://www.doi.org/10.1007/s00445-022-01624-x.

Ekström, G., Abers, G., & Webb, S., 2009. Determination of surface-wave phase velocities across USArray from noise and Aki's spectral formulation, *Geophysical Research Letters*, **36**, L18301, https://www.doi.org/10.1029/2009GL039131.

Fang, H., Yao, H., Zhang, H., Huang, Y.-C., & van der Hilst, R. D., 2015. Direct inversion of surface wave dispersion for three-dimensional shallow crustal structure based on ray tracing: methodology and application, *Geophysical Journal International*, **201**(3), 1251–1263, https://www.doi.org/10.1093/gji/ggv080.

Fischer, T., Hrubcová, P., Salama, A., Doubravová, J., Ágústsdóttir, T., Gudnason, E., Horálek, J., & Hersir, G. P., 2022. Swarm seismicity illuminates stress transfer prior to the 2021 Fagradalsfjall eruption in Iceland, *Earth and Planetary Science Letters*, **594**, 117685, https://www.doi.org/10.1016/j.epsl.2022.117685.

Flóvenz, Ó. G., Wang, R., Hersir, G. P., Dahm, T., Hainzl, S., Vassileva, M., Drouin, V., Heimann, S., Isken, M. P., Gudnason, E. Á., et al., 2022. Cyclical geothermal unrest as a precursor to Iceland's 2021 Fagradalsfjall eruption, *Nature Geoscience*, **15**(5), 397–404, https://www.doi.org/10.1038/s41561-022-00930-5.

Flóvenz, G. et al., 1980. Seismic structure of the Icelandic crust above layer three and the relation between body wave velocity and the alteration of the basaltic crust, *Journal of Geophysics*, **47**(1), 211–220, https://api.semanticscholar.org/CorpusID:210280877.

Foti, S., Lancellotta, R., Sambuelli, L., Socco, L. V., et al., 2000. Notes on fk analysis of surface waves, *Annali di Geofisica*, **43**(6), 1199–1209, https://www.doi.org/10.4401/ag-3683.

Foulger, G., Du, Z., & Julian, B., 2003. Icelandic-type crust, *Geophysical Journal International*, **155**(2), 567–590, https://www.doi.org/10.1046/j.1365-246X.2003.02056.x.

Friðleifsson, G., Albertsson, A., Elders, W., Sigurdsson, Ó., Karlsdottir, R., & Pálsson, B., 2011. The Iceland Deep Drilling Project (IDDP): planning for the second deep well at Reykjanes, *Geothermal Resources Council - Transactions*, **35**, 347–354.

Friðleifsson, G. Ó., Elders, W. A., Zierenberg, R. A., Fowler, A. P., Weisenberger, T. B., Mesfin, K. G., Sigurðsson, Ó., Níelsson, S., Einarsson, G., Óskarsson, F., et al., 2020. The Iceland Deep Drilling Project at Reykjanes: Drilling into the root zone of a black smoker analog, *Journal of Volcanology and Geothermal Research*, **391**, 106435, https://www.doi.org/10.1016/j.jvolgeores.2018.08.013.

Froment, B., Campillo, M., Roux, P., Gouédard, P., Verdel, A., & Weaver, R. L., 2010. Estimation of the effect of nonisotropically distributed energy on the apparent arrival time in correlations, *Geophysics*, **75**, SA85–SA93, https://www.doi.org/10.1190/1.3483102.

Galetti, E., Curtis, A., Meles, G. A., & Baptie, B., 2015. Uncertainty loops in travel-time tomography from nonlinear wave physics, *Physical review letters*, **114**(14), 148501, https://www.doi.org/10.1103/PhysRevLett.114.148501.

Galetti, E., Curtis, A., Baptie, B., Jenkins, D., & Nicolson, H., 2017. Transdimensional Love-wave tomography of the British Isles and shear-velocity structure of the East Irish Sea Basin from ambient-noise interferometry, *Geophysical Journal International*, **208**(1), 36–58, https://www.doi.org/10.1093/gji/ggw286.

Gelman, A., Roberts, G. O., Gilks, W. R., et al., 1996. Efficient Metropolis jumping rules, *Bayesian statistics*, **5**, 599–607, https://www.doi.org/10.1093/oso/9780198523567.003.0038.

Gelman, A., Carlin, J. B., Stern, H. S., & Rubin, D. B., 2014. Bayesian data analysis (Vol. 2), https://www.doi.org/10.1201/b16018.

Geman, S. & Geman, D., 1984. Stochastic relaxation, Gibbs distributions, and the Bayesian restoration of images, *IEEE Transactions on pattern analysis and machine intelligence*, **PAMI-6**(6), 721–741, https://www.doi.org/10.1109/TPAMI.1984.4767596.

Ghalenoei, E., Dettmer, J., Ali, M. Y., & Kim, J. W., 2022. Trans-dimensional gravity and magnetic joint inversion for 3-D earth models, *Geophysical Journal International*, **230**(1), 363–376, https://www.doi.org/10.1093/gji/ggac083.

Gilks, W. R., Richardson, S., & Spiegelhalter, D., 1995. *Markov chain Monte Carlo in practice*, CRC press, https://www.doi.org/10.1201/b14835.

Gorbatov, A., Fukao, Y., Widiyantoro, S., & Gordeev, E., 2001. Seismic evidence for a mantle plume oceanwards of the Kamchatka—Aleutian trench junction, *Geophysical Journal International*, **146**(2), 282–288, https://www.doi.org/10.1046/j.0956-540x.2001.01439.x.

Green, P. J., 1995. Reversible jump Markov chain Monte Carlo computation and Bayesian model determination, *Biometrika*, **82**(4), 711–732, https://www.doi.org/10.1093/biomet/82.4.711.

Green, P. J. & Hastie, D. I., 2009. Reversible jump MCMC, *Genetics*, **155**(3), 1391–1403.

Greenfield, T., Winder, T., Rawlinson, N., Maclennan, J., White, R. S., Ágústsdóttir, T., Bacon, C. A., Brandsdóttir, B., Eibl, E. P., Glastonbury-Southern, E., et al., 2022. Deep long period seismicity preceding and during the 2021 Fagradalsfjall eruption, Iceland, *Bulletin of Volcanology*, **84**(12), 1–20, https://www.doi.org/10.1007/s00445-022-01603-2.

Gudnason, E., Köpke, R., Gaucher, E., Ágústsson, K., Níelsson, S., & Kohl, T., 2020. Seismic monitoring during drilling and stimulation of well RN-15/IDDP-2 in Reykjanes, SW-Iceland, in *Proc. World Geothermal Congress 2020*, vol. 1, p. 13015.

Guðmundsson, M. T., Högnadóttir, Þ., & Háskólans, J., 2004. *Hraun og móbergsmyndanir á svæðinu frá Brennisteinsfjöllum að Hengli: niðurstöður þyngdarmælinga*, Jarðvísindastofnun Háskólans.

Halldórsson, S. A., Marshall, E. W., Caracciolo, A., Matthews, S., Bali, E., Rasmussen, M. B., Ranta, E., Robin, J. G., Guðfinnsson, G. H., Sigmarsson, O., et al., 2022. Rapid shifting of a deep magmatic source at Fagradalsfjall volcano, Iceland, *Nature*, **609**(7927), 529–534, https://www.doi.org/10.1038/s41586-022-04981-x.

Halliday, D. & Curtis, A., 2008. Seismic interferometry, surface waves and source distribution, *Geophysical Journal International*, **175**, 1067–1087, https://www.doi.org/10.1111/j.1365-246X.2008.03918.x.

Haney, M., Mikesell, T. D., van Wijk, K., & Nakahara, H., 2012. Extension of the spatial autocorrelation (SPAC) method to mixed-component correlations of surface waves, *Geophysical Journal International*, **191**(1), 189–206, https://www.doi.org/10.1111/j.1365-246X.2012.05597.x.

Haney, M. M. & Tsai, V. C., 2015. Nonperturbational surface-wave inversion: A Dix-type relation for surface waves, *Geophysics*, **80**(6), EN167–EN177, https://www.doi.org/10.1190/geo2014-0612.1.

Hawkins, R., Bodin, T., Sambridge, M., Choblet, G., & Husson, L., 2019. Trans-dimensional surface reconstruction with different classes of parameterization, *Geochemistry, Geophysics, Geosystems*, **20**(1), 505–529, https://www.doi.org/10.1029/2018GC008022.

Hayashi, K. & Suzuki, H., 2004. CMP cross-correlation analysis of multi-channel surface-wave data, *Exploration Geophysics*, **35**(1), 7–13, https://www.doi.org/10.1071/EG04007.

Herrmann, R. B., 2013. Computer programs in seismology: An evolving tool for instruction and research, *Seismological Research Letters*, **84**(6), 1081–1088, https://www.doi.org/10.1785/0220110096.

Hersir, G. P., Björnsson, G., & Björnsson, A., 1990. Eldstöðvar og jarðhiti á Hengilssvæðinu: jarðeðlisfræðileg könnun. Orkustofnun, Tech. rep., OS-90031/JHD-06.

Hersir, G. P., Árnason, K., Vilhjálmsson, A. M., Saemundsson, K., Ágústsdóttir, Þ., & Friðleifsson, G. Ó., 2020a. Krýsuvík high temperature geothermal area in SW Iceland: Geological setting and 3D inversion of magnetotelluric (MT) resistivity data, *Journal of Volcanology and Geothermal Research*, **391**, 106500, https://www.doi.org/10.1016/j.jvolgeores.2018.11.021.

Hersir, G. P., Flóvenz, Ó. G., Bruhn, D., Liotta, D., van Wees, J.-D., Halldórsdóttir, S., & Manzella, A., 2020b. Geothermal Exploration and Reservoir Assessment in Magmatic Systems The IMAGE Project, in *Proceedings World Geothermal Congress*.

Hobé, A., Gudmundsson, O., Tryggvason, A., et al., 2021. Imaging the 2010-2011 Inflationary Source at Krysuvik, SW Iceland, Using Time-Dependent Vp/Vs Tomography, in *Geothermal Congress 2020+ 1*.

Horálek, J., 2013. Reykjanet [2014-2015], International Federation of Digital Seismo-graph Networks, https://doi.org/10.7914/SN/7E_2013.

Icelandic Meteorological Office, 1992. Icelandic National Digital Seismograph Network [dataset], https://www.doi.org/10.7914/ZKJM-TJ71.

Jacoby, W. R., Weigel, W., & Fedorova, T., 2007. Crustal structure of the Reykjanes Ridge near 62° N, on the basis of seismic refraction and gravity data, *Journal of Geodynamics*, **43**(1), 55–72, https://www.doi.org/10.1016/j.jog.2006.10.002.

Jakobsdóttir, S. S., 2008. Seismicity in Iceland: 1994–2007, *Jökull*, **58**(1), 75–100, https://www.doi.org/10.33799/jokull2008.58.075.

Johannessen, K., Drakeley, B., & Farhadiroushan, M., 2012. Distributed acoustic sensing-a new way of listening to your well/reservoir, in *SPE Intelligent Energy International*, OnePetro, https://www.doi.org/10.2118/149602-MS.

Jousset, P., Blanck, H., Franke, S., Metz, M., Ágústsson, K., Verdel, A., Ryberg, T., Hersir, G. P., Weemstra, C., Bruhn, D., et al., 2016. Seismic tomography in Reykjanes, SW Iceland, *Extended Abstract EGC, Strasbourg*.

Jousset, P., Hersir, G. P., Blanck, H., Kirk, H., Erbas, K., Hensch, M., Franke, S., Bruhn, D., & Huenges, E., 2020a. IMAGE (Integrated Methods for Advanced Geothermal Exploration), https://doi.org/10.14470/9Y7569325908.

Jousset, P., Mortensen, A. K., Fridleifsson, G. Ó., Ágústsson, K., & Gudmundsson, M. T., 2020b. Reykjanes, Iceland: Structure and dynamics of mid-oceanic ridge geo/hydrothermal systems, *Journal of Volcanology and Geothermal Research*, **391**, 106692, https://www.doi.org/10.1016/j.jvolgeores.2019.106692.

Karato, S.-i., 2014. Does partial melting explain geophysical anomalies?, *Physics of the earth and planetary interiors*, **228**, 300–306, https://www.doi.org/10.1016/j.pepi.2013.08.006.

Karlsdóttir, R., Vilhjálmsson, A. M., & Guðnason, E. Á., 2020. Three dimensional inversion of magnetotelluric (MT) resistivity data from Reykjanes high temperature field in SW Iceland, *Journal of Volcanology and Geothermal Research*, **391**, 106498, https://www.doi.org/10.1016/j.jvolgeores.2018.11.019.

Kästle, E. D., Soomro, R., Weemstra, C., Boschi, L., & Meier, T., 2016. Two-receiver measurements of phase velocity: cross-validation of ambient-noise and earthquake-based observations, *Geophysical Journal International*, **207**(3), 1493–1512, https://www.doi.org/10.1093/gji/ggw341.

Khodayar, M., Björnsson, S., Guðnason, E. Á., Níelsson, S., Axelsson, G., & Hickson, C., 2018. Tectonic control of the Reykjanes geothermal field in the oblique rift of SW Iceland: from regional to reservoir scales, *Open Journal of Geology*, **8**(3), 333–382, https://www.doi.org/10.4236/ojg.2018.83021.

Korostelev, F., Weemstra, C., Leroy, S., Boschi, L., Keir, D., Ren, Y., Molinari, I., Ahmed, A., Stuart, G. W., Rolandone, F., Khanbari, K., Hammond, J. O. S., Kendall, J. M., Doubre, C., Ganad, I. A., Goitom, B., & Ayele, A., 2015. Magmatism on rift flanks: Insights from ambient noise phase velocity in Afar region, *Geophysical Research Letters*, **42**, 2179–2188, https://www.doi.org/10.1002/2015GL063259.

Kruiver, P. P., van Dedem, E., Romijn, R., de Lange, G., Korff, M., Stafleu, J., Gunnink, J. L., Rodriguez-Marek, A., Bommer, J. J., van Elk, J., & Doornhof, D., 2017. An integrated shear-wave velocity model for the Groningen gas field, The Netherlands, *Bulletin of Earthquake Engineering*, **15**(9), 3555–3580, https://www.doi.org/10.1007/s10518-017-0105-y.

Kurita, T., 1973. Regional variations in the structure of the crust in the central United States from P-wave spectra, *Bulletin of the Seismological Society of America*, **63**(5), 1663–1687, https://www.doi.org/10.1785/BSSA0630051663.

Lees, J. M., 2007. Seismic tomography of magmatic systems, *Journal of Volcanology and Geothermal Research*, **167**(1-4), 37–56, https://www.doi.org/10.1016/j.jvolgeores.2007.06.008.

Lehujeur, M., Vergne, J., Maggi, A., & Schmittbuhl, J., 2016. Ambient noise tomography with non-uniform noise sources and low aperture networks: case study of deep geothermal reservoirs in northern Alsace, France, *Geophysical Supplements to the Monthly Notices of the Royal Astronomical Society*, **208**(1), 193–210, https://www.doi.org/10.1093/gji/ggw373.

Lehujeur, M., Chevrot, S., Villaseñor, A., Masini, E., Saspiturry, N., Lescoutre, R., & Sylvander, M., 2021. Three-dimensional shear velocity structure of the Mauléon and Arzacq Basins (Western Pyrenees), *Bulletin de la Société Géologique de France*, **192**(1), 47, https://www.doi.org/10.1051/bsgf/2021039.

Levenberg, K., 1944. A method for the solution of certain non-linear problems in least squares, *Quarterly of applied mathematics*, **2**(2), 164–168, https://www.doi.org/10.1090/qam/10666.

Lindner, F., Weemstra, C., Walter, F., & Hadziioannou, C., 2018. Towards monitoring the englacial fracture state using virtual-reflector seismology, *Geophysical Journal International*, **214**(2), 825–844, https://www.doi.org/10.1093/gji/ggy156.

Lindsey, N. J., Martin, E. R., Dreger, D. S., Freifeld, B., Cole, S., James, S. R., Biondi, B. L., & Ajo-Franklin, J. B., 2017. Fiber-optic network observations of earthquake wavefields, *Geophysical Research Letters*, **44**(23), 11–792, https://www.doi.org/10.1002/2017GL075722.

Luo, Y., Xia, J., Liu, J., Xu, Y., & Liu, Q., 2008. Generation of a pseudo-2D shear-wave velocity section by inversion of a series of 1D dispersion curves, *Journal of Applied Geophysics*, **64**(3-4), 115–124, https://www.doi.org/10.1016/j.jappgeo.2008.01.003.

Marquardt, D. W., 1963. An algorithm for least-squares estimation of nonlinear parameters, *Journal of the society for Industrial and Applied Mathematics*, **11**(2), 431–441, https://www.doi.org/10.1137/0111030.

Martins, J. E., Ruigrok, E., Draganov, D., Hooper, A., Hanssen, R., White, R., & Soosalu, H., 2019. Imaging Torfajökull's magmatic plumbing system with seismic interferometry and phase velocity surface wave tomography, *Journal of Geophysical Research: Solid Earth*, **124**(3), 2920–2940, https://www.doi.org/10.1029/2018JB016002.

Martins, J. E., Weemstra, C., Ruigrok, E., Verdel, A., Jousset, P., & Hersir, G. P., 2020. 3D S-wave velocity imaging of Reykjanes Peninsula high-enthalpy geothermal fields with ambient-noise tomography, *Journal of Volcanology and Geothermal Research*, **391**, 106685, https://www.doi.org/10.1016/j.jvolgeores.2019.106685.

Mata Flores, D., Sladen, A., Ampuero, J.-P., Mercerat, E. D., & Rivet, D., 2023. Monitoring deep sea currents with seafloor distributed acoustic sensing, *Earth and Space Science*, **10**(6), e2022EA002723, https://www.doi.org/10.1029/2022EA002723.

McKenzie, D., 2000. Constraints on melt generation and transport from U-series activity ratios, *Chemical Geology*, **162**(2), 81–94, https://www.doi.org/10.1016/S0009-2541(99)00126-6.

McMechan, G. A. & Yedlin, M. J., 1981. Analysis of dispersive waves by wave field transformation, *Geophysics*, **46**(6), 869–874, https://www.doi.org/10.1190/1.1441225.

Menke, W., 2018. *Geophysical data analysis: Discrete inverse theory*, Academic press, https://doi.org/10.1016/C2016-0-05203-8.

Michalczewska, K., Hreinsdóttir, S., Árnadóttir, T., Hjaltadóttir, S., Ágústsdóttir, T., Gudmundsson, M., Geirsson, H., Sigmundsson, F., & Gudmundsson, G., 2012. Inflation and deflation episodes in the Krýsuvík volcanic system, in *AGU Fall Meeting Abstracts*, vol. 2012, pp. V33A–2843.

Molenaar, M. M., Hill, D. J., Webster, P., Fidan, E., & Birch, B., 2012. First downhole application of distributed acoustic sensing for hydraulic-fracturing monitoring and diagnostics, *SPE Drilling & Completion*, **27**(01), 32–38, https://www.doi.org/10.2118/140561-PA.

Nayak, A., Ajo-Franklin, J., et al., 2021. Measurement of Surface-Wave Phase-Velocity Dispersion on Mixed Inertial Seismometer–Distributed Acoustic Sensing Seismic Noise Cross-Correlations, *Bulletin of the Seismological Society of America*, **111**(6), 3432–3450, https://www.doi.org/10.1785/0120210028.

Neducza, B., 2007. Stacking of surface waves, *Geophysics*, **72**(2), V51–V58, https://www.doi.org/10.1190/1.2431635.

Nolet, G., 2008. *A breviary of seismic tomography*, Cambridge University Press: Cambridge, UK, https://www.doi.org/10.1017/CBO9780511984709.

Noorlandt, R., Drijkoningen, G., Dams, J., & Jenneskens, R., 2015. A seismic vertical vibrator driven by linear synchronous motors, *Geophysics*, **80**(2), EN57–EN67, https://www.doi.org/10.1190/geo2014-0295.1.

Obermann, A., Wu, S.-M., Ágústsdóttir, T., Duran, A., Diehl, T., Sánchez-Pastor, P., Kristjansdóttir, S., Hjörleifsdóttir, V., Wiemer, S., & Hersir, G. P., 2022. Seismicity and 3-D body-wave velocity models across the Hengill geothermal area, SW Iceland, *Frontiers in Earth Science*, **10**, 969836, https://www.doi.org/10.3389/feart.2022.969836.

Pálmason, G., 1971. *Crustal structure of Iceland from explosion seismology*, Reykjavik, Prentsmidjan Leiftur.

Park, C. B., Miller, R. D., & Xia, J., 1999. Multichannel analysis of surface waves, *Geophysics*, **64**(3), 800–808, https://www.doi.org/10.1190/1.1444590.

Paulsson, B., Fairborn, J., Goldman, R., Bunn, B., & Frederick, D., 1997. An all fiber optic borehole hydrophone array, in *SEG Technical Program Expanded Abstracts 1997*, pp. 250–253, Society of Exploration Geophysicists, https://www.doi.org/10.1190/1.1885876.

Pedersen, G. B., Belart, J. M., Óskarsson, B. V., Gudmundsson, M. T., Gies, N., Högnadóttir, T., Hjartardóttir, Á. R., Pinel, V., Berthier, E., Dürig, T., et al., 2022. Volume, effusion rate, and lava transport during the 2021 Fagradalsfjall eruption: Results from near real-time photogrammetric monitoring, *Geophysical Research Letters.*, **49**(13), e2021GL097125, https://www.doi.org/10.1029/2021GL097125.

Priestley, K. & McKenzie, D., 2006. The thermal structure of the lithosphere from shear wave velocities, *Earth and Planetary Science Letters*, **244**(1-2), 285–301, https://www.doi.org/10.1016/j.epsl.2006.01.008.

Priestley, K. & McKenzie, D., 2013. The relationship between shear wave velocity, temperature, attenuation and viscosity in the shallow part of the mantle, *Earth and*

Planetary Science Letters, **381**, 78–91, https://www.doi.org/10.1016/j.epsl.2013.08.022.

Qin, F., Luo, Y., Olsen, K. B., Cai, W., & Schuster, G. T., 1992. Finite-difference solution of the eikonal equation along expanding wavefronts, *Geophysics*, **57**(3), 478–487, https://www.doi.org/10.1190/1.1443263.

Qu, L., Dettmer, J., Hall, K., Innanen, K. A., Macquet, M., & Lawton, D. C., 2023. Trans-dimensional inversion of multimode seismic surface wave data from a trenched distributed acoustic sensing survey, *Geophysical Journal International*, **234**(2), 1051–1062, https://www.doi.org/10.1093/gji/ggad112.

Rawlinson, N. & Sambridge, M., 2004. Wave front evolution in strongly heterogeneous layered media using the fast marching method, *Geophysical Journal International*, **156**(3), 631–647, https://www.doi.org/10.1111/j.1365-246X.2004.02153.x.

Rawlinson, N., Sambridge, M., et al., 2003. Seismic traveltime tomography of the crust and lithosphere, *Advances in geophysics*, **46**, 81–199, https://www.doi.org/10.1016/S0065-2687(03)46002-0.

Rawlinson, N., Pozgay, S., & Fishwick, S., 2010. Seismic tomography: a window into deep Earth, *Physics of the Earth and Planetary Interiors*, **178**(3-4), 101–135, https://www.doi.org/10.1016/j.pepi.2009.10.002.

Ryberg, T. & Haberland, C., 2017. Bayesian inversion of refraction seismic traveltime data, *Geophysical Journal International*, **212**(3), 1645–1656, https://www.doi.org/10.1093/gji/ggx500.

Sæmundsson, K. & Sigurgeirsson, M., 2013. Reykjanesskagi, *Náttúruvá á Íslandi eldgos og jarðskjálftar*, pp. 379–401.

Sæmundsson, K., Sigurgeirsson, M. Á., & Friðleifsson, G. Ó., 2020. Geology and structure of the Reykjanes volcanic system, Iceland, *Journal of Volcanology and Geothermal Research*, **391**, 106501, https://www.doi.org/10.1016/j.jvolgeores.2018.11.022.

Sambridge, M., 1999. Geophysical inversion with a neighbourhood algorithm—I. Searching a parameter space, *Geophysical journal international*, **138**(2), 479–494, https://www.doi.org/10.1046/j.1365-246X.1999.00876.x.

Sambridge, M., 2014. A parallel tempering algorithm for probabilistic sampling and multimodal optimization, *Geophysical Journal International*, **196**(1), 357–374, https://www.doi.org/10.1093/gji/ggt342.

Sambridge, M. & Mosegaard, K., 2002. Monte Carlo methods in geophysical inverse problems, *Reviews of Geophysics*, **40**(3), 3–1, https://www.doi.org/10.1029/2000RG000089.

Sambridge, M., Rawlinson, N., et al., 2005. Seismic tomography with irregular meshes, *Geophysical Monograph-American Geophysical Union*, **157**, 49, https://www.doi.org/10.1029/157GM04.

Sambridge, M., Gallagher, K., Jackson, A., & Rickwood, P., 2006. Trans-dimensional inverse problems, model comparison and the evidence, *Geophysical Journal International*, **167**(2), 528–542, https://www.doi.org/10.1111/j.1365-246X.2006.03155.x.

Sánchez-Pastor, P., Obermann, A., Schimmel, M., Weemstra, C., Verdel, A., & Jousset, P., 2019. Short- and long-term variations in the Reykjanes geothermal reservoir from seismic noise interferometry, *Geophysical Research Letters*, **46**(11), 5788–5798, https://www.doi.org/10.1029/2019GL082352.

Sánchez-Pastor, P., Obermann, A., Reinsch, T., Ágústsdóttir, T., Gunnarsson, G., Tómasdóttir, S., Hjörleifsdóttir, V., Hersir, G. P., Ágústsson, K., & Wiemer, S., 2021. Imaging high-temperature geothermal reservoirs with ambient seismic noise tomography, a case study of the Hengill geothermal field, SW Iceland, *Geothermics*, **96**, 102207, https://www.doi.org/10.1016/j.geothermics.2021.102207.

Saygin, E. & Kennett, B., 2012. Crustal structure of Australia from ambient seismic noise tomography, *Journal of Geophysical Research: Solid Earth*, **117**(B1), https://www.doi.org/10.1029/2011JB008403.

Schaefer, J. F., Boschi, L., & Kissling, E., 2011. Adaptively parametrized surface wave tomography: methodology and a new model of the European upper mantle, *Geophysical Journal International*, **186**(3), 1431–1453, https://www.doi.org/10.1111/j.1365-246X.2011.05135.x.

Schippkus, S., Zigone, D., Bokelmann, G., Group, A. W., et al., 2018. Ambient-noise tomography of the wider Vienna Basin region, *Geophysical Journal International*, **215**(1), 102–117, https://www.doi.org/10.1093/gji/ggy259.

Sen, M. K. & Biswas, R., 2017. Transdimensional seismic inversion using the reversible jump Hamiltonian Monte Carlo algorithm, *Geophysics*, **82**(3), R119–R134, https://www.doi.org/10.1190/geo2016-0010.1.

Sethian, J. A., 1996. A fast marching level set method for monotonically advancing fronts, *Proceedings of the National Academy of Sciences*, **93**(4), 1591–1595, https://www.doi.org/10.1073/pnas.93.4.1591.

Shapiro, N. M. & Campillo, M., 2004. Emergence of broadband Rayleigh waves from correlations of the ambient seismic noise, *Geophysical Research Letters.*, **31**(7), https://www.doi.org/10.1029/2004GL019491.

Sigmundsson, F., Einarsson, P., Hjartardóttir, Á. R., Drouin, V., Jónsdóttir, K., Arnadottir, T., Geirsson, H., Hreinsdottir, S., Li, S., & Ofeigsson, B. G., 2020. Geodynamics of Iceland and the signatures of plate spreading, *Journal of Volcanology and Geothermal Research*, **391**, 106436, https://www.doi.org/10.1016/j.jvolgeores.2018.08.014.

Sigmundsson, F., Parks, M., Hooper, A., Geirsson, H., Vogfjörd, K. S., Drouin, V., Ófeigsson, B. G., Hreinsdóttir, S., Hjaltadóttir, S., Jónsdóttir, K., et al., 2022. Deformation and seismicity decline before the 2021 Fagradalsfjall eruption, *Nature*, **609**, 523–528, https://www.doi.org/10.1038/s41586-022-05083-4.

Socco, L. V. & Boiero, D., 2008. Improved Monte Carlo inversion of surface wave data, *Geophysical Prospecting*, **56**(3), 357–371, https://www.doi.org/10.1111/j.1365-2478.2007.00678.x.

Socco, L. V., Boiero, D., Foti, S., & Wisén, R., 2009. Laterally constrained inversion of ground roll from seismic reflection records, *Geophysics*, **74**(6), G35–G45, https://www.doi.org/10.1190/1.3223636.

Socco, L. V., Foti, S., & Boiero, D., 2010. Surface-wave analysis for building near-surface velocity models—Established approaches and new perspectives, *Geophysics*, **75**(5), 75A83–75A102, https://www.doi.org/10.1190/1.3479491.

Strobbia, C. & Foti, S., 2006. Multi-offset phase analysis of surface wave data (MOPA), *Journal of Applied Geophysics*, **59**(4), 300–313, https://www.doi.org/10.1016/j.jappgeo.2005.10.009.

Takei, Y., 2017. Effects of partial melting on seismic velocity and attenuation: A new insight from experiments, *Annual Review of Earth and Planetary Sciences*, **45**, 447–470, https://www.doi.org/10.1146/annurev-earth-063016-015820.

Tarantola, A., 2005. *Inverse problem theory and methods for model parameter estimation*, Society for Industrial and Applied Mathematics, https://www.doi.org/10.1137/1.9780898717921.

Tikhonov, A. N., 1963. On the solution of ill-posed problems and the method of regularization, in *Doklady Akademii Nauk*, vol. 151, pp. 501–504, Russian Academy of Sciences.

Tryggvason, A., Rögnvaldsson, S. T., & Flóvenz, O. G., 2002. Three-dimensional imaging of the P-and S-wave velocity structure and earthquake locations beneath Southwest Iceland, *Geophysical Journal International*, **151**(3), 848–866, https://www.doi.org/10.1046/j.1365-246X.2002.01812.x.

Tsai, V. C., 2009. On establishing the accuracy of noise tomography travel-time measurements in a realistic medium, *Geophysical Journal International*, **178**, 1555–1564, https://www.doi.org/10.1111/j.1365-246X.2009.04239.x.

Vantassel, J. P., Cox, B. R., Hubbard, P. G., & Yust, M., 2022. Extracting high-resolution, multi-mode surface wave dispersion data from distributed acoustic sensing measurements using the multichannel analysis of surface waves, *Journal of Applied Geophysics*, **205**, 104776, https://www.doi.org/10.1016/j.jappgeo.2022.104776.

Verdel, A., Wedemeijer, H., Paap, B., Vandeweijer, V., Weemstra, C., Jousset, P., Franke, S., Blanck, H., Ágústsson, K., & Hersir, G. P., 2016. Reykjanes ambient noise reflection interferometry, in *Proc. European Geothermal Congress, Strasbourg, France*.

Vidale, J. E., 1990. Finite-difference calculation of traveltimes in three dimensions, *Geophysics*, **55**(5), 521–526, https://www.doi.org/10.1190/1.1442863.

Vignoli, G. & Cassiani, G., 2010. Identification of lateral discontinuities via multi-offset phase analysis of surface wave data, *Geophysical Prospecting*, **58**(3), 389–413, https://www.doi.org/10.1111/j.1365-2478.2009.00838.x.

Vignoli, G., Strobbia, C., Cassiani, G., & Vermeer, P., 2011. Statistical multioffset phase analysis for surface-wave processing in laterally varying media, *Geophysics*, **76**(2), U1–U11, https://www.doi.org/10.1190/1.3542076.

Vignoli, G., Gervasio, I., Brancatelli, G., Boaga, J., Della Vedova, B., & Cassiani, G., 2016. Frequency-dependent multi-offset phase analysis of surface waves: an example of high-resolution characterization of a riparian aquifer, *Geophysical Prospecting*, **64**(1), 102–111, https://www.doi.org/10.1111/1365-2478.12256.

Violay, M., Gibert, B., Mainprice, D., Evans, B., Dautria, J.-M., Azais, P., & Pezard, P., 2012. An experimental study of the brittle-ductile transition of basalt at oceanic crust pressure and temperature conditions, *Journal of Geophysical Research: Solid Earth*, **117**(B3), https://www.doi.org/10.1029/2011JB008884.

Wang, Y., 2016. *Seismic inversion: Theory and applications*, John Wiley & Sons, https://www.doi.org/10.1002/9781119258032.

Wapenaar, K. & Fokkema, J., 2006. Green's function representations for seismic interferometry, *Geophysics*, **71**(4), SI33–SI46, https://www.doi.org/10.1190/1.2213955.

Wathelet, M., 2008. An improved neighborhood algorithm: parameter conditions and dynamic scaling, *Geophysical Research Letters*, **35**(9), L09301, https://www.doi.org/10.1029/2008GL033256.

Weaver, R., Froment, B., & Campillo, M., 2009. On the correlation of non-isotropically distributed ballistic scalar diffuse waves, *The Journal of the Acoustical Society of America*, **126**, 1817–1826, https://www.doi.org/10.1121/1.3203359.

Weemstra, C., Boschi, L., Goertz, A., & Artman, B., 2013. Seismic attenuation from recordings of ambient noise, *Geophysics*, **78**(1), Q1–Q14, https://www.doi.org/10.1190/geo2012-0132.1.

Weemstra, C., Westra, W., Snieder, R., & Boschi, L., 2014. On estimating attenuation from the amplitude of the spectrally whitened ambient seismic field, *Geophysical Journal International*, **197**, 1770–1788, https://www.doi.org/10.1093/gji/ggu088.

Weemstra, C., Snieder, R., & Boschi, L., 2015. On the estimation of attenuation from the ambient seismic field: inferences from distributions of isotropic point scatterers, *Geophysical Journal International*, **203**, 1054–1071, https://www.doi.org/10.1093/gji/ggv311.

Weemstra, C., Obermann, A., Verdel, A., Paap, B., Blanck, H., Gudnason, E. Á., Hersir, G., Jousset, P., & Sigurðsson, A., 2016. Time-lapse seismic imaging of the Reykjanes geothermal reservoir, in *Proc. European Geothermal Congress, Strasbourg, France*.

Weemstra, C., De Laat, J. I., Verdel, A., & Smets, P., 2021. Systematic recovery of instrumental timing and phase errors using interferometric surface-waves retrieved from large-N seismic arrays, *Geophysical Journal International*, **224**(2), 1028–1055, https://www.doi.org/10.1093/gji/ggaa504.

Weir, N. R., White, R. S., Brandsdóttir, B., Einarsson, P., Shimamura, H., & Shiobara, H., 2001. Crustal structure of the northern Reykjanes Ridge and Reykjanes Peninsula, southwest Iceland, *Journal of Geophysical Research: Solid Earth*, **106**(B4), 6347–6368, https://www.doi.org/10.1029/2000JB90035810.1111/j.1365-246X.2012.05500.x.

Wielandt, E., 1993. Propagation and structural interpretation of non-plane waves, *Geophysical Journal International*, **113**(1), 45–53, https://www.doi.org/10.1111/j.1365-246X.1993.tb02527.x.

Wilken, D. & Rabbel, W., 2012. On the application of particle swarm optimization strategies on Scholte-wave inversion, *Geophysical Journal International*, **190**(1), 580–594, https://www.doi.org/10.1111/j.1365-246X.2012.05500.x.

Wu, D., Wang, X., Su, Q., & Zhang, T., 2019. A MATLAB package for calculating partial derivatives of surface-wave dispersion curves by a reduced delta matrix method, *Applied Sciences*, **9**(23), 5214, https://www.doi.org/10.3390/app9235214.

Xia, J., Miller, R. D., & Park, C. B., 1999. Estimation of near-surface shear-wave velocity by inversion of Rayleigh waves, *Geophysics*, **64**(3), 691–700, https://www.doi.org/10.1190/1.1444578.

Xiang, E., Guo, R., Dosso, S. E., Liu, J., Dong, H., & Ren, Z., 2018. Efficient hierarchical trans-dimensional Bayesian inversion of magnetotelluric data, *Geophysical Journal International*, **213**(3), 1751–1767, https://www.doi.org/10.1093/gji/ggy071.

Yamanaka, H. & Ishida, H., 1996. Application of genetic algorithms to an inversion of surface-wave dispersion data, *Bulletin of the Seismological Society of America*, **86**(2), 436–444, https://www.doi.org/10.1785/BSSA0860020436.

Yao, H., van Der Hilst, R. D., & De Hoop, M. V., 2006. Surface-wave array tomography in SE Tibet from ambient seismic noise and two-station analysis—I. Phase velocity maps, *Geophysical Journal International*, **166**(2), 732–744, https://www.doi.org/10.1111/j.1365-246X.2006.03028.x.

Yao, H., Beghein, C., & Van Der Hilst, R. D., 2008. Surface wave array tomography in SE Tibet from ambient seismic noise and two-station analysis-II. Crustal and upper-mantle structure, *Geophysical Journal International*, **173**(1), 205–219, https://www.doi.org/10.1111/j.1365-246X.2007.03696.x.

Yao, H., Ren, Z., Tang, J., Guo, R., & Yan, J., 2023. Trans-dimensional Bayesian joint inversion of magnetotelluric and geomagnetic depth sounding responses to constrain mantle electrical discontinuities, *Geophysical Journal International*, **233**(3), 1821–1846, https://www.doi.org/10.1093/gji/ggad029.

Yildirim, I., 2012. Bayesian inference: Gibbs sampling, *Technical Note, University of Rochester*.

Young, M. K., Rawlinson, N., & Bodin, T., 2013. Transdimensional inversion of ambient seismic noise for 3D shear velocity structure of the Tasmanian crustTransdimensional shear velocity inversion, *Geophysics*, **78**(3), WB49–WB62, https://www.doi.org/10.1190/geo2012-0356.1.

Yust, M. B., Cox, B. R., Vantassel, J. P., Hubbard, P. G., Boehm, C., & Krischer, L., 2023. Near-Surface 2D Imaging via FWI of DAS Data: An Examination on the Impacts of FWI Starting Model, *Geosciences*, **13**(3), 63, https://www.doi.org/10.3390/geosciences13030063.

Zhang, X., Curtis, A., Galetti, E., & De Ridder, S., 2018. 3-D Monte Carlo surface wave tomography, *Geophysical Journal International*, **215**(3), 1644–1658, https://www.doi.org/10.1093/gji/ggy362.

Zhang, X., Hansteen, F., Curtis, A., & De Ridder, S., 2020. 1-D, 2-D, and 3-D Monte Carlo Ambient Noise Tomography Using a Dense Passive Seismic Array Installed on the North Sea Seabed, *Journal of Geophysical Research: Solid Earth*, **125**(2), e2019JB018552, https://www.doi.org/10.1029/2019JB018552.

Zhou, Y., Dahlen, F., & Nolet, G., 2004. Three-dimensional sensitivity kernels for surface wave observables, *Geophysical Journal International*, **158**(1), 142–168, https://www.doi.org/10.1111/j.1365-246X.2004.02324.x.

Zulic, S., Sidenko, E., Yurikov, A., Tertyshnikov, K., Bona, A., & Pevzner, R., 2022. Comparison of amplitude measurements on borehole geophone and das data, *Sensors*, **22**(23), 9510, https://www.doi.org/10.3390/s22239510.

Acknowledgements

I am deeply grateful to my esteemed promotors, Kees Weemstra, and Kees Wapenaar, for their unwavering support, constant motivation, and the considerable time they dedicated to guiding me through this research journey. Kees Weemstra's invaluable assistance throughout the entire PhD process, marked by the perfect balance of autonomy and supervision, has been instrumental. His availability for advice and assistance has been a constant source of strength, infusing both my scientific pursuits and personal life with renewed energy. Our shared experience of navigating the challenges of raising young children fostered a unique understanding between us.

I extend my sincere gratitude to Guy Drijkoningen and Mus'ab Al Hasani for their substantial contributions to Chapter 3. The knowledge and insights I gained from both of you were invaluable, and your dedicated efforts played a pivotal role in enhancing the quality of that chapter. I am truly appreciative of the collaborative learning experience and the marked improvement you brought to this section of the thesis.

I want to convey my deep appreciation to Gylfi Páll Hersir, Thorbjörg Ágústsdóttir, and Egill Árni Gudnason, esteemed Geologists and Geophysicists from Iceland Geosurvey, for their exceptional contributions to Chapter 5 of this thesis. Their collaborative efforts in interpreting tomographic results significantly enhanced the quality of the chapter. I am grateful for their patience during the manuscript drafting process and for generously sharing their wealth of knowledge. Additionally, I express my thanks to Xin Zhang for his valuable contributions to Chapters 4-5.

I would like to thank Faezeh, Siamak, and Aydin for their meaningful discussions on diverse scientific topics and support throughout my Ph.D. journey. Their insights and encouragement have been invaluable, contributing to the richness of my research experience.

Additionally, I am deeply grateful for the funding provided for this research by the Iran Ministry of Science, Research and Technology and the European Research Council (ERC). The financial support from these institutions has played a crucial role in advancing this work, and I express my sincere appreciation for their contributions to the success of this project.

Then, my heartfelt gratitude goes to my family and friends, whose unwavering support has been a pillar of strength throughout this academic journey. My wife, Zohreh, deserves special mention for her steadfast encouragement and

understanding. Her support has been a constant source of motivation. I also extend my thanks to my little son, Mohammad-Hossein, whose infectious joy has filled my moments of respite with laughter and fun, providing a delightful balance to the rigors of research. The love and encouragement from my family have been invaluable, and I am truly fortunate to have them by my side.

Curriculum Vitæ

Amin Rahimi Dalkhani

06-03-1990	Born in Shiraz, Iran.

Education

2019-2024	Ph.D. Applied Geophysics Delft University of Technology, Delft, The Netherlands. *Thesis:* Transdimensional surface wave inversion: 1D, 2D, 3D applications
2012-2015	M.Sc. Petroleum Geosciences Engineering Amirkabir University of Technology, Tehran, Iran. *Thesis:* Seismic wave propagation modeling: Finite Element, Finite Difference, and Spectral Element methods
2008-2012	B.Sc. Petroleum Engineering Amirkabir University of Technology, Tehran, Iran. *Thesis:* Reservoir characterization using seismic and well log data integration
2004–2008	Mathematics & Physics Razi High-school, Shiraz, Iran.

Experience

2019-2024	Ph.D. Candidate, TUDelft, Delft, The Netherlands
2017-2019	Researcher and software developer, RIPI, Tehran, Iran
2015-2017	Researcher and software developer, NIOOC, Tehran, Iran

List of publications

7. **Rahimi Dalkhani, A.**, Ágústsdóttir, T., Gudnason, E. Á., Hersir, G. P., Zhang, X., & Weemstra, C. (2024). Transdimensional ambient-noise surface wave tomography of the Reykjanes Peninsula, SW Iceland. *Geophysical Journal International*, **236**(1), 621-643.

6. Weemstra, C., **Rahimi Dalkhani, A.**, Ágústsdóttir, Þ., Árni Guðnason, E., Páll Hersir, G., & Zhang, X. (2023, May). Inferences on the shear wave velocity structure below the Reykjanes peninsula (SW Iceland) from transdimensional ambient-noise surface wave tomography. In EGU General Assembly Conference Abstracts (pp. EGU-4979).

5. **Rahimi Dalkhani, A.**, Hasani, M. A. A., Drijkoningen, G., & Weemstra, C. (2023). Transdimensional surface wave tomography of the near-surface: Application to DAS data. *arXiv preprint*, arXiv:2304.10678 (submitted to Geophysics).

4. Shirmohammadi, F., Hatami, M. R., & **Rahimi Dalkhani, A.** (2022). Surface wave tomography and radial anisotropy using seismic interferometry in the Cental Alborz. *Iranian Journal of Geophysics*, **16**(3), 183-197.

3. **Rahimi Dalkhani, A.**, Zhang, X., & Weemstra, C. (2021). On the potential of 3D transdimensional surface wave tomography for geothermal prospecting of the Reykjanes Peninsula. *Remote Sensing*, **13**(23), 4929.

2. **Rahimi Dalkhani, A.**, Zhang, X., & Weemstra, C. (2021, October). 3D transdimensional ambient noise surface wave tomography of the Reykjanes Peninsula–a feasibility study. In 82nd EAGE Annual Conference & Exhibition (Vol. 2021, No. 1, pp. 1-5). European Association of Geoscientists & Engineers.

1. **Rahimi Dalkhani, A.**, Ruigrok, E., & Weemstra, C. (2019, November). Towards a Near-Surface Velocity Model of Groningen using Transdimensional Markov Chains. In Fifth EAGE Workshop on Borehole Geophysics (Vol. 2019, No. 1, pp. 1-5). European Association of Geoscientists & Engineers.